Available online at www.sciencedirect.com
SCIENCE DIRECT®
Physics Reports 413 (2005) 91–196
PHYSICS REPORTS
www.elsevier.com/locate/physrep

Chemical and biological activity in open flows: A dynamical system approach

Tamás Tél[a], Alessandro de Moura[b], Celso Grebogi[b,c,*], György Károlyi[d]

[a] *Institute for Theoretical Physics, Eötvös University, P.O. Box 32, H-1518, Budapest, Hungary*
[b] *Instituto de Física, Universidade de São Paulo, Caixa Postal 66318, 05315-970, São Paulo, SP, Brazil*
[c] *Max-Plank-Institute for the Physics of Complex Systems, Nöthnitzer Str. 38, D-01187 Dresden, Germany*
[d] *Center for Applied Mathematics and Computational Physics, and Department of Structural Mechanics, Budapest University of Technology and Economics, Műegyetem rkp. 3, H-1521, Budapest, Hungary*

Accepted 3 January 2005
Available online 28 April 2005
editor: I. Procaccia

Abstract

Chemical and biological processes often take place in fluid flows. Many of them, like environmental or microfluidical ones, generate filamentary patterns which have a fractal structure, due to the presence of chaos in the underlying advection dynamics. In such cases, hydrodynamical stirring strongly couples to the reactivity of the advected species: the outcome of the reaction is then typically different from that of the same reaction taking place in a well-mixed environment. Here we review recent progress in this field, which became possible due to the application of methods taken from dynamical system theory. We place special emphasis on the derivation of effective rate equations which contain singular terms expressing the fact that the reaction takes place on a moving fractal catalyst, on the unstable foliation of the reaction free advection dynamics.

PACS: 05.45.−a; 47.52.+j; 47.53.+n; 47.70.Fw

Keywords: Reaction; Chaotic advection; Diffusion; Filamentary fractal; Advection–reaction–diffusion; Population dynamics; Inertial effect; Non-hyperbolic effect

* Corresponding author. Instituto de Física, Universidade de São Paulo, Caixa Postal 66318, 05315-970, São Paulo, SP, Brazil.
E-mail address: grebogi@if.usp.br (C. Grebogi).

0370-1573/$ - see front matter © 2005 Elsevier B.V. All rights reserved.
doi:10.1016/j.physrep.2005.01.005

Contents

1. Introduction

1.1. Motivation

Several chemical and biological processes occur in fluid flows, both in natural systems and in engineering. Such processes are especially important in environmental systems, such as plankton blooming in the oceans [2,3,25,116–118,142,173,210], and the formation of the ozone hole in the stratosphere [41,190,58]. They are, however, relevant in a broad range of other fields as well, including chemistry [125,43,123,124,5], population dynamics [179,181,86], geophysical sciences [62,202,186], microfluids [197,121,23,150,216,134] and combustion [219,54,89,90]. In these systems, particles are carried by the motion of the fluid, and they change due to their chemical and biological interactions. We say that these particles are *active*, in the sense that they are not just passively advected by the flow, but they follow dynamical processes of their own. In other words, they *do* something. For example, plankton 'particles' (cells) reproduce and die, their number changes; the various chemicals involved in ozone depletion transform into each other, and lead to an overall decay of ozone. Fig. 1 illustrates the idea, showing a particle that is advected for some time by the flow, and then undergoes a multiplicative process. For simplicity, we refer to such systems as *active flows*, by which we mean flows carrying active particles. We emphasize, however, that this kind of activity is assumed to have no feedback on the fluid flow, which is a realistic assumption in many applications. An unusual feature of many of these reactions, as shown e.g. in Figs. 2–5, is that they take place along *filamentary* spatial structures.

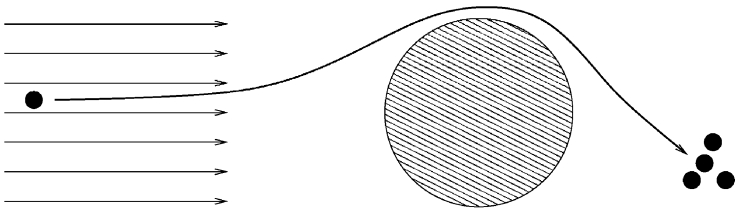

Fig. 1. Illustration of a kind of active process taking place in a flow.

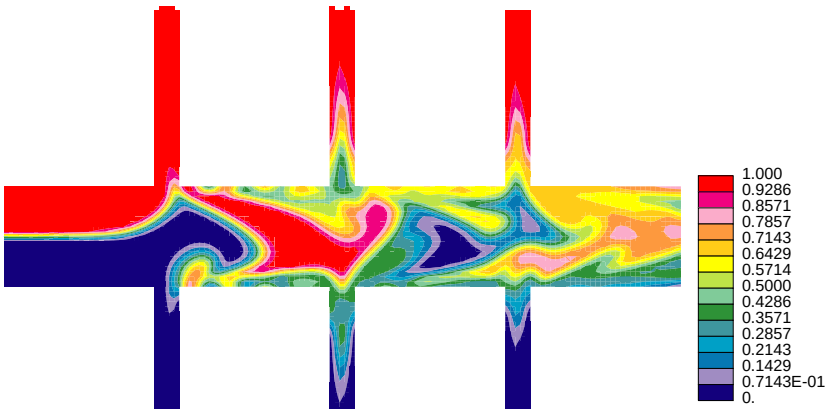

Fig. 2. (Color online.) Concentration distribution of a passive scalar (red: full concentration, dark blue: zero concentration) in a micromixer. The flow in the main channel is stationary and is manipulated by time-periodic flows in the secondary channels. The frequency of these perturbations can be used to enhance mixing. Picture by S.D. Müller, I. Mezić, J.H. Walther and P. Koumoutsakos, with their kind permission.

The main fields of phenomena where chemical or biological reactivity plays a role can be grouped into the following categories, according to their length scale (see Table 1):

- *Microfluidics:* Recent technological advancement has made the fabrication of microchannels of a few hundred micrometers in cross-section possible [23,134] (Fig. 2). These are used e.g. in printers and in bio-medical equipment. At the microfluidic scale, viscosity dominates and turbulence cannot be present; also, diffusion can usually be neglected. The only effective source of mixing is then chaotic advection.
- *Laboratory scale flows:* This covers a broad range of phenomena on the human scale, including chemical industry applications, flames and combustion, as well as laboratory experiments (see Fig. 3).
- *Flows in oceans or large lakes:* The most typical reactive process on this scale is plankton dynamics (see Fig. 4). Phytoplankton is a key ingredient in the carbon exchange with the atmosphere and plays thus a role in regulating the greenhouse effect. The population dynamics of other micro-organisms and the spread of chemically reacting pollutants also belongs here.

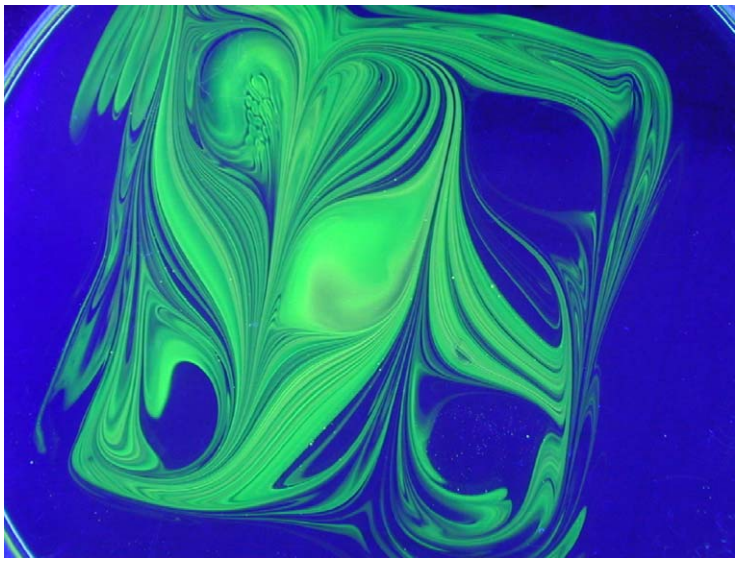

Fig. 3. Shape of a dye (flouresceine) droplet (of initial diameter about 1 cm) after stirring on the surface of a thin layer of glycerol in a Petri dish. The stirring protocol is that of the experiment by Villermaux and Duplat [214]: a number of parallel cuts is made by a rod through the fluid in two direction in an alternating manner. Experiment carried out by I.M. Jánosi, K.G. Szabó, T. Tél, and M. Wells at the von Kármán Laboratory of Eötvös University, Budapest.

Fig. 4. (Color online.) Filamentation in a phytoplankton bloom in the Norwegian Sea. Provided by the SeaWiFS Project, NASA/Goddard Space Flight Center, and ORBIMAGE, URL: http://visibleearth.nasa.gov/cgi-bin/viewrecord?5278.

- *Atmospheric flows:* The prototype process is ozone depletion in the stratosphere (see Fig. 5), influencing essentially the greenhouse effect. Several other reactions of atmospheric chemistry are also of interest. Outside the planetary boundary layer, flows are practically two-dimensional (as well as in the oceans), due to the dominance of the Coriolis effect and density stratification.

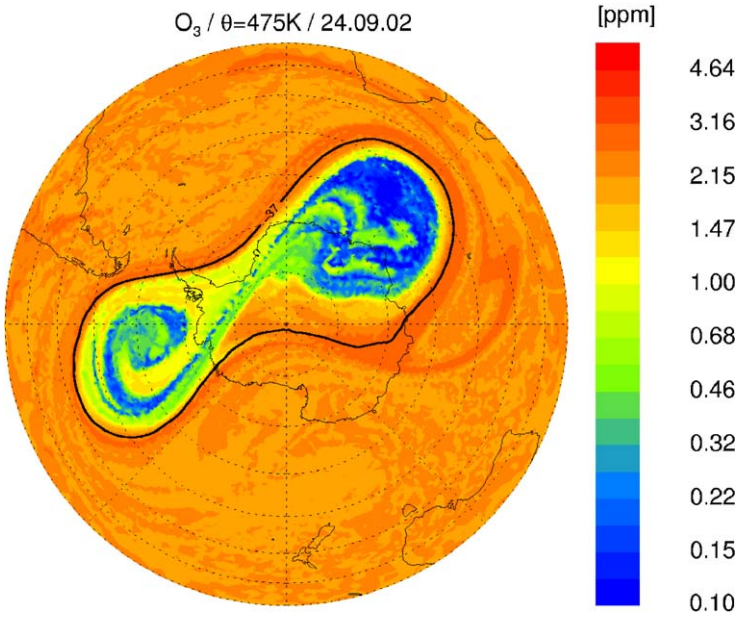

Fig. 5. (Color online.) Ozone distribution (in mixing ratio measured in parts per million (ppm)) above the South Pole region at about 18 km altitude on September 24, 2002. The chemical reactions leading to ozone depletion are simulated over 23 days in the flow given by meteorological wind analyses (from Grooß, Konopka, and Müller, Ozone chemistry during the 2002 Antarctic vortex split [58], with permission) during a very rare event when the so-called polar vortex splits into two parts.

Table 1
Typical length and velocity scales of important flows, as detailed in the main text

	Microfluids	Laboratory	Ocean	Atmosphere
L (m)	5×10^{-4}	1	10^5	10^6
U (m/s)	10^{-2}	10^{-2}	10^{-1}	10

In studying active flows, it is of particular importance to relate the dynamics of the reactive system to the underlying advection dynamics of the flow. In other words, how does the advection dynamics affect total reaction productivity, or population dynamics of different species in the flow? The Lagrangian formulation of the equations of motion for the flow is the relevant framework in this context, because we are interested in the behavior of the particles advected by the fluid. It is well-known (see e.g. [7,153,33,35,78,229,174,87,221,114,128,225]) that even very simple flows may have chaotic advection dynamics, characterized by an extreme sensitivity of the motion to initial conditions. *Lagrangian chaos* is a very general feature, found in most real flows.

In this work, we review recent results which show that the character of a reaction can drastically change if it takes place in a time-dependent chaotic flow. A reaction can lead to a pattern formation of a new type: the product is asymptotically distributed around a filamentary fractal which moves in a rhythm corresponding to the time dependence of the flow. In a periodic case, the total amount of product is thus

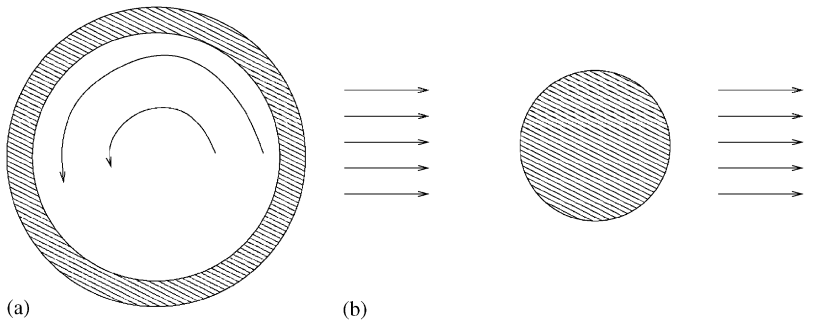

Fig. 6. Illustrations of (a) closed, and (b) open flows.

oscillating about a mean: a kind of limit-cycle behavior sets in even if the original reaction kinetics leads to a time-independent stationary state. This pattern formation is due to the interplay of the chaotic particle motion produced by hydrodynamics and the production of the new particles by the reaction.

Flows can be grouped into two main classes: closed and open ones. A flow is closed if its motion is confined to a bounded domain (see Fig. 6a). A flow is open if there is a net current flowing through the region of observation. We also assume that far from the region of observation the flow is simple (nearly homogeneous). A typical example is the flow around an obstacle (see Fig. 6b). In open flows, most trajectories are unbounded, and particles escape the observation region in a finite time. Even flows that are actually closed can in many cases be considered open, if the time it takes for typical particles to return to the observation region is much longer than the relevant time-scale of observation. As an example, the ocean is of course a closed fluid system, but if we are looking at a small region surrounding an island, the average return time might be of the order of hundreds of years. The fluid flow in the vicinity of the island can, for all practical purposes, be considered open. There are many other important flow systems which can be effectively open, especially environmental and microfluidic flows (see e.g. Fig. 2).

Both closed and open flows are important, and can of course carry some kind of activity. The dynamical system approach to the active problem turns out, however, to be more relevant for the case of open flows: it is in this class where the effective rate equation to be derived explicitly contains the chaos parameters of the advection dynamics. Our presentation is therefore biased towards open flows, and touches only some aspects of closed ones.

1.2. Relevance of open flows

The question of the interplay between chaotic advection and activity was first addressed by Metcalfe and Ottino in the context of closed flows [125,43]. The asymptotic state (reached as $t \to \infty$) is typically a homogeneous distribution of the components in the fluid, and there is no enhancement of activity in this state.

In open flows, however, chaos takes a different form [204], because typical advected particle orbits escape the observation region in a finite time. There are, however, non-escaping orbits which are bounded within a finite region, located e.g. in the vicinity of the wake in the case of a flow around an obstacle. These non-escaping orbits form a chaotic set of the dynamical system associated with advection, which is known as a *chaotic saddle*. Even though the orbits in the chaotic saddle are unstable and in many

cases make up a set of measure zero, they control the long-term dynamics of the system. Chaotic saddles have a complex, fractal geometric structure, and they give rise to extreme sensitivity to initial conditions of particle trajectories. This sensitivity is related to the *fractal dimension* of the chaotic saddle, and characterizes its geometry. The chaotic dynamics of open flows is a special case of *transient chaos* [204], i.e., chaos of finite lifetime, as opposed to persistent motion on attractors, found in dissipative systems. It is worth mentioning that due to the openness of a flow even the spectrum of passive scalars changes: it becomes steeper than the Batchelor spectrum, and the shift of the spectral exponent can be expressed in terms of transient chaos properties [137].

In this work, we present a general theoretical framework for the understanding of the reactive dynamics of particles advected by open chaotic flows. This area has attracted great interest since the appearance of the first papers by Toroczkai, Károlyi, Péntek, Tél and Grebogi [209,83,205], and there have been many new and interesting results since then. Due to space constraints, this review is necessarily limited in its scope. However, we try to present the main results in the area as well as the theoretical concepts that unify them.

The basic picture that emerges from the study of active dynamics in open chaotic flows is that in all cases *most of the reactivity is concentrated along a fractal set* [204], forming clearly visible filamentary patterns in space. This fractal set is associated with the chaotic saddle, being its *unstable manifold*. The concentration of reactivity along a filamentary fractal results in a singular enhancement of the productivity associated with the reaction (as compared to the productivity in non-chaotic flows). As we will show, this enhancement is reflected by a singular production term in the reaction rate equation, which is absent if the flow is not chaotic. This singular term is related in a well-defined way to the fractal dimension of the chaotic saddle [204] (in fact, to the fractal dimension of its unstable manifold), and therefore it is a consequence of the fractal geometry of the set of non-escaping orbits. This is because the surface (or perimeter, in the case of two-dimensional flows) of the fractal filaments of the unstable manifold diverges with refining resolution. As it is a consequence of a basic geometric property of fractals, the enhancement of activity is a very general and pervading phenomenon, and is largely independent of the particulars of the active process, or of the details of the flow, so long as it is open and its dynamics is chaotic. We will illustrate this through many examples and applications. We stress that this phenomenon is *not* a result of artificial assumptions of particular models, but is expected to be a general feature of real active open flows. Hence, the theory we present here has potentially broad applicability, and could be a valuable tool in areas where reactivity in flows plays an important role, like chemistry, biology, oceanography, atmospheric sciences, engineering, and others.

1.3. Organization of the paper

We start with a presentation of the phenomena in simple systems (two-dimensional incompressible flows with non-inertial particles displaying autocatalytic activity), and then proceed to more complex situations, including three-dimensional flows, transport barriers (non-hyperbolic motion), chaotically time-dependent or random flows, inertial tracers, and more complex chemical or biological activity. Throughout the presentation, we try to emphasize how the active dynamics in all these cases can be understood within a single unifying theoretical framework.

In Section 2, we review the basic results related to chaotic advection, focusing on applications to open flows. We put emphasis on those aspects that are of direct relevance to the understanding of active dynamics, including the notions of invariant chaotic sets, stable and unstable manifolds, and fractal

dimension. We also introduce some important examples of two-dimensional incompressible open flows that display Lagrangian chaos: the von Kármán vortex street, the blinking vortex–sink systems and the case of four point vortices.

In Section 3, we present some simple models of activity, corresponding to different ways by which the advected particles can be active. We introduce both a discrete kind of modeling, where individual particles are considered, and a continuous modeling, where concentrations are considered. We use the autocatalytic reaction ($A + B \longrightarrow 2B$) as an example because it is both simple and important, and it underlies many real reactive processes.

Section 4 brings together the motion of the flow (Section 2) and the activity of the advected particles (Section 3), and presents the basic theory of the dynamics of active processes in open flows. We expose the theory in the context of 2D incompressible time-periodic flows. This allows us to present the basic ideas of the theory as clearly as possible. We argue that our approach and its results are valid for any situation in which a well-defined reaction front exists, independently of the details of the flow motion or of the particular kind of reaction. We derive an effective rate equation, and we emphasize the new features in the reaction dynamics brought about by chaos, especially the enhancement of productivity.

In Section 5, we discuss a striking application of the theory, introduced in Section 4, to population dynamics. Two or more species of micro-organisms (like plankton) inhabiting a flow, and competing for a single resource, can coexist in a chaotic flow, whereas in non-chaotic flows the fittest species would necessarily drive all the others to extinction. This result sheds new light on the so-called 'plankton paradox', a classical problem in ecology. It also illustrates that the reactive dynamics of open chaotic flows can be very different from that of well-mixed flows.

Section 6 extends the theory presented in Section 4 to 3D flows. Essentially the same phenomenon of productivity enhancement and fractal-like distribution of reacting particles are preserved in 3 dimensions. Thus, they are not a specific feature of 2D flows. Moreover, new effects appear due to the extra dimension that have no counterpart in 2D.

In Section 7, the reactive dynamics in aperiodic flows is investigated. On certain time scales, these flows can be regarded as random, and can be modeled by *random maps*. This allows us to derive an average rate equation for reactions taking place in such flows. The result is that there is again an enhancement due to the chaotic motion of the flow, even though it is aperiodic. This shows that this enhancement is indeed a general phenomenon, and not a particular feature due to time-periodicity.

In Section 8, we investigate the case when the advection dynamics is non-hyperbolic, corresponding to the existence of transport barriers, associated to large vortices in the flow. There are then many qualitatively new features in the reaction dynamics, caused by the 'stickiness' of the advection dynamics near the barriers. We show that the effects of non-hyperbolicity can be understood via the introduction of a new quantity called the *effective dimension*.

In Section 9, we consider active particles with a non-negligible inertia. In this case, the advection dynamics is dissipative, and attractors might be formed, which are typically chaotic. We investigate the reactive dynamics in this case, and we argue that, irrespective of whether the flow is closed or open, we can apply the theory of Section 4. The reason is that in both closed and open flows, the active particles accumulate on a fractal set. This shows that the theory presented here, although developed for open flows, is actually more generic.

In Section 10, we discuss reactive processes other than autocatalytic ones. These include bistable reactions, excitable media, flames, and collisional reactions. We find throughout that the reaction dynamics is dominated by fractal sets, as in the simpler cases, and singular terms are also present in the rate equation.

Even though this work addresses mostly open flows, the insight gained there can be applied to describe some basic aspects of reactivity in closed flows. This subject is taken up in Section 11.

Through most of this work, the models are continuous in time, giving rise to rate equations in the form of ordinary differential equations. In Section 12, we follow another approach, which considers the reactions to occur at discrete times. The rate equations are then replaced by maps. The two approaches are compared, and certain phenomena exclusive to the discrete-time modeling are discussed. This discrete approach might especially be important for modeling population dynamical processes.

We conclude in Section 13 with some final remarks and perspectives for future research.

2. Passive advection dynamics in open flows

2.1. Chaotic sets, fractal manifolds

In this section, we show how advection in open flows can be considered as a scattering process, and how it can be understood in the framework of the theory of dynamical systems. In particular, we will see that open flows can display a kind of chaos known as *chaotic scattering* [152].

In the simplest approximation, the particles are assumed to take on the velocity of the surrounding flow very rapidly, so that inertial effects can be neglected. We can thus suppose that at each instant the velocity of the advected particle is the same as that of the fluid at the same position. The equation of motion is then

$$\dot{\mathbf{r}} \equiv \frac{\mathrm{d}\mathbf{r}}{\mathrm{d}t} = \mathbf{u}(\mathbf{r}(t), t) \ , \tag{1}$$

where $\mathbf{r}(t)$ is the position vector of the advected particle, and $\mathbf{u}$ is the velocity field of the flow, which may depend explicitly on time. Finding the functional form of $\mathbf{u}$ for a specific case is usually a hard task, since it requires solving the Navier–Stokes equation with the appropriate boundary conditions. Here we are primarily interested in the dynamics of advected particles for a given flow field, so we simply assume that $\mathbf{u}(\mathbf{r}, t)$ is known.

Of particular importance to us is the case of two-dimensional incompressible flows, with $\mathbf{r} = (x, y)$, $\mathbf{u} = (u_x, u_y)$, and $\operatorname{div}\mathbf{u} = \partial u_x/\partial x + \partial u_y/\partial y = 0$. Both the oceans and the atmosphere (for velocities much smaller than the speed of sound) can be regarded as incompressible, and can in many situations be considered two-dimensional systems as well [156]. In this case, there exists a stream function $\psi(x, y, t)$ whose derivatives give the velocity components of the flow [101,16]:

$$u_x(x, y, t) = -\frac{\partial\psi(x, y, t)}{\partial y}, \quad u_y(x, y, t) = \frac{\partial\psi(x, y, t)}{\partial x} \ . \tag{2}$$

Substituting the above equations in Eq. (1), one obtains the equation of motion for an advected particle in terms of the stream function:

$$\dot{x} = -\frac{\partial\psi}{\partial y}, \quad \dot{y} = \frac{\partial\psi}{\partial x} \ . \tag{3}$$

One immediately notices that the pair of equations above has a Hamiltonian structure, with the variable x playing the role of position, y playing the role of conjugate momentum, and the stream function $\psi(x, y, t)$ being the Hamiltonian [101,16]. Thus, we identify the dynamics of a passively advected particle in

a planar incompressible flow with a one-degree-of-freedom Hamiltonian system. The phase space of this Hamiltonian system coincides with the physical plane in which the flow occurs. As a consequence, the phase-space structures of this dynamical system are directly visible, and can even be photographed in experiments [195]. This is because the phase-space variables of the associated Hamiltonian system correspond to the real-space coordinates of the advected particle in configuration space.

If the flow is stationary, the stream function (or Hamiltonian) ψ does not depend on time, and the particle trajectories coincide with the level curves of ψ, called *streamlines* in fluid mechanics [101,16]. From a dynamical point of view, in this case we have a one-degree-of-freedom time-independent Hamiltonian system, which is always integrable. In most realistic situations, however, the flow is non-stationary, and ψ depends on time explicitly. In this case, one has a one-degree-of-freedom Hamiltonian system with a *time-dependent* Hamiltonian. It is well-known that such driven systems typically exhibit non-integrable dynamics, or *chaos* [152]. This means that an advected particle moves unpredictably, and displays a great sensitivity to initial conditions. This kind of chaoticity in the advection dynamics is sometimes referred to as *Lagrangian chaos*, or *Lagrangian turbulence* [7]. We observe that this is distinct from what is usually called turbulence in fluid dynamics (*Eulerian turbulence*), which implies a very complicated time *and* space dependence for ψ. Even very simple time dependencies of ψ can generate Lagrangian chaos, even though the corresponding flow is far from being turbulent in the Eulerian sense. For example, simple time-periodic flows in general display chaotic advection, even though they are laminar in space [7,153,33,170,218,171,192,191,195]. From now on, we shall refer to flows having Lagrangian chaos simply as *chaotic flows*.

In this review we are mainly interested in open flows, such as the one illustrated in Fig. 6b. As mentioned in the Introduction, such flows are characterized by the existence of a net current. In other words, the fluid is moving from an *upstream* region towards a *downstream* region. In most cases of interest, the time-dependent part of the dynamics is restricted to a finite region of space, called the *mixing region*. An illustrative example is the flow with an obstacle placed in the middle, as sketched in Fig. 6b. In both the upstream and the downstream region, the flow is asymptotically stationary. The time dependence, and hence the chaotic part of the dynamics, is restricted to the mixing region in the wake of the obstacle.

From the point of view of the theory of dynamical systems, advection in open flows is a *scattering* process: there is an asymptotic region where the dynamics is simple, and a bounded region where the dynamics is non-trivial. This latter is called the *interaction region*, which corresponds to the mixing region for fluids. The advected particles typically come from the asymptotically simple region, stay in the interaction region for a while, and then escape again to the asymptotic region. In scattering systems, the accessible phase-space is unbounded, whereas for a confined system (such as a flow within a container) the accessible phase-space has finite volume. When a scattering system displays chaos, *chaotic scattering* is said to occur [204]. Chaotic open flows are instances of chaotic scattering. We now discuss briefly the main properties of chaotic scattering, since they are fundamental to our subject.

We assume that the 2D flow is time-periodic, with some period T: $\psi(x, y, t + T) = \psi(x, y, t)$. The advection dynamics can then be described by a stroboscopic map M, which connects the position of the advected particle at time $nT + t_0$ to that at time $(n + 1)T + t_0$:

$$(x_{n+1}, y_{n+1}) = M_{t_0}(x_n, y_n) \ , \tag{4}$$

where $0 \leqslant t_0 < T$. Since the flow is incompressible, M_{t_0} is an area-preserving diffeomorphism. This is the simplest case of chaos in an open flow, and we will study it in detail in this review. We will see, however, that the results remain essentially unchanged for much more general systems (see Section 7).

Chaotic scattering systems are characterized by the existence of a complicated set of non-escaping orbits in the interaction region (that is, the mixing region in case of open flows). These are orbits that never escape to the asymptotic regions, either in the past ($t \to -\infty$) or in the future ($t \to +\infty$). These orbits make up a set which has a fractal structure in phase-space, and appear as a fractal cloud of points sprinkled on the 2D space of the fluid in a stroboscopic map. This invariant set of non-escaping orbits is called the *chaotic saddle*, and it is responsible for all the main features of chaotic scattering [204].

An important invariant set associated to the chaotic saddle is its *stable manifold*. It is defined as the set of initial conditions (points) in phase space such that their corresponding orbits approach asymptotically the chaotic saddle, as the discrete time $n \to +\infty$. Particles moving along the stable manifold enter the mixing region and never leave it, becoming 'trapped' there. However, the stable manifold has in general zero area (more precisely, zero Lesbegue measure), which means that the probability that a randomly chosen point in phase space belongs to the stable manifold is zero. Thus, almost all orbits will leave the interaction region some finite time after entering it, and only a set of measure zero corresponds to orbits which do not leave. In spite of this, the stable manifold has a great influence on the global dynamics of the system. Particles starting from points close to it will spend a long time in the interaction region before escaping, and these long-lived trajectories are responsible for the sensitivity of the dynamics to initial conditions. Like the chaotic saddle, the stable manifold is also a fractal set, and its fractal (box-counting) dimension D satisfies $1 < D < 2$.

Another invariant set related to the chaotic saddle is the *unstable manifold*. This is the set of phase-space points whose orbits approach the chaotic saddle asymptotically as $n \to -\infty$. The unstable manifold is the set of points along which points lying infinitesimally close to the chaotic saddle will eventually escape it in the course of time. It is also fractal, and due to the invariance under time-reversal of the Hamiltonian system (3), its fractal dimension is D, the same as that of the stable manifold. Time invariance implies that the chaotic saddle is the direct product of two Cantor sets of identical dimension d each, with $0 < d < 1$. The saddle's dimension is thus $D_{\text{saddle}} = 2d$. Both the stable and unstable manifolds are the direct product of a line (of dimension 1) and a Cantor set of partial dimension d, their dimension can therefore be written as $D = 1 + d$. Consequently, $D_{\text{saddle}} = 2(D - 1)$.

The unstable manifold can be *directly observed* in open flows [195]. By considering initially a droplet of particles, corresponding to a set of initial conditions which overlap the stable manifold, as time goes on, the particles get advected to the mixing region. Those particles which last a long time there without escaping fall very close to the chaotic saddle, and when they finally leave, they trace out the unstable manifold (Fig. 7). In short, once the bulk of the particles has escaped, the remaining ones, with longer lifetimes in the mixing region, are concentrated around a fractal set, namely the unstable manifold. This fact is of fundamental importance for all the results to be described in this work. One particular consequence of this is that classical flow visualization techniques based on dye evaporation or streaklines [213] trace out curves which are different from streamlines or any other Eulerian characteristic of the velocity field, and are in fact the unstable manifolds of chaotic saddles. Another aspect of fractality can be seen when using different dies: their boundaries typically contain fractal parts [158]. In the presence of three or more colors, the boundary can even be of WADA type. i.e., *all* the colors accumulate along a single fractal curve [208].

The stroboscopic map (4) depends on the parameter t_0, which is proportional to the phase of the oscillation at the instant the map is taken. For each choice of t_0, the chaotic saddle, as well as its stable and unstable manifolds, has a different shape. However, all the dynamical invariants, such as the fractal dimension, Lyapunov coefficients, etc., are all *independent* of t_0. In the original time-continuous

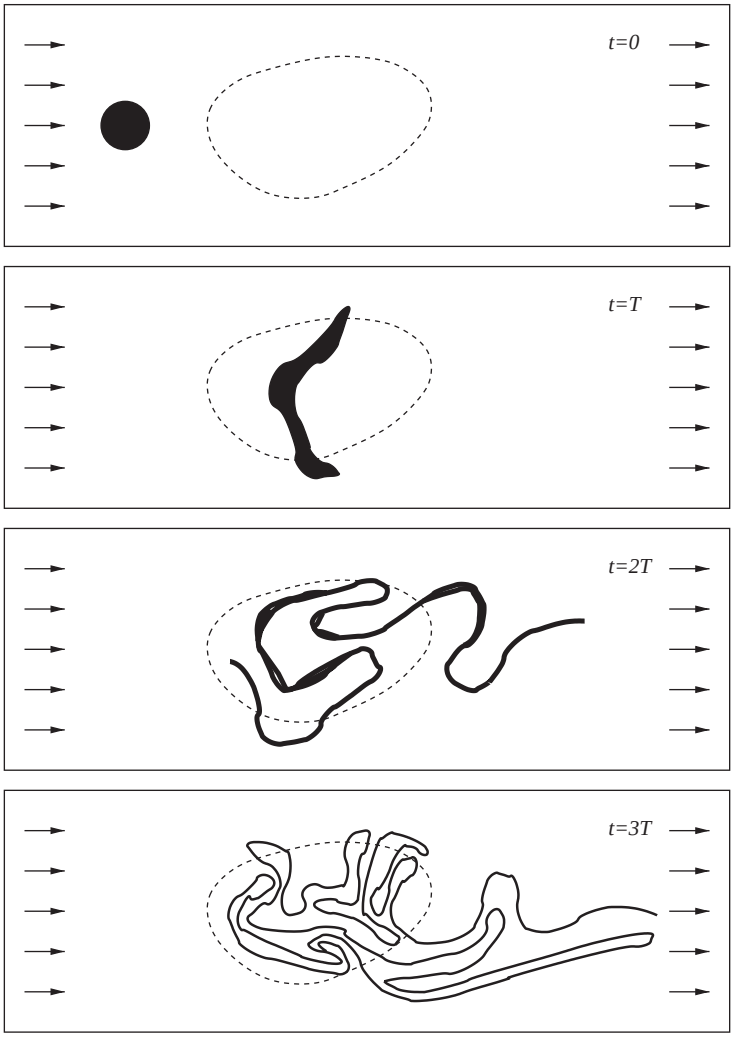

Fig. 7. Relevance of the unstable manifold: schematic diagram illustrating the distribution of an originally compact and small dye droplet in the mixing region of an open flow. After some time, the not yet escaped dye particles trace out the unstable manifold of the chaotic saddle existent in the mixing region.

system (3), these manifolds are fractal filaments with shapes changing in time, but recurring with a period T. For pictures of the unstable manifold for a particular system, see Fig. 14.

Scattering systems are either *hyperbolic* or *non-hyperbolic*, according to the stability of the orbits in their chaotic saddles. In hyperbolic systems, all orbits in the chaotic saddle are strictly unstable. One of the consequences of hyperbolicity is that the chaotic saddle has zero measure: almost all initial conditions lead to orbits that eventually escape the interaction region. Another feature of hyperbolic systems is that, if we initially have a large number of particles uniformly distributed on an observation region intersecting the interaction region, the number $\mathcal{N}(t)$ of particles that have not escaped the region up to time t decays exponentially, $\mathcal{N}(t) \sim \mathrm{e}^{-\kappa t}$. The coefficient κ is the *escape rate* of the process. It satisfies $\kappa < \overline{\lambda}$, where $\overline{\lambda}$

is the chaotic saddle's Lyapunov exponent, calculated as an average of the largest eigenvalues of all orbits in the saddle, weighted by the natural measure of the saddle. Physically, the Lyapunov exponent gives the exponential rate of separation of nearby advected particles in the mixing region. There is a classical formula relating three important dynamical invariants for 2D hyperbolic open systems [79]:

$$D_1 = 2 - \frac{\kappa}{\bar{\lambda}} . \tag{5}$$

Here D_1 is the *information dimension* of the unstable manifold, which is a fractal dimension taking into account the saddle's natural measure (roughly, it gives more weight to regions where a typical particle spends more time), differently from the fractal (or box-counting) dimension D, which is a purely geometrical quantity. However, D_1 is typically very close to D, and therefore Eq. (5) usually provides a very good estimate for D as well. In what follows we shall mainly use the fractal dimension D of the manifolds. For this reason, we write Eq. (5) using D instead of the information dimension D_1:

$$D = 2 - \frac{\kappa}{\bar{\lambda}} . \tag{6}$$

This equation is an approximation, valid when D is close to D_1. Since this is the case for all systems considered, we will from now on ignore this difference, and always use Eq. (6) directly.

Another possibility is that the scattering dynamics is non-hyperbolic. In this case, there are marginally stable orbits in the chaotic saddle. These orbits are surrounded by stable regions, from which fluid does not escape. In these stable regions there are quasi-periodic orbits forming the so-called *KAM islands*, well-known in Hamiltonian chaos [112]. These islands form a fractal hierarchical structure, with big islands being surrounded by smaller islands, and these in turn are surrounded by even smaller islands, and so on. From the point of view of advection, these KAM islands correspond (in two-dimensional flows) to absolute *transport barriers*, where fluid is trapped. They can be seen as vortices in the flow. An immediate consequence of the existence of KAM islands is that there is a finite volume of initial conditions in the interaction region whose orbits do not escape, namely those within the islands (or vortices). Consequently, the chaotic saddle has non-zero measure. However, tracers with initial conditions *outside* the interaction region cannot enter the islands, because of the uniqueness property of solutions of ordinary differential equations. As a result, the set of non-escaping initial conditions outside the interaction region which leads to the saddle still has zero measure, so that almost all scattering trajectories (starting in the asymptotic region) escape after a finite time spent in the interaction region, as in the hyperbolic case. However, there are several differences between the two cases. The fractal dimension D of the stable (and unstable) manifold takes the maximum value of 2 in non-hyperbolic flows [103]. Another difference is that the number $\mathcal{N}(t)$ of particles that have not escaped up to time t follows a power law $N(t) \sim t^{-\sigma}$, $\sigma > 0$, as opposed to the exponential law satisfied by hyperbolic systems. The advection dynamics is assumed to be hyperbolic until we turn to the investigation of non-hyperbolic effects on the reactivity in Sections 8 and 12.7.

2.2. Paradigmatic flows

We introduce now three examples of two-dimensional incompressible flows that exhibit the phenomenon of chaotic scattering discussed above, and which will be used as examples throughout this review: the flow around a cylindrical obstacle [78,229], the 'blinking vortex–sink' flow [8,81], and the case of four point vortices [140].

2.2.1. Flow around a cylinder: the von Kármán vortex street

The flow around an obstacle is a classic system in fluid mechanics [101,16,188]. We consider (viscous) incompressible flow around a cylinder of radius R, in the setup shown in Fig. 6b. Far away from the obstacle (that is, for $x \to \pm\infty$), the flow is expected to be uniform. We label the longitudinal flow direction by x, and the transverse direction by y.

Denoting by U the velocity for $x \to \pm\infty$, the Reynolds number associated with this flow can be defined as

$$Re = 2RU/\nu \ , \tag{7}$$

where ν is the fluid's kinematic viscosity. For Re sufficiently small, the flow is stationary. As U increases, Re also increases. When Re passes a critical value $Re_c \approx 80$, the stationary solution of the Navier–Stokes equation becomes unstable, and the flow becomes time periodic, with a velocity field satisfying $\mathbf{u}(\mathbf{r}, t + T) = \mathbf{u}(\mathbf{r}, t)$ with some period T [77]. If the Reynolds number is increased further, it will eventually reach values where the periodic regime is unstable, and more complicated space–time behavior sets in. For sufficiently high Re, the flow becomes turbulent. From now on we will concentrate on the time-periodic regime, because despite its simplicity, it displays chaotic advection.

Viscous vortices are created in the wake of the cylinder, detach from it and drift down the channel. They gradually lose strength because of viscosity, until after some distance they die out. New vortices are shed from the cylinder surface at intervals of half a period $T/2$, alternately above and below the middle of the cylinder (see Fig. 8). By this process, a *von Kármán vortex street* is formed behind the cylinder. In the following, for simplicity we assume that at any instant there are at most two vortices in the flow. In other words, the lifetime of each detached vortex equals one period T.

This flow was studied numerically by direct simulation of the Navier–Stokes equations at $Re = 250$, with the usual no-slip boundary conditions on the surface of the cylinder [77]. Because working directly with the Navier–Stokes equations is computationally time consuming, an analytical model for the flow in the time periodic regime has been proposed [78,229], which fits well the results of the direct numerical calculation. In this model, the stream function ψ is written as

$$\psi(x, y, t) = f(x, y)g(x, y, t) \ , \tag{8}$$

where the first factor

$$f(x, y) = 1 - \exp\{-a[(x^2 + y^2)^{1/2} - 1]^2\} \tag{9}$$

guarantees the no-slip boundary condition at the cylinder surface, whose radius has been taken to be unity (which can always be done by a suitable rescaling of the lengths). The term $a^{-1/2}$ plays the role of the width of the boundary layer. The time unit is chosen to be the period of the flow: $T = 1$. The second factor in Eq. (8) is

$$g(x, y, t) = -Wh_1(t)g_1(x, y, t) + Wh_2(t)g_2(x, y, t) + Uys(x, y) \ . \tag{10}$$

The first two terms model the alternating birth and subsequent death of the vortices. The maximum vortex amplitude is W, with time dependence

$$h_1(t) = |\sin(\pi t)|, \quad h_2(t) = h_1(t - \tfrac{1}{2}) \ . \tag{11}$$

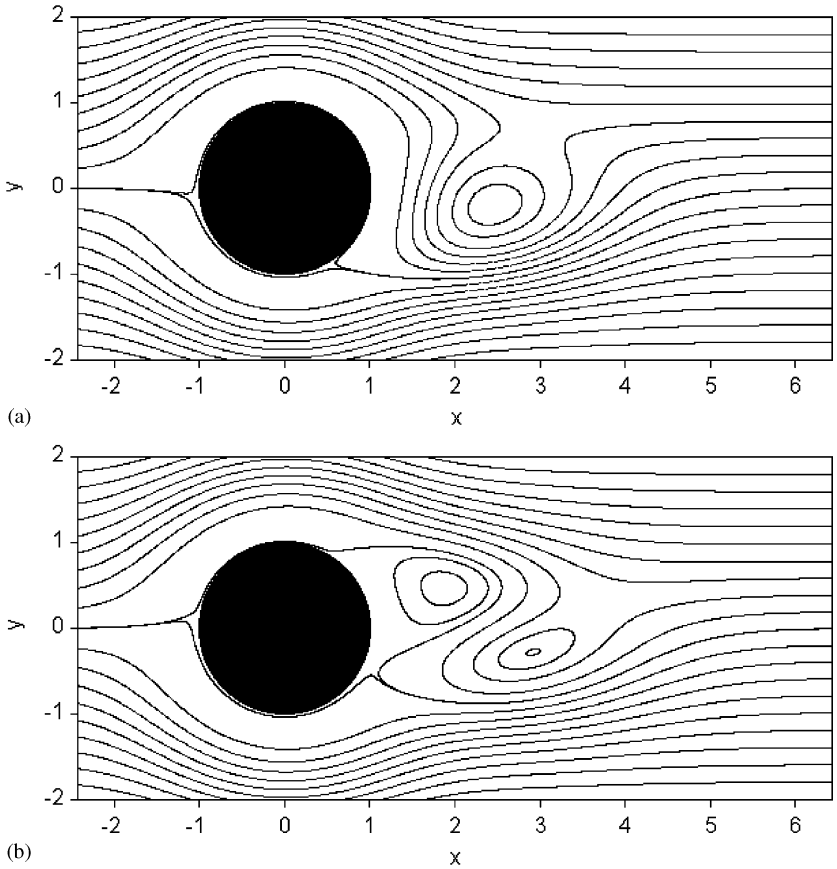

Fig. 8. Streamlines for the flow around a cylinder at two different times, separated by $T/4$, one quarter of the full period of the flow. The vortex shedding is clearly visible.

The vortices, having characteristic linear size $R_0^{-1/2}$, are of Gaussian shape:

$$g_i(x, y, t) = \exp(-R_0\{[x - x_i(t)]^2 + \alpha^2[y - (-1)^{i-1}y_0]^2\}), \quad i = 1, 2 \ , \tag{12}$$

whose centers move downstream by constant velocity

$$x_1(t) = 1 + L[t \bmod 1]; \quad x_2(t) = x_1(t - \tfrac{1}{2}) \ , \tag{13}$$

and where y_0 is the distance of the vortex centers from the x-axis. The last term in Eq. (10) arises from the background flow, and the screening factor

$$s(x, y) = 1 - \exp[-(x - 1)^2/\alpha^2 - y^2] \tag{14}$$

ensures that the effect of the background flow velocity U is reduced in the wake. This analytic model has several parameters, which have been set as $a = 1$, $\alpha = 2$, $R_0 = 0.35$, $L = 2$, $y_0 = 0.3$, $U = 14$, and $W = 24$, to fit the numerical solution. We will see that our results are robust with respect to the particular dynamics, and so the exact values of the parameters are not so important. With this model, the stream

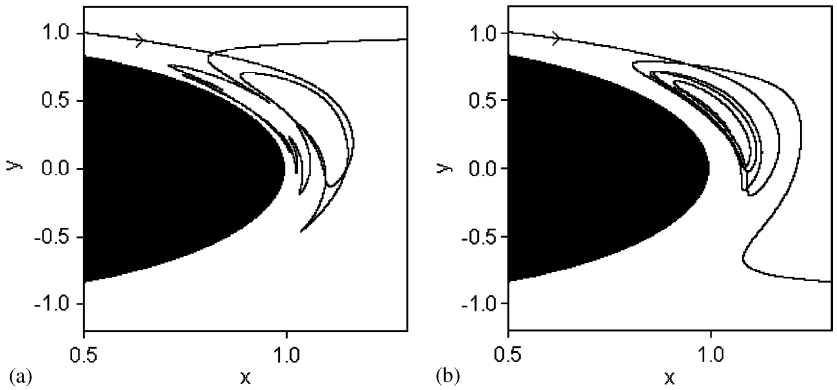

Fig. 9. Trajectories corresponding to two very close initial conditions, in the cylinder flow. The black region is the cylinder, which is distorted into an elliptical shape because of the coordinates used in the figure. The sensitivity to initial conditions is a clean indication of chaos.

function is given by Eq. (8) as a function of space and time, and can be directly used in Eq. (3) to find the motion of passively advected particles by numerical integration.

Using this analytic model, we can investigate the dynamics of particles advected by the flow around a cylinder. In both the far upstream and far downstream directions ($x \to \pm\infty$), the particles move downstream along straight lines. Only in the near wake of the cylinder is the flow non-trivial, being time dependent because of the vortex shedding. Therefore, advection in this flow is a scattering process, and the mixing region is the time-dependent part of the flow, situated within an area of finite extension (of length L) in the wake. This model serves thus as an ideal paradigm for a large class of open chaotic flows. To illustrate the chaotic nature of particle motion in this flow, Fig. 9 shows trajectories corresponding to two very close initial conditions. It may be observed that the particles leave the mixing region by totally different routes.

We finish by noting that a careful experimental investigation of passive advection in the wake of a cylinder has been carried out by Sommerer and coworkers [195]. They determined the escape rate and the Lyapunov exponent of the transiently chaotic dynamics, as well as, the asymptotic fractal dimension of dye droplets. Furthermore, the von Kármán vortex street is not a particular property of cylindrical obstacles. Most (approximately) two-dimensional flows past an obstacle have this property, provided that their Reynolds number is in the appropriate range. Thus, von Kármán vortices are found in many real situations. Fig. 10 displays the cloud pattern in the wake of the island of Guadalupe which traces out the unstable manifold due to the von Kármán vortices. In this case, the mountain on the island plays the role of an obstacle in the flow of the wind. Fig. 11 shows dye patterns obtained in a simulation of the sea current around the island of Grand Canaria [9]. Fractal filaments generated by the von Kármán vortices are, again, prominent.

2.2.2. Blinking vortex–sink flow

The blinking vortex–sink system [8,81] models the *outflow* from a large bath tub with two sinks that are opened in an alternating manner. One of these sinks is modeled by a point vortex superimposed on a point sink acting in an infinite plane of ideal fluid. This model corresponds to the observation that a rotational flow is formed around the sink in the course of drainage.

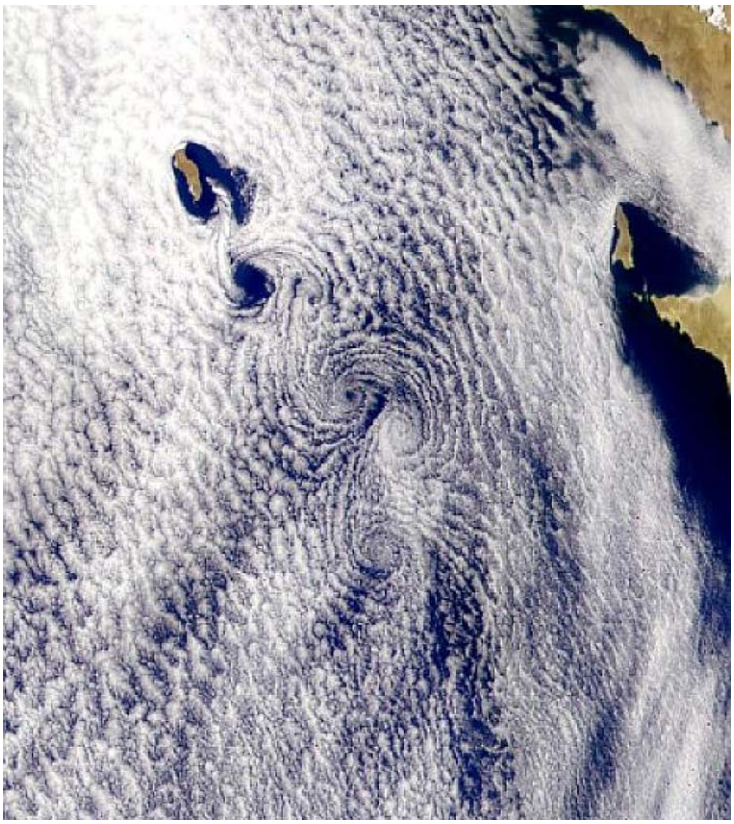

Fig. 10. (Color online.) Cloud patterns around Guadalupe Island, August 20, 1999 (NASA SEAWIFS image).

The complex potential [92] for a sinking vortex point located at the origin can be written as

$$w(z) = -(C + \mathrm{i}K)\ln z\ , \tag{15}$$

where z is the complex coordinate in the plane of the flow. Here $2\pi C$ is the sink strength, i.e., the amount of fluid drained by the sink in unit time, and $2\pi K$ is the circulation measuring the vortex strength. The velocity field corresponding to $w(z)$ consists of the superposition of a radial component $v_r = -C/r$ and of a tangential component $v_\varphi = K/r$, where r is the distance from the origin. The imaginary part of the complex potential, $\psi = -K\ln r - C\varphi$ is the stream function [92]. The streamlines (the level lines of ψ) are logarithmic spirals: $\varphi = -K/C\ln r + \text{const}$.

A passively advected tracer particle follows the velocity field of the flow without any delay. Its equations of motion in polar coordinates are

$$\dot{r} = v_r, \quad \dot{\varphi} = v_\varphi/r. \tag{16}$$

By solving these equations with initial conditions (r_0, φ_0), we find

$$r(t) = (r_0^2 - 2Ct)^{1/2}, \quad \varphi(t) = \varphi_0 - \frac{K}{C}\ln\frac{r(t)}{r_0}\ . \tag{17}$$

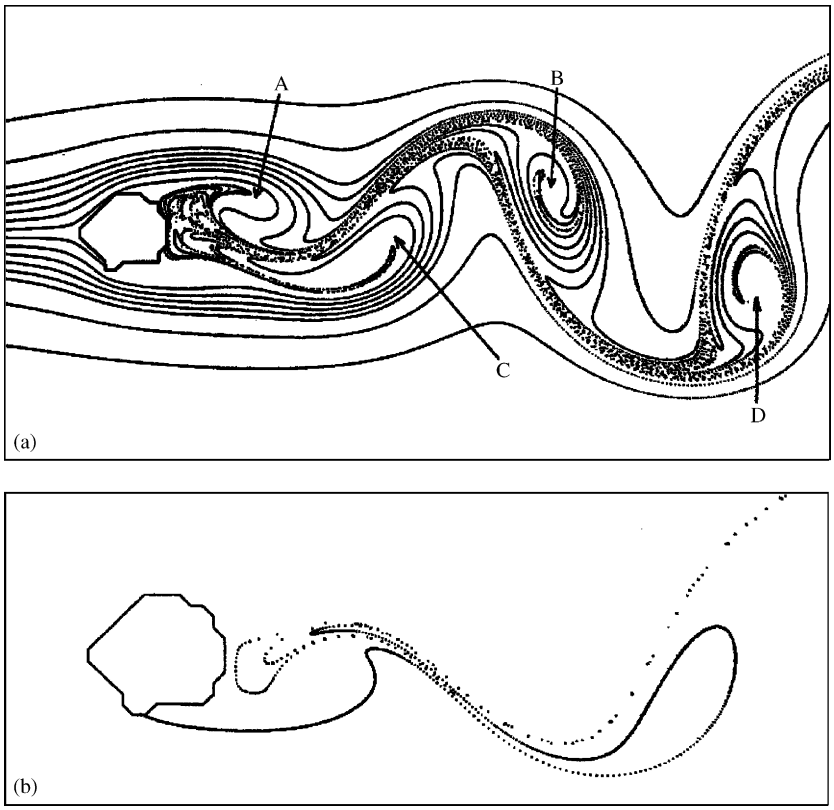

Fig. 11. Patterns of a sea current around Gran Canaria island. The black lines are traces of continuously injected die obtained in a numerical simulation. Several streaklines are shown in panel (a), and a single such streakline is shown in panel (b). Many of the streaklines trace out a fractal pattern, the unstable manifold of the chaotic saddle in the wake of the island. From [9], with permission.

The particles move along streamlines, since the flow is stationary. In the complex representation, a position in the (x, y) or (r, φ) plane corresponds to a complex number z, given by $z = r\exp(\mathrm{i}\varphi)$ in polar coordinates. We obtain that a tracer particle starting at a point z_0 will arrive, after time t, at

$$z(t) = z_0\left(1 - \frac{2Ct}{|z_0|^2}\right)^{1/2-\mathrm{i}K/2C} . \tag{18}$$

Because the motion is undefined after reaching the sink center, the time in this expression is limited from above:

$$t \leqslant |z_0|^2/(2C) . \tag{19}$$

With this condition, Eq. (18) uniquely describes the advection dynamics.

The blinking vortex–sink system [8,81] is obtained by having two such sinking vortex points some distance apart from each other, both being alternately active for a duration of $T/2$ each. In this system the velocity field is periodic in time with period T, but in a special way: it is stationary for half a period

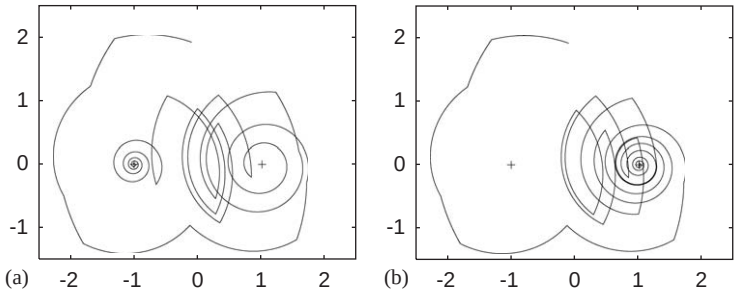

Fig. 12. Trajectories corresponding to two very close initial conditions, in the blinking-vortex flow. For the initial condition (a), the particle falls into the left sink, whereas in (b) it falls in the right one.

and stationary again but around another vortex point for the next half period $T/2$. The velocity field corresponds to a sinking vortex flow centered at $z=-a$ and at $z=a$ in the time intervals $(0, T/2]$ and $(T/2, T]$, respectively. Because of this alternating action, the flow as a whole is no longer stationary, since there are jumps in the velocity field at each half period.

The tracer motion can be easily built up from Eq. (18). A trajectory starting at $t=0$ follows the corresponding streamline up to $t=T/2$, when the velocity field suddenly changes. It finds itself on another streamline that will be followed for the next time interval of length $T/2$. Thus, on a time scale of several periods, the trajectory will have several break points and its path can be much more complicated than any of the streamlines. Fig. 12 presents two such trajectories.

Since the velocity field is periodic, it is convenient to monitor the particle motion on a *stroboscopic map* obtained by recording the position of particles after integer multiples of T only. In this section, we choose the starting time by taking stroboscopic snapshots at $t_0=0$, corresponding to the instant when the right sink is switched off. For the tracer position at $t=T/2$ and T, we obtain from Eq. (18) by a simple coordinate transformation the two pieces of the solution

$$z(T/2)=(z_0+a)\left(1-\frac{CT}{|z_0+a|^2}\right)^{1/2-\mathrm{i}K/2C}-a$$

and

$$z(T)=(z(T/2)-a)\left(1-\frac{CT}{|z(T/2)-a|^2}\right)^{1/2-\mathrm{i}K/2C}+a\ , \tag{20}$$

respectively. By introducing dimensionless coordinates via $z\to az$, one notices that the dynamics is fully specified by two parameters:

$$\eta=CT/a^2 \quad \text{and} \quad \xi=K/C, \tag{21}$$

the dimensionless sink strength and the ratio of the vortex to sink strength, respectively. The locations of the sinking vortex points are $z=\pm 1$ in the new dimensionless units.

The rule connecting the coordinates on snapshots taken at $t=0$ and T is exactly the same as for the $t=nT$ and $(n+1)T$ stroboscopic instants. By introducing $z_n\equiv z(nT)$ as the particle position after n

periods, we obtain the general form of the discrete-time advection dynamics as

$$z_{n+1} = (z'_n - 1)\left(1 - \frac{\eta}{|z'_n - 1|^2}\right)^{1/2 - i\xi/2} + 1,$$

where

$$z'_n = (z_n + 1)\left(1 - \frac{\eta}{|z_n + 1|^2}\right)^{1/2 - i\xi/2} - 1 \tag{22}$$

is a dummy variable corresponding to the particle position at $t = (n + \frac{1}{2})T$. It is the jump in the flow field at $t = T/2 \bmod T$ that makes the submaps connecting z_n to z'_n, and z'_n to z_{n+1} different.

We note that due to the alternating character of the flow, *effective sink cores* are formed. Tracers which are inside a circle of radius $R = \sqrt{\eta}$ around any of the sinks at the instant when it starts to be active, will leave the system in the next time interval of $T/2$, and we do not follow their dynamics any longer. This formally corresponds to having infinitely strong dissipation within the sink cores. Thus, the sink cores are extended non-chaotic *attractors* of the advection map (although the time continuous tracer dynamics possesses point attractors only, the two centers). Therefore, Eqs. (22) are valid outside of these sink cores only. Here, however, the map has Hamiltonian character: it is area preserving and invertible.

Fig. 13 shows the various chaotic sets for a particular time. Their shape changes in time with period T, as can be seen in Fig. 14 for the unstable manifold. This complex fractal structure is the hallmark of chaotic scattering, and is associated with the sensitivity of the trajectories of the system to initial conditions. This is also illustrated by Fig. 12 where two initially very close trajectories end up falling in different sinks.

The closed version of the blinking vortex–sink flow, the blinking vortex flow [7], can experimentally be generated via two parallel cylinders rotated alternately in a viscous fluid [201]. To our knowledge, the vortex–sink flow has not yet been realized in a laboratory.

2.2.3. Point vortices

An important class of models in the area of fluid dynamics is that of N point vortices moving in a two-dimensional ideal flow [99,163,147]. Each point vortex is defined by a position (x_i, y_i), with $1 \leqslant i \leqslant N$. A point vortex at (x_i, y_i) generates a flow field given by

$$u_x = -\Gamma_i y/R_i, \quad u_y = \Gamma_i x/R_i \ , \tag{23}$$

where $R_i = \sqrt{(x - x_i)^2 + (y - y_i)^2}$ is the distance of point (x, y) at which the velocity field is being calculated from the vortex center (x_i, y_i), and Γ_i is the *vortex strength* of the vortex i. For $N \geqslant 2$, the flow field is given by the linear combination of the fields generated by each individual vortex. Note that the flow field is singular at the vortex centers (x_i, y_i).

In the N vortex problem ($N \geqslant 2$), each vortex is affected by the flow generated by the other vortices. As a consequence of Kelvin's circulation [101,16] in ideal flows, the strength Γ_i of each vortex is preserved. The vortex centers (x_i, y_i), however, become functions of time, moving according to the flow field generated by the other $N - 1$ point vortices. It can be shown [16,147] that the equations of motion for the point vortices are given by

$$\Gamma_i \dot{x}_i = \frac{\partial H}{\partial y_i} \ , \quad \Gamma_i \dot{y}_i = -\frac{\partial H}{\partial x_i} \ . \tag{24}$$

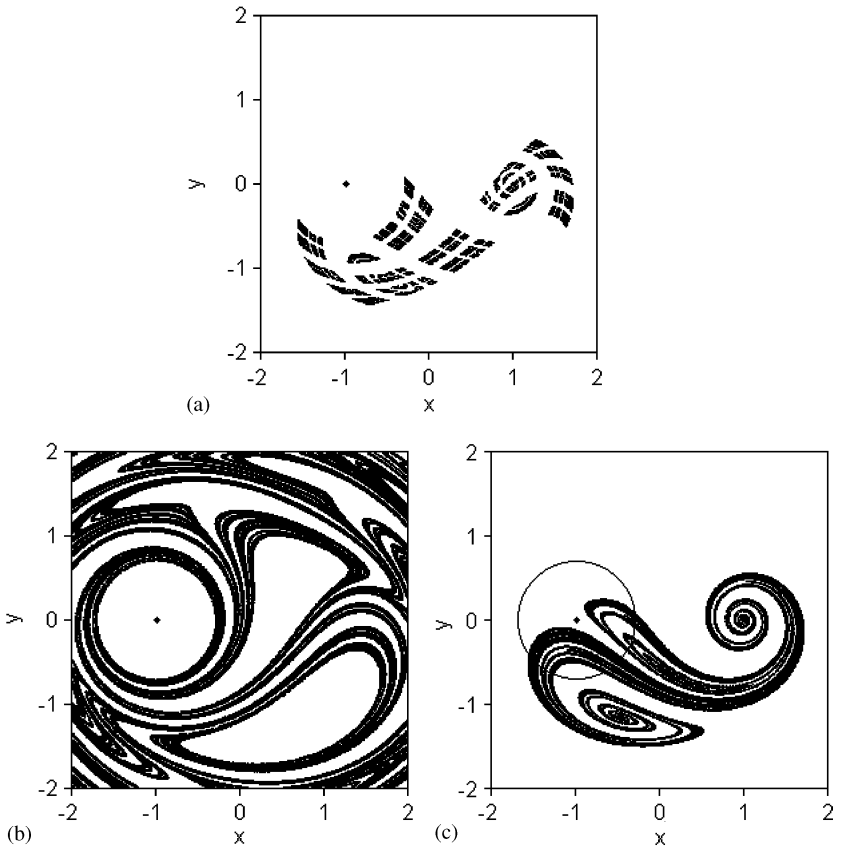

Fig. 13. Snapshot of the (a) chaotic saddle, (b) stable manifold, and (c) unstable manifold in the blinking vortex–sink flow ($\eta = 0.5$, $\eta = 10$). The circle in (c) shows the area that is drained during the next half time period.

Here the function $H = H(x_1, y_1, \ldots, x_N, y_N)$ is

$$H = -\frac{1}{\pi}\sum_{i<j} \Gamma_i \Gamma_j \ln r_{ij} \ , \tag{25}$$

and $r_{ij} \equiv \sqrt{(x_i - x_j)^2 + (y_i - y_j)^2}$ is the distance between vortices i and j. Eqs. (24) and (25) have a Hamiltonian structure, with the Hamiltonian H. The motion of the vortices is typically aperiodic and chaotic for $N \geqslant 4$. If the total vorticity vanishes, $\sum_{i=1}^{N} \Gamma_i = 0$, the vortices remain close to each other, but on average they undergo an overall drift. In a reference frame co-moving with the vortices, the flow can be considered to be open, and advected particles undergo a scattering process [40,157,140].

The flow generated around the moving vortices is governed by the stream function $\psi = \psi(x, y, t)$ given by

$$\psi = -\frac{1}{\pi}\sum_{i=1}^{N} \Gamma_i \ln r_i(t) \ . \tag{26}$$

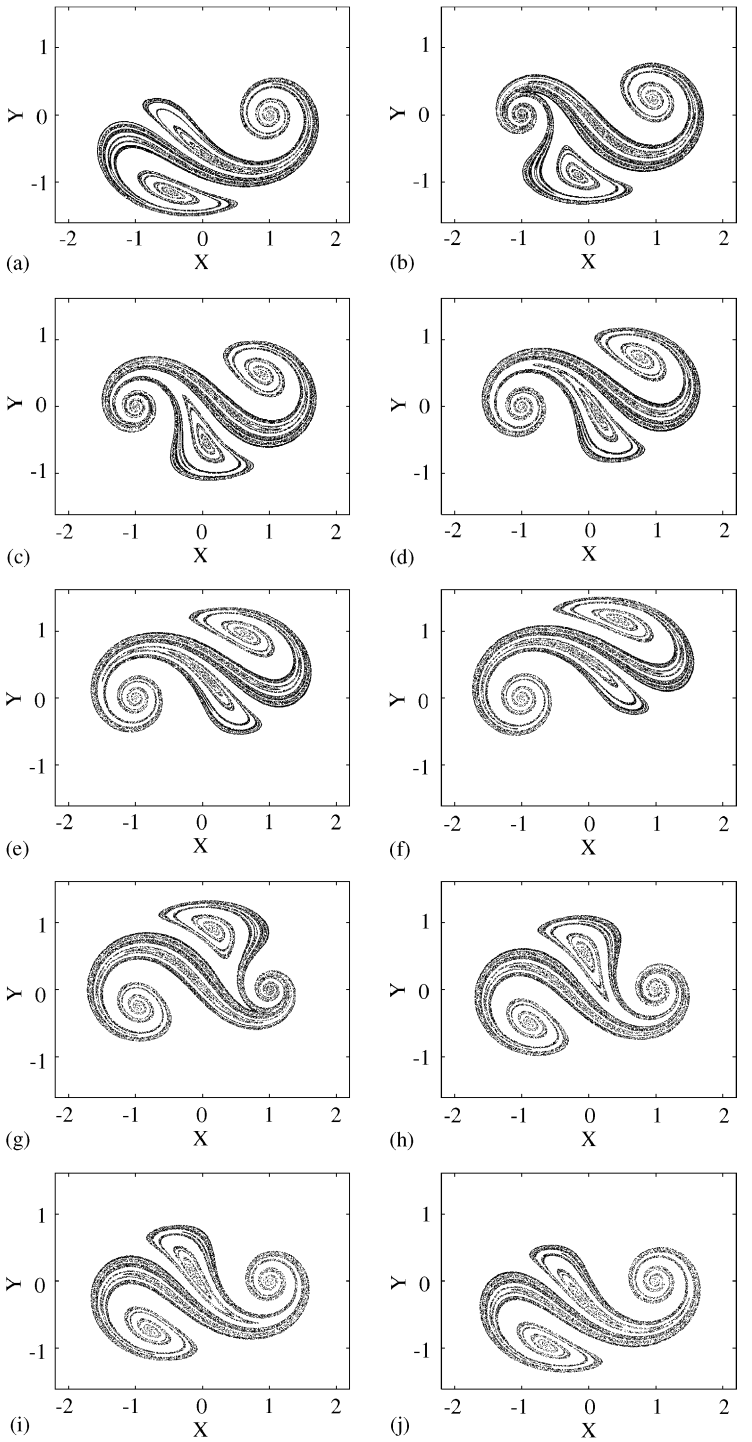

Fig. 14. Time evolution of the unstable manifold in the blinking vortex–sink system. The snapshots were taken at (a) $t = 0$, (b) $t = T/10$, (c) $t = 2T/10$, (d) $t = 3T/10$, (e) $t = 4T/10$, (f) $t = 5T/10$, (g) $6T/10$, (h) $7T/10$, (i) $8T/10$, (j) $9T/10$. Note that at $t = T$ we recover (a), the shape of the unstable manifold changes periodically in time.

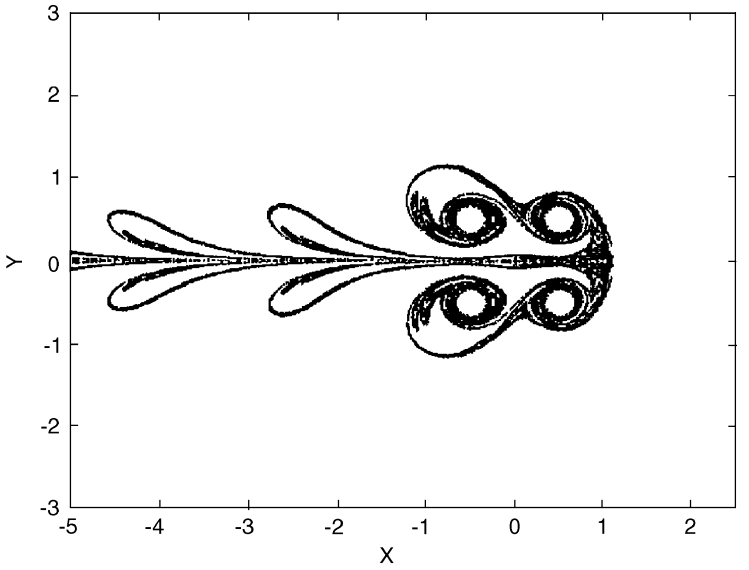

Fig. 15. Unstable manifold of the chaotic saddle developing in the advection problem of two periodically leapfrogging vortex pairs [157] ($\Gamma_1 = \Gamma_2 = -\Gamma_3 = -\Gamma_4$) with the x-axis as their common symmetry axis during the entire vortex motion. For vortex strengths not all identical in modulus and zero resulting vorticity, the fractal pattern remains topologically similar, but much less symmetric (cf. the backbone of the distribution of Fig. 34).

Here r_i is the distance of the advected particle from the ith vortex of center (x_i, y_i). For $N \geqslant 4$, the flow field associated with the vortices is therefore aperiodic. We shall use this example (with $N = 4$) to illustrate the theory for reactions in non-periodic flows, in Section 7.

We note that the advection dynamics is already chaotic in the flow field of $N \geqslant 3$ vortices [7]. Fig. 15 illustrates this by exhibiting the fractal unstable manifold of a symmetrically arranged four-vortex problem.

Vortices behaving over finite time scales very similar to ideal point vortices can be generated in stratified fluids [63], and vortex systems with zero resultant vorticity are easy to produce. An experiment visualizing the leapfrogging motion of two vortex rings in air was carried out more than two decades ago [224]. The smoke pattern (cf. Fig. 79 of [213]) is very similar to Fig. 15 and clearly shows a filamentary structure, to be called in current terminology, the unstable manifold of the chaotic saddle existing in between the smoke rings.

3. A basic model of activity: autocatalytic process

3.1. Relevance

First we restrict our attention to autocatalytic reactions, which occur often in Nature [43]. They are generic models of infection-like processes, or more precisely, of the penetration of a stable phase B into an unstable one A. The reaction scheme is

$$\mathrm{A} + \mathrm{B} \to 2\mathrm{B} \ . \tag{27}$$

This reaction typically propagates in the form of fronts of some velocity v with relatively sharp boundaries [94,143].

In chemical systems autocatalysis leads to explosive reactions, e.g., to a sudden color change [43]. Autocatalytic reactions, when coupled to other reactions, can give rise to such complex behavior as multiple steady states, hysteresis, periodic oscillations or chaos. The famous Belousov–Zhabotinsky reaction [228] also contains an autocatalytic step. During the last decades, several other autocatalytic chemical reactions have been investigated.

The first evidences for the influence of the stirring rate on the reaction's outcome have been found within the class of nonlinear reactions [172,111,122,173]. The interaction of mixing with autocatalysis has been shown to give rise to new phenomena as stochastic behavior [135] and chiral symmetry breaking [95]. The first studies have been devoted to some global effects of imperfect mixing on the reaction. It has been the sensitive dependence of the optical activity in [95] on the initial conditions which gave motivation to Metcalfe and Ottino [125] to carry out the first study on the interplay between reaction and chaotic advection (in a closed flow).

Among environmental processes, in the simplest approximation, both ozone depletion [41,223,96] and plankton replication [117,116,25] can be described by front propagation of this type. In the first case, ClO-rich polar air catalytically depletes ozone under the influence of light. However, chlorine can be deactivated via the NO_2-rich air of the mid-northern latitudes, and the nonlinear interaction of these processes might play a role in controlling the effective amount of ozone in the stratosphere. A striking phenomenon related to the second example is plankton blooming, a sudden increase of the plankton population in seas and oceans conditioned on certain environmental changes. A further example is combustion, i.e., the propagation of a flame front separating unburned premixed reactants (A) and burned gases (B) [219].

In our models of autocatalytic reactions taking place in flows, both components A and B are considered to be made of constituents advected by the flow. Component A is assumed to be uniformly available, and hence a single seed of B is sufficient to trigger an extended reaction. In a closed container, B spreads until it eventually takes over all the available space. In an open flow, however, B particles are lost due to outflow, and there is a non-trivial product distribution. The simplest example is that of a homogeneous flow of velocity U, where the stationary B-distribution is a cone behind a fixed single B-seed (see Fig. 16).

3.2. Individual modeling (particles)

The individual, or kinetic-theory-type modeling [125] uses point particles as basic elements of the reactions. If two particles of different type come closer than a threshold distance, then they can react. This distance is called the *reaction range*, and is denoted by σ. Alternatively, σ can also be considered as the size of the reacting particles.

For practical reasons it is convenient to assume that reactions instantaneously occur at certain times only. The time difference between reactions is the time lag τ. At integer multiples of τ, the autocatalytic activity of B particles converts all the A particles within a radius σ into B particles. During a period of length τ, between two subsequent reactions, the particles are passively advected by the flow of given velocity field $\mathbf{u}$.

Although autocatalytic reactions can be treated by appropriate partial differential equations of the advection–reaction–diffusion type (see the following subsection), individual modeling of the reacting particles has been shown to be unavoidable in processes where strong particle number fluctuations exist

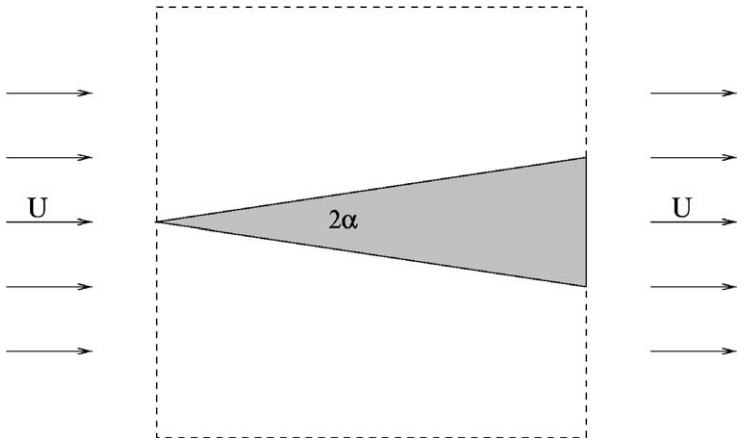

Fig. 16. Stationary B-distribution in a homogeneous flow behind a single fixed B particle. The half angle of the cone is $\alpha = \arcsin v/U$ for $v < U$, where v is the reaction front velocity, and U is the uniform flow velocity.

[227,182,66,110], as well as in the case where inertial effects of the advected reacting particles are included (see Section 9).

The present microscopic discrete-time model goes over into a time-continuous description if the limit $\tau \to 0$ is taken. In this limit, however, the reaction range σ should also go to zero (otherwise a singular spreading of B would be possible). The limit is thus only meaningful if the ratio σ/τ remains finite, i.e., if the *reaction velocity*

$$v = \lim_{\sigma,\tau\to 0} \frac{\sigma}{\tau} \tag{28}$$

remains well defined.

3.3. Continuum modeling with concentrations

The continuum modeling uses concentrations a and b of particles A and B, respectively. We consider them as particle number concentrations, and use their dimensionless versions. Locally, the reaction equations are

$$\frac{\mathrm{d}a}{\mathrm{d}t} = -k_0 ab, \quad \frac{\mathrm{d}b}{\mathrm{d}t} = k_0 ab\ , \tag{29}$$

where k_0 denotes the reaction rate, with dimension 1/time. Since the total number of particles (number of A particles + number of B particles) is conserved, the sum $a + b$ of concentrations is a constant of the reaction. We can thus consider the proportion

$$c \equiv \frac{b}{a+b} \tag{30}$$

of component B as a new variable. The value of c ranges from 0 (A component only) to 1 (when all material is converted into B). Its time evolution is given by

$$\frac{\mathrm{d}c}{\mathrm{d}t} = kc(1-c) \ , \tag{31}$$

which is a logistic growth with reaction rate $k = k_0(a+b)$.

The corresponding diffusion–reaction equation for concentration c in a medium at rest is

$$\frac{\partial c}{\partial t} = kc(1-c) + D_{\mathrm{diff}}\nabla^2 c \ , \tag{32}$$

where D_{diff} denotes the diffusion coefficient. This is the so-called Fischer–Kolmogorov–Petrovsky–Piskunov (FKPP) equation [49,94] which contains two basic parameters: the *reaction rate* and the *diffusion coefficient*. They determine the front velocity v: the stable phase ($c = 1$) penetrates into the unstable one ($c = 0$) with a velocity [94,49] which is proportional to the geometric mean of the reaction rate and the diffusion coefficient:

$$v = \alpha\sqrt{kD_{\mathrm{diff}}} \ , \tag{33}$$

where $\alpha = 2$. The transition between the concentration values $c = 0$ and 1 takes place in a narrow spatial range whose width is of order $\sqrt{D_{\mathrm{diff}}/k}$. Since in most cases of interest this range is very small, it can be said that the stable phase ($c = 1$) propagates into the unstable phase ($c = 0$) through a well-defined front, which moves with velocity v given by Eq. (33).

In the presence of a fluid flow of velocity $\mathbf{u}(\mathbf{r}, t)$, the time derivative $\partial c/\partial t$ is to be replaced by the total hydrodynamical time derivative of the concentration, and the full advection–diffusion–reaction equation for concentration c reads as

$$\frac{\partial c}{\partial t} + (\mathbf{u}\cdot\nabla)c = kc(1-c) + D_{\mathrm{diff}}\nabla^2 c \ . \tag{34}$$

This is the equation which is to be solved in the study of autocatalytic reactions in flows. It is a first approximation only, being based on the assumption that the reaction does not affect the flow. Also, it does not take into consideration the size and the inertia of the particles (see Section 9).

4. Autocatalytic reactions in open 2D flows

In this section, we study the autocatalytic reaction in open flows, as one of the simplest kinds of active chaos. We first describe the results of some numerical experiments, using both the flow around a cylinder (Section 2.2.1) [209,83,105] and the blinking-vortex flow (Section 2.2.2). We then develop a general theory for the reaction dynamics of this system [209,83,205,206]. In spite of its simplicity, this theory predicts the main dynamical features of active chaos.

4.1. Numerical results

We first consider the flow around a cylinder. Since the flow is periodic, we fix the 'phase' of the reaction relative to the flow. We consider time zero, $t = 0$, to be the instant when a vortex is born close to the

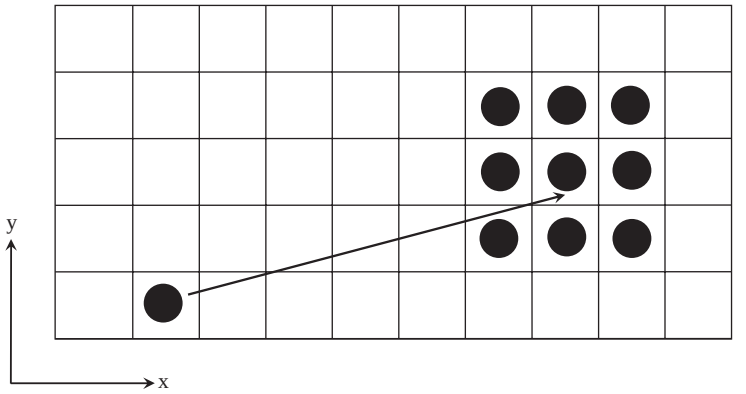

Fig. 17. Illustration of the 'infection' scheme to simulate numerically an auto-catalytic reaction. The arrow indicates the transport of the particle by advection, after which it infects the eight neighboring cells.

surface of the first quadrant of the cylinder and, simultaneously, the other vortex is in its fully developed state (see Section 2.2.1 for details).

For convenience, we carry out the simulations on a uniform rectangular grid of lattice size ε_0 covering both the incoming flow and the mixing region in the wake of the cylinder. This ε_0 also corresponds to the average distance between nearest-neighbor particles, and is considered for simplicity to be the same as the reaction range σ (see Section 3). If there is a tracer inside a cell, it is always considered to be at its center. This projection of the tracer dynamics on a grid defines a mapping among the grid cells.

The course of the reaction starts with nearly all cells occupied by component A, the background material. Initially, only a few cells contain B. One iteration of the process consists of two mappings in involution. The first mapping describes the advection of the particles on the chosen grid over some time lag τ, while the second corresponds to the instantaneous chemical reaction occurring on the same grid of cells. If a cell contains B at the time of the reaction, all of the 8 neighboring cells are infected by B. This process is illustrated in Fig. 17.

Initially, we introduce a seed of reagent B in front of the cylinder. Since there are only two species in the system, we monitor only reagent B. Values referring to material A inside the computational domain can be obtained from mass (in our two-dimensional model, area) conservation. Fig. 18 displays the spreading of reagent B (black) in the course of time. Note the rapid increase of the B area and the quick formation of a filamentary structure that becomes steady after a few time units, but changes periodically with the period of the flow. A comparison with Fig. 16 illustrates the basic difference in the reaction outcome in simple and in chaotic flows. Note that the seed is not fixed in the present case.

Fig. 19 shows the number of B particles in the computational domain as a function of time. After four periods, a self-repeating periodic oscillation sets in around a mean value. This means that the chemical reaction takes over the flow's basic periodicity and reaches a steady state: the number of particles being born in the reaction is the same as the number of particles escaping due to outflow. In fact, since the flow is reflection symmetric with respect to the x axis after a time shift of one-half, the product distribution repeats itself with a period of $\frac{1}{2}$ of the flow's period.

The outcome of the dynamics depends strongly on whether the initial droplet intersects with the stable manifold of the saddle. If the initial B droplet is too much off axis [as in Fig. 20a], it does not penetrate the

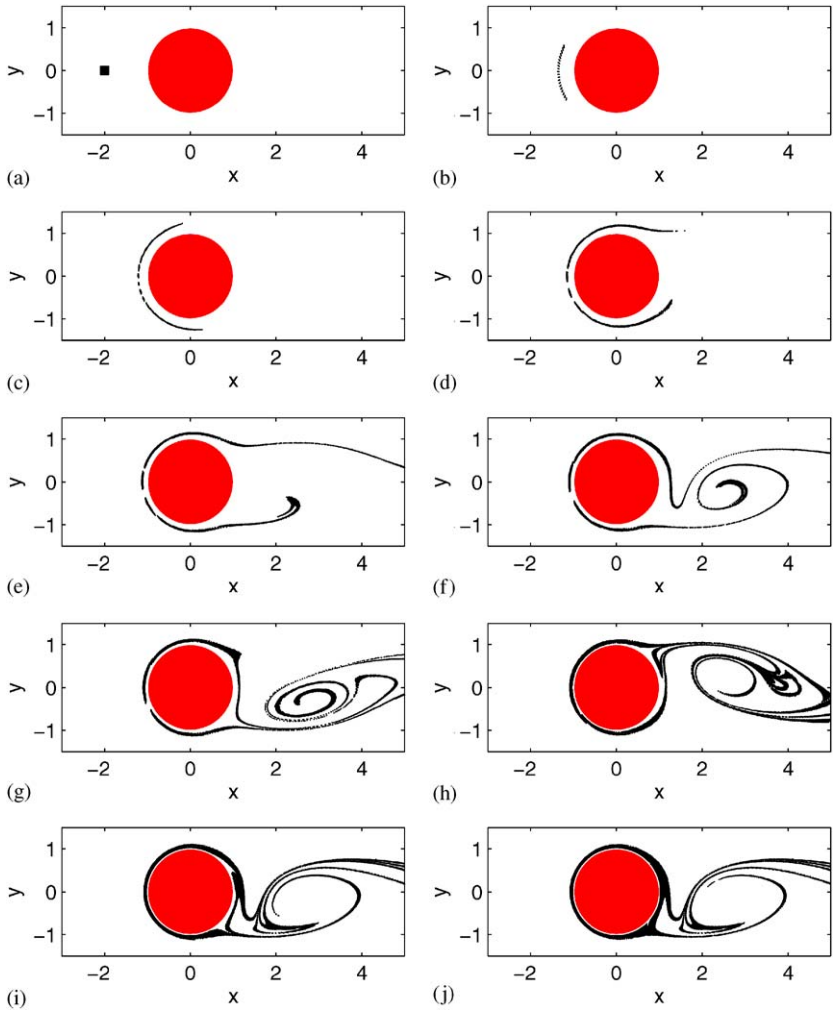

Fig. 18. Time evolution of a blob of B particles (black), initially placed close to the cylinder, interacting auto-catalytically with the surrounding A particles (white). The snapshots (a–j) are taken at times $t = 0$, 0.2, 0.4, 0.6, 0.8, 1.0, 1.2, 1.6, 2.0, and 3.0, respectively, right before a reaction takes place. ($T = 1$ is the period of the flow.)

mixing region in the wake of the cylinder, and the whole amount of B is washed away downstream. One can observe, of course, that the size of the compact patch B increases due to the autocatalytic process as time goes on. Note that in this case no material B remains in the mixing region and the reaction dynamics dies out in any fixed observation region of finite size. To sharpen the contrast, in Fig. 20b we display the B distribution of Fig. 18j in a much longer region downstream. This clearly indicates that material B is now present at *any* instant of time at *any* x-value in the wake (after long enough time). The gradual broadening of the stripes of product downstream is due to the autocatalytic feature of the process. It is worth emphasizing that whenever the initial droplet overlaps with the stable manifold, the long-term reaction dynamics are all similar, and the outcome is independent of the precise initial conditions.

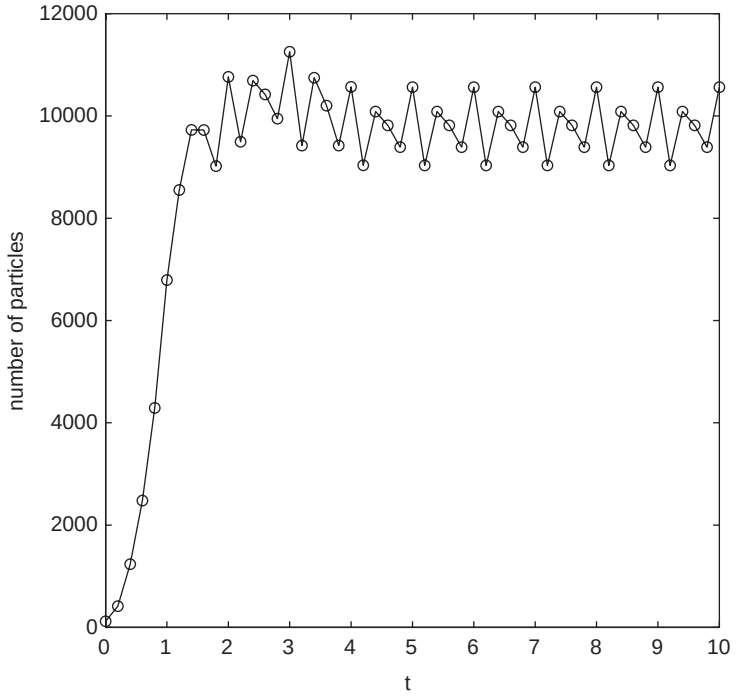

Fig. 19. Time dependence of the number of B particles in the region shown as in Fig. 18.

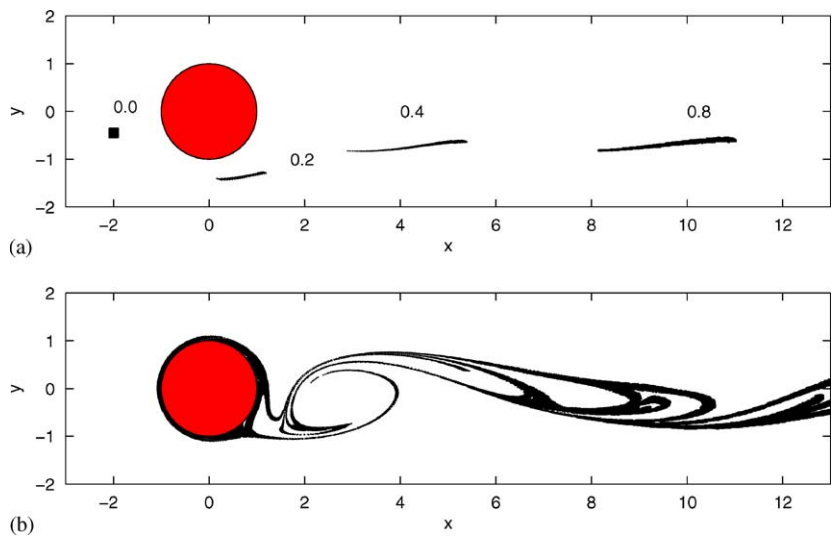

Fig. 20. (a) Time dependence of an initially off-axis B blob. The numbers indicate the time instants when the snapshots of the blobs are taken. (b) The shape of a blob initially overlapping with the stable manifold at time $t = 3$, the same as Fig. 18j but in a different frame, and approximates well the unstable manifold.

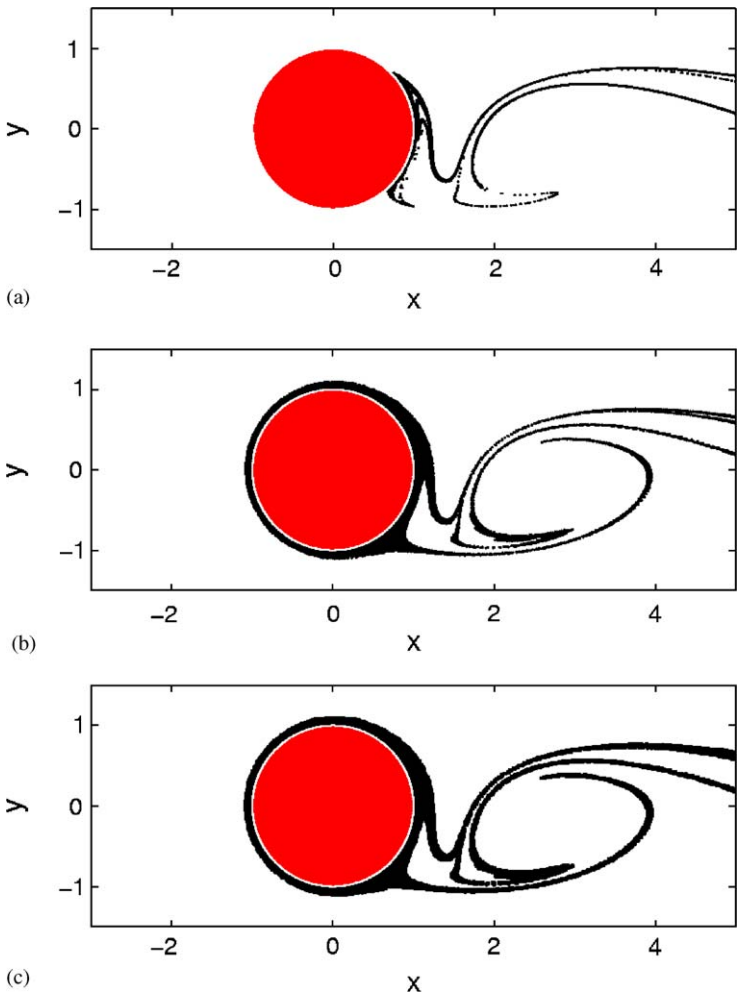

Fig. 21. (a) The unstable manifold of the chaotic saddle in the reaction free flow generated by distributing 20.000 particles (black dots) on short segments along the local unstable direction of three basic periodic orbits of the advection dynamics, and iterating them forward in time over several periods. Panels (b) and (c) show the B-distribution at $t = 10.0$ just before and just after the reaction, respectively.

In what follows, we focus on the nontrivial cases when the droplet penetrates the mixing region. To understand the dynamics of Fig. 18, we recall that the tracer dynamics is governed by a chaotic saddle in the wake of the cylinder. Passive tracers coming close to the chaotic saddle spend a long time in the mixing region before being advected away along the unstable manifold of the chaotic saddle, shown in Fig. 21a. Thus tracers having spent a long time in the mixing region accumulate on the unstable manifold. A comparison between Figs. 18i,j and 21a provides numerical evidence for the accumulation of the product material B in stripes of finite widths along this manifold.

In order to gain further insight into the reaction dynamics, Figs. 21b and c show the reagent distribution just before and just after the occurrence of the autocatalytic reaction, respectively, in the steady state.

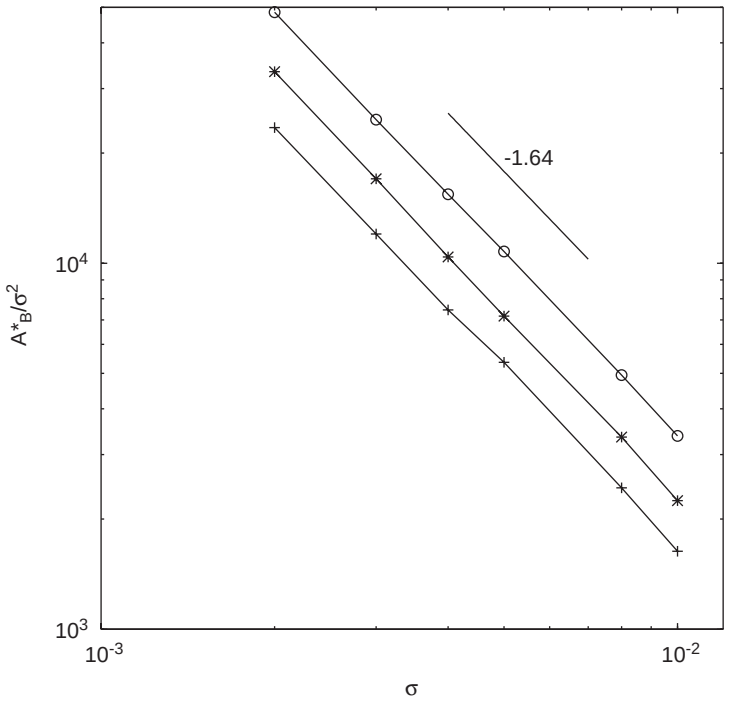

Fig. 22. The area occupied by the B particles in the steady state, at different values of the reaction time lag τ ('o' $\tau = 1$, '*' $\tau = 2$, '+' $\tau = 3$) as a function of the grid size chosen to be the reaction range σ. The scaling with σ is found to be $\mathscr{A}_{B^*} \sim \sigma^{2-D}$, with $D = 1.64$, which is in close agreement with the fractal dimension of the unstable manifold of the reaction free flow.

In the first case, the B distribution has a rather scanty appearance, while right after the autocatalytic reaction, a sudden widening of the B stripes occurs. The two pictures correspond to two different coverages of the fractal manifold. The sudden increase of the coverage width at certain times is due to our modeling of the chemical reaction as a 'kicked' process. In the case of time continuous reaction obtained in the limit $\tau \to 0$ this feature is not present, but the fact that material B occupies a fattened-up fractal remains unaltered.

The fact that the B particles define a fractal coverage is confirmed by Fig. 22, which shows the scaling of the area occupied by the B particles, as a function of the grid size used in the simulation. It is seen in Fig. 22 that the scaling is compatible with the fractal dimension of the unstable manifold of the underlying advection dynamics.

Finally we illustrate the same reactive process in the blinking vortex–sink flow, see Fig. 23. Although the flow is completely different, the fact that advected autocatalytic particles are accumulating along a fractal set, the unstable manifold, remains the same.

4.2. Basic theory: the bandwidth dynamics

Now we develop a continuous-time model to describe the reaction dynamics. To do this, we follow the history of a blob of reactive material (B) which intersects the stable manifold of the chaotic saddle

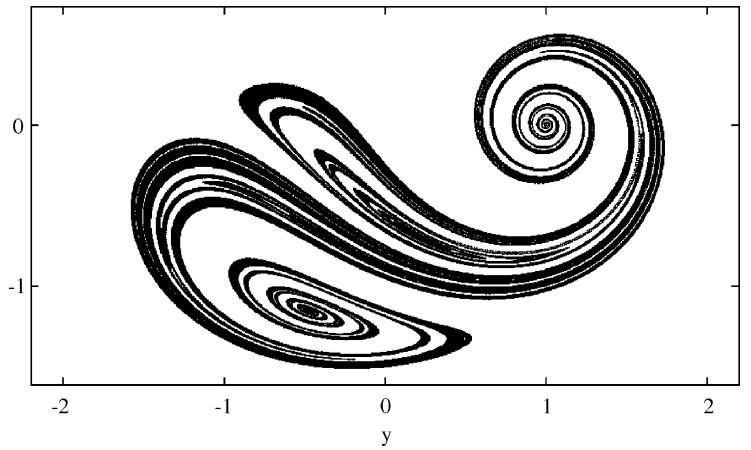

Fig. 23. Snapshot of the autocatalytic reactions in the blinking vortex–sink system. The product traces out a fattened-up copy of the unstable manifold, cf. Fig. 14a (parameters as in that figure).

associated with the advection dynamics. This blob is advected by the flow, and after some time t_c, the material B of the blob will be distributed in the mixing region along filaments, in bands along the unstable manifold. Without reaction, the width of these bands converges to zero, due to the stretching of material element, and to area conservation. In the presence of reactions, however, the loss due to escape is counteracted by the production of new B particles, and as a result, the instantaneous average width of the bands becomes nonzero.

This local effect of the reaction can be described both in the concentration and in the individual particle modeling picture. Within the framework of the former, much insight can be gained into the reaction dynamics by analyzing the so-called Lagrangian filament slice model [136]. The idea is that, along the unstable manifold, the concentration c of material B is rapidly homogenized (due to the stretching feature of the chaotic flow), and after some time the concentration can be considered to be invariant under translation along the unstable direction. In the transversal direction, however, there is contraction, and as a consequence strong gradients build up. In a reference frame comoving with the fluid element, the effect of the fluid flow transversal to the unstable manifold is basically a contraction, due to the presence of the contracting Lyapunov exponent. Taking the x coordinate as the one measuring the distance from the unstable manifold, the typical flow field can be written as $-\bar{\lambda}x$ since in incompressible flows the contracting Lyapunov exponent coincides with the expanding one $\bar{\lambda}$ (in modulus). The Lagrangian filamental slice model is thus a reduced one-dimensional model of the form

$$\frac{\partial c}{\partial t} - \bar{\lambda}x\frac{\partial c}{\partial x} = kc(1-c) + D_{\mathrm{diff}}\frac{\partial^2}{\partial x^2}c \ , \tag{35}$$

where the reaction term is the same as (32), containing c, the relative concentration of B. By measuring time in units of $1/\bar{\lambda}$ and length in units of some linear scale L, the equation becomes

$$\frac{\partial c}{\partial t} - \frac{\partial c}{\partial x} = Dac(1-c) + \frac{1}{Pe}\frac{\partial^2}{\partial x^2}c \ , \tag{36}$$

where two dimensionless parameters remain. The first one is the Lagrangian Damköhler number

$$Da = \frac{k}{\bar{\lambda}}, \tag{37}$$

which is the ratio of the time scale of the chaotic advection ($1/\bar{\lambda}$, the Lyapunov time) to the time scale of the reaction. $Da \gg 1$ implies that the reaction is very fast on the time scale of advection, while for $Da \ll 1$, the reaction is much slower than advection. The other dimensionless quantity is the Lagrangian Péclet number

$$Pe = \frac{\bar{\lambda} L^2}{D_{\text{diff}}}\ , \tag{38}$$

which characterizes the relative strength of the advection and diffusion.

The corresponding Eulerian dimensionless quantities appearing in the diffusion–reaction equation (34) are the Damköhler [38] and Péclet [101] numbers, $Da' = kL/U$, and $Pe' = LU/D_{\text{diff}}$, respectively, where U denotes the characteristic velocity of the flow, and L is the characteristic length scale.

In what follows, we assume that the reaction is fast, and diffusion is very slow. While diffusion spreads the reactive material around the unstable manifold, the fast reaction immediately increases concentration c to its maximum, 'consuming' all available resources. This implies that the coverage of the filaments of the unstable manifold by the reactive material has sharp edges. This is a feature what one also finds when dealing with particles (there is either one or no particle at a given site). In other words, this limit of fast reaction and slow diffusion of (35) corresponds to the individual particle picture.[1] We then have a coverage of the filaments by stripes of some width $\delta(t)$, within which $c = 1$, while $c = 0$ outside. Inside the stripes reaction is stopped in lack of resources, they only occur at the edges. We can then write an *ordinary* differential equation for the width.

Consider now a single band of B-particles of width $\delta(t)$ lying along a segment of the unstable manifold. The bandwidth changes for two reasons. First, it decreases at a rate $-\lambda\delta$. This is due to the exponential stretching along the unstable manifold with a local Lyapunov exponent λ of the passive advection dynamics, which is accompanied, because of incompressibility, by a contraction of strength $-\lambda$. Second, due to the reaction, the bandwidth increases. This increase is proportional to the reaction velocity v (see Fig. 24).

The rate of increase of the bandwidth is $2v$, since the reaction front propagates on both sides of the band. Thus, the time derivative $\dot{\delta} \equiv \mathrm{d}\delta/\mathrm{d}t$ of the width is given by

$$\dot{\delta} = -\lambda\delta + 2v. \tag{39}$$

This simple differential equation expresses the competition of two effects: the exponential contraction of the bands towards the underlying fractal, and the linear expansion due to the front propagation of the autocatalytic process. After some transient time, comparable to $1/\lambda$, this competition leads to a *steady state* ($\dot{\delta} = 0$) characterized by the fixed point value

$$\delta^* = 2\frac{v}{\lambda}. \tag{40}$$

[1] In terms of the dimensionless number this implies $Da > 1$, $Pe \gg 1$, or Pe, $Da \to \infty$ with $Da/Pe \ll 1$ remaining finite.

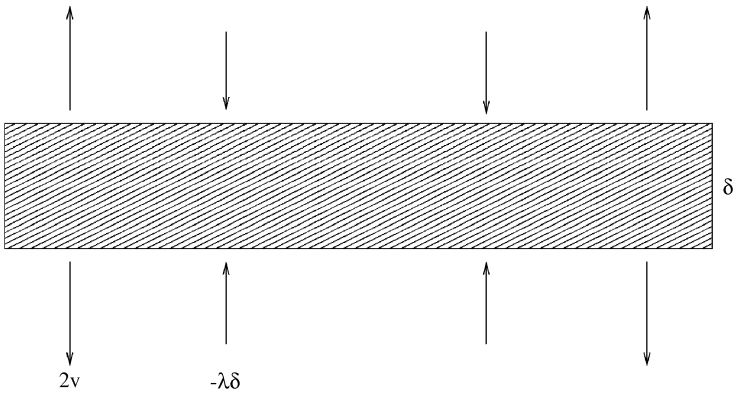

Fig. 24. Schematic diagram indicating the bandwidth dynamics: there is contraction across the unstable manifold due to the flow, and increase of the bandwidth due to reactivity.

We emphasize that this equation is a consequence of the Lagrangian filament slice model (35) whenever the continuum approach is applicable [143]. This approach, however, cannot be straightforwardly generalized to inertial particles. Therefore, it is the bandwidth equation (39) on which our entire presentation is based, which also allows an extension for three-dimensional flows and for flows with transport barriers.

The equation above describes an isolated band. In a chaotic flow, however, there are several bands coexisting, all with different local Lyapunov exponents. We can assume that the dynamics of each of these bands are similar to that of an isolated one, treated above. These bands have a typical (average) instantaneous width $\overline{\delta}$. For the sake of keeping the notation simple, from now on we denote the average bandwidth simply by δ, without the bar. No confusion should arise, because we will be mostly interested in average quantities in the following. The equation for the time evolution of a typical bandwidth is thus:

$$\dot{\delta} = -\overline{\lambda}\delta + 2v \ , \tag{41}$$

where $\overline{\lambda}$ is the average of the local Lyapunov exponents; hence, it is just what is usually called the Lyapunov exponent. The average steady-state width, *the reactive scale* is thus

$$\delta^* = 2\frac{v}{\overline{\lambda}} \ . \tag{42}$$

It is worth giving an estimate of the characteristic scales and, above all, of the reactive length scale δ^* (42) for the four flow regimes listed in the Introduction (cf. Table 2). The length scales L range from micrometers to thousands of kilometers, and even the characteristic velocities U span three orders of magnitudes. Typical Lyapunov exponents are reported to be 1/weeks [4] and 1/(5 days) [97] in the ocean and in the stratosphere, respectively. Note that they are of the order of U/L. The characteristic replication time of (phyto)plankton is 2 days, and we take this as the reaction time in the ocean. The depletion of ozone is a similarly slow process in the stratosphere, we therefore estimate the reaction rate to be about the same. We emphasize that in large-scale flows, the role of the molecular diffusion is taken over by turbulent diffusion, which is of much larger magnitude. The front velocity is estimated from Eq. (33) with $\alpha = 2$, and the resulting reactive scales range from 10 μm to tens of kilometers.

In Table 3, we also give the dimensionless numbers. In spite of the huge span in length scales, the Damköhler numbers are between 2 and 10. This indicates that reactivity and advection are of

Table 2
Characteristic parameters for some reactive flows on different scales

	Microfluids	Laboratory	Ocean	Atmosphere
L (m)	5×10^{-4}	1	10^5	10^6
U (m/s)	10^{-2}	10^{-2}	10^{-1}	10
$1/\overline{\lambda}$ (s)	5×10^{-2}	10^2	10^6	4×10^5
$1/k$ (s)	10^{-2}	10	2×10^5	2×10^5
D_{diff} (m^2/s)	10^{-9}	10^{-9}	1	10^2
v (m/s)	6×10^{-4}	2×10^{-5}	4×10^{-3}	4×10^{-2}
δ^* (m)	5×10^{-5}	4×10^{-3}	8×10^3	3×10^4

Table 3
Dimensionless numbers of the reactive flows of Table 2

	Microfluids	Laboratory	Ocean	Atmosphere
$Da = k/\overline{\lambda}$	5	10	5	2
$Da' = kL/U$	5	10	5	5×10^{-1}
$Pe = \overline{\lambda}L^2/D_{\text{diff}}$	5×10^3	10^7	10^7	3×10^4
$Pe' = UL/D_{\text{diff}}$	5×10^3	10^7	10^7	10^5

approximately equal importance in these phenomena, and the reactions are somewhat faster than advection. On the other hand, the Péclet numbers are all very large, showing that diffusion is negligible compared to hydrodynamical advective effects.

It is worth emphasizing that the basic feature leading to Eq. (40) is the existence of a front velocity. Therefore all reactions with a well-defined front (such as bistable or excitable reactions, and flames [143,144,89]) are expected to behave similarly in flows. We shall discuss this in some more detail in Section 10.

The bandwidth dynamics investigated so far reflects local properties, and is valid for both closed and open flows. The basic feature of open flows is that the unstable manifold is a fractal, not filing out the entire flow field. This implies that after a transient time, the B-material is distributed in bands of average width $\delta(t)$ and their total area is less then the fluid area in the region of observation. Furthermore, on any filamentary segment, infinitely many other segments accumulate, since they form a fractal set. The number of B bands *observed* to cover the segments with a width δ is finite due to the overlaps. The total B-distribution, covering the unstable manifold, appears thus to be a fractal on length scales above δ (or δ^* in the steady state), but it is smooth below this reactive scale.

4.3. The new rate equation

Let us consider a fixed region of linear size L that contains filamentary bands of average width $\delta(t)$ around the unstable manifold. According to fractal geometry [115,45], the number N of boxes of linear

size ε needed to cover a fractal set of dimension D is proportional to ε^{-D}:

$$N(\varepsilon) = \mathscr{H}\left(\frac{\varepsilon}{L}\right)^{-D} . \tag{43}$$

Here $\mathscr{H}$ is a dimensionless geometrical factor, the so-called Hausdorff volume.

The smallest box size where this scaling is observed is the typical width introduced above, $\varepsilon = \delta$. At this coverage, the number of boxes needed to cover the fractal filaments in the region of observation is $N(\delta) \sim \delta^{-D}$. The total area $\mathscr{A}_B$ covered by material B in the observation region is therefore $N(\delta)$ times the area δ^2 of a single box, or $\delta^2 N(\delta)$, which is

$$\mathscr{A}_B = \mathscr{H} L^2 \left(\frac{\delta}{L}\right)^{2-D} . \tag{44}$$

Note that the exponent $2-D$ in the above expression is the difference between the dimension of space and the dimension of the unstable manifold. Due to the frontal propagation of the reaction, the concentration along the bands is approximately constant (see Fig. 24). The *number B* of the B-particles in the given region of observation is thus proportional to the area

$$B = c_0 \mathscr{A}_B , \tag{45}$$

where c_0 is 1/(the area covered by a single particle) in the particle picture, and is the maximum concentration $c_0 = 1$ in the continuum model.

By taking into account the time dependence in (44), the time derivative of the total number of B particles, using Eq. (45), is

$$\dot{B} = c_0 \mathscr{H} L^D (2-D)\delta^{1-D}\dot{\delta} + B\dot{\mathscr{H}}/\mathscr{H} . \tag{46}$$

Note that the fractal dimension is time-independent, see Section 2.1. By using $2 - D = \kappa/\bar{\lambda}$ (see Eq. (6)), substituting $\dot{\delta}$ from (41), and assuming that $\dot{\mathscr{H}}/\mathscr{H}$ is negligible[2] we obtain

$$\dot{B} = -\kappa B + q\kappa \frac{v}{\bar{\lambda} L} B^{-\beta} , \tag{47}$$

where

$$q = 2(c_0 L^2 \mathscr{H})^{1/(2-D)} \tag{48}$$

is a dimensionless geometrical factor, and the exponent β is *constant*:

$$\beta \equiv \frac{D-1}{2-D}. \tag{49}$$

The first term on the right-hand side of Eq. (47) describes the exponential decay in the number of B particles due to outflow. The second term is the *production term*, that is, the rate of production of B due to the autocatalytic reaction. The exponent in the production term is *always* negative, since $1 < D < 2$ for chaotic 2D flows (β is positive). Eq. (49) implies that the smaller the number of B-particles is, the greater the production becomes, and that the productivity diverges as B approaches zero.

[2] Without this assumption, the prefactor $-\kappa$ of B in (46) must be replaced by $-\kappa + \dot{\mathscr{H}}/\mathscr{H}$. Due to the periodicity of the flow, $\mathscr{H}$ is also periodic, and the time average of this prefactor is $-\kappa$.

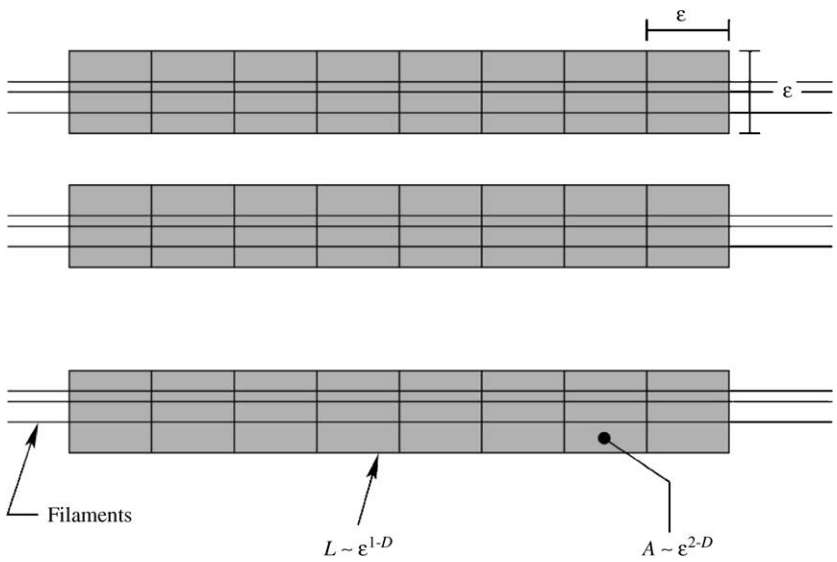

Fig. 25. Schematic diagram illustrating the ε-dependence of the perimeter length $\mathscr{L}$ and the area $\mathscr{A}$ of a filamentary fractal, when observed with resolution ε.

We shall see in Sections 10.2 and 10.3 that Eq. (47) is valid for other types of reactions, too. For a broad range of reactions (see Section 10) in 2D open flows the rate equation is of somewhat different form, but all of them have the property that the production term contains the particle number raised to the power β given by Eq. (49). It is important to emphasize that the exponent β characterizes the geometry of the reaction-free chaotic advection, being determined solely by the dimension of the unstable manifold of the chaotic saddle.

The appearance of this negative exponent in widely different active processes is a generic property of filamentary fractals: the perimeter length of their finite-width coverage *increases* as the area of the coverage decreases. This is the relationship which leads to the singularly enhanced productivity. In order to understand this, let us derive the relationship between the observed perimeter length $\mathscr{L}$ and the area $\mathscr{A}$ of filamentary fractals. Since to cover such a fractal set requires $N(\varepsilon) \sim \varepsilon^{-D}$ small squares of linear size ε, and since two of the four edges of each box typically belong to the perimeter of the covered area, the perimeter length is proportional to ε^{1-D} and *increases* with refining resolution (remember $2 > D > 1$) (see Fig. 25). On the other hand, the area is proportional to ε^{2-D} and *decreases* with refining resolution. By eliminating ε from the relations $\mathscr{L} \sim \varepsilon^{1-D}$ and $\mathscr{A} \sim \varepsilon^{2-D}$, we find that

$$\mathscr{L} \sim \mathscr{A}^{-\beta} \tag{50}$$

with β as given by (49). Thus, the perimeter length is, at any small resolution, a *negative* power $(-\beta)$ of the area. In view of this, the production term in (47) can be interpreted as an expression for the reaction taking place along the perimeter of a fattened-up filamentary fractal seen at resolution δ. This is a purely geometric phenomenon, and hence the feature of singular enhancement of productivity can be expected to be present whenever the reaction takes place around a fractal set.

The singular productivity disappears for $D = 1$, representing a flow in which the filaments do not form a fractal, and advection is consequently non-chaotic. In this case, $\beta = 0$, $D = 1$, $\kappa = \overline{\lambda}$, and the rate equation

(47) reduces to

$$\dot{B} = -\kappa B + P \ , \tag{51}$$

where $P \sim vc_0L$ is a constant productivity. This is the traditional equation for a surface reaction in the presence of outflow.

Another limiting case is that of $D = 2$, which occurs in closed flows, where the unstable manifold is space filling (cf. Section 11). In this case, the escape rate is $\kappa = 0$, since there is no outflow. The rate equation (47) then reduces to $\dot{B} = 0$, and there is no production after the steady state has set in. It is possible, however, to investigate the transient behavior leading to this trivial steady state, see Section 11.

Eq. (47) describes the competition of two effects: outflow and production. As a result of the balance between these effects, a *steady state* sets in after sufficiently long time for the global distribution in the region of observation. This steady state is synchronized with the flow, i.e., it takes over the time-dependence of the flow and in general follows the hydrodynamical time-dependence manifested in the parameter q (see Eq. (48)). In other words, the shape of the filaments follows the shape of the unstable manifold determined by the advective dynamics, at all times. In the case when the time dependence of parameter q is weak (is practically time-independent), the steady-state value of the number of particles is given by

$$B^* = \left(\frac{qv}{\bar{\lambda}L}\right)^{2-D} \sim \delta^{*2-D} \ . \tag{52}$$

The scaling is unique: B^* is proportional to the power $(2 - D) < 1$ of the reaction velocity. For example, if $v \sim 10^{-4}$ m/s, the value of B^* is with $D = 1.5$ two orders of magnitude larger than that for a traditional active process with $D = 1$.

4.4. Consequences and new features of the rate equation

4.4.1. Advantage of rarity

The singular production term in the rate equation, Eq. (47), corresponds to the principle of *advantage of rarity*. If reagent B represents living organisms, a state with a smaller number of organisms will grow, in view of the term $B^{-\beta}$, much faster than another one with more individuals. This is due to the fact that a smaller population covers the unstable manifold with a smaller area but with a longer perimeter. It thus grows faster. One consequence of the advantage of rarity principle is the existence of a nontrivial steady state: the population cannot die out, according to this model (but see Sections 4.4.6 and 12), and plays an important role in understanding the coexistence of competitive populations (see Section 5). Another consequence is that the number of individuals, Eq. (52), in the steady state is proportional to a power smaller than unity of the velocity, and it is thus much *larger* for small velocities (rare populations) than that expected from a linear law, characteristic of traditional population dynamics models.

4.4.2. Dimensionless forms

By measuring the time in units of $1/\kappa$, we obtain the dimensionless rate equation

$$\dot{B} = -B + qVB^{-\beta} \ , \tag{53}$$

where q is defined by Eq. (48), and

$$V = \frac{v}{\bar{\lambda} L} \tag{54}$$

is a dimensionless reaction velocity. Note that it contains the Lyapunov exponent of the passive advection, and hence it is a Lagrangian number (which cannot be obtained from a traditional, Eulerian approach).

In view of relation (33), the dimensionless front velocity can be expressed in terms of the Lagrangian Damköhler (37) and Péclet (38) numbers:

$$V = \alpha \left(\frac{Da}{Pe} \right)^{1/2} , \tag{55}$$

and is always small in view of the large magnitude of the latter. The steady-state particle number from Eq. (52) is then

$$B^* = (qV)^{2-D} = \left(q^2 \alpha^2 \frac{Da}{Pe} \right)^{1-D/2} . \tag{56}$$

It is worth noting that although the Eulerian dimensionless numbers (Da' and Pe') are close to Da and Pe in their values, in the dimensionless equation (53) only the latter occur (via V). This clearly indicates that the phenomenon is of Lagrangian character.

4.4.3. Product vs. diffusivity

Because in the continuum model the reaction front velocity v is proportional to the square root of the diffusion coefficient D_{diff} (see Eq. (33)), we obtain from (52)

$$B^* \sim D_{\text{diff}}^{(2-D)/2} . \tag{57}$$

The amount of particles produced is proportional to the fractional power $(1 - D/2)$ of the diffusion coefficient. This relation for diffusive particles has also been derived in Refs. [202,223].

4.4.4. Dependence of production on resolution

Let us now consider the production term $P(B) = qVB^{-\beta}$ of Eq. (53) in the steady state. Assume that this production is measured with a resolution ε *worse* than the reactive scale, i.e, $\varepsilon > \delta^*$. Since the production is proportional to the perimeter length seen with the resolution used, we have

$$P(\varepsilon) \sim \varepsilon^{1-D} . \tag{58}$$

The exact amount of production $P(\delta^*)$ is, however, proportional to δ^{*1-D}. The ratio of the observed, coarse-grained amount of production to the exact one is thus

$$\frac{P(\varepsilon)}{P(\delta^*)} = \left(\frac{\delta^*}{\varepsilon} \right)^{D-1} , \quad \varepsilon > \delta^* . \tag{59}$$

By improving the resolution (decreasing ε towards δ^*) the ratio moves towards unity (see Fig. 26).

This dependence is not present at all in the nonchaotic case, where $D = 1$. Therefore, we conclude that the increase of productivity with increasing resolution observed earlier in simulations of environmental problems [41,113] can be described by Eq. (59), that is, by the fractality of the reacting substance

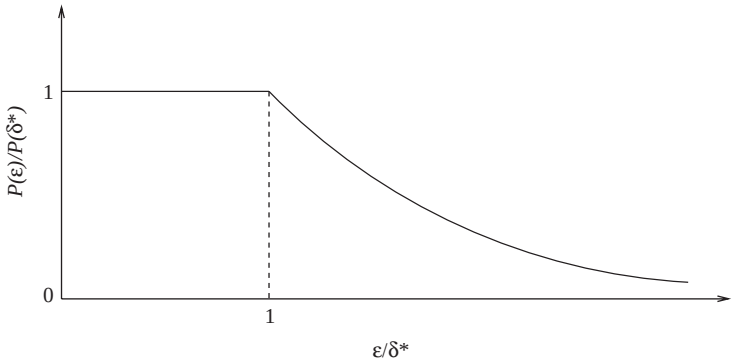

Fig. 26. Schematic diagram of the dependence of the production term on the resolution. For $\varepsilon < \delta^*$, $P(\varepsilon)$ coincides with $P(\delta^*)$.

distribution. Our results show that this effect is present even if the description of the hydrodynamical flow field is complete, in contrast to a similar effect reported before [41,113], which may be due to incomplete knowledge of the flow field.

4.4.5. Enhancement factor

In a non-chaotic flow (with $D = 1$, a non-fractal distribution), the average width δ^* of B-particle bands in the steady state is proportional to $v/\bar{\lambda}$. The enhancement factor relative to the non-chaotic case is thus

$$\frac{B^*(D)}{B^*(D=1)} \sim \left(\frac{v}{\bar{\lambda}L}\right)^{1-D} \sim V^{1-D}\ , \tag{60}$$

where V is the dimensionless front velocity given by Eq. (55). Since $\delta^* = 2v/\bar{\lambda}$ is typically much smaller than the characteristic length scale L of the flow, $V \ll 1$, and the right-hand side is typically a very large number (recall that $1 - D < 0$ for 2D flows). Consequently, there is always a considerable enhancement due to the chaoticity of the advection dynamics. Eq. (60) can also be considered as a quantitative measure of the efficiency of the advantage of rarity, described in Section 4.4.1.

4.4.6. Emptying transition

According to numerical simulations with the continuum model, the total amount of B particles depends in a nontrivial way on the reaction velocity.[3] It is observed [143] that below a critical Damköhler number Da_c, no product remains in the flow. Thus, an 'emptying transition' takes place at this critical value of Da. Fig. 27 shows schematically the dependence of the steady-state particle number on the Damköhler number. Around the critical point the particle number goes continuously to zero [143]. In other words, the transition is the analog of a second-order phase transition. It is interesting to mention that an analogous transition can be found by analytic means [143,144,70] in the Lagrangian filamental slice model (35), which proves thus to be a useful indicator of the global behavior in the continuum picture.

In the discrete time version of the particle picture, a similar emptying transition exists (cf. Section 12).

[3] For sufficiently slow reactions, the coefficient q in Eq. (48) becomes a function of the reaction rate, too, or more precisely, of the Damköhler number Da (37).

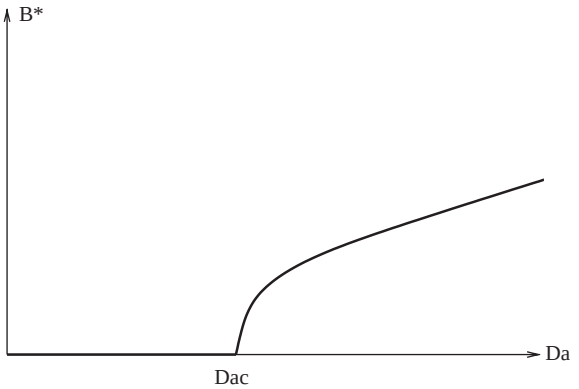

Fig. 27. Schematic diagram showing the dependence of B^* on the reaction velocity expressed in terms of the Damköhler number Da. The critical Damköhler number Da_c turns out to be of order unity.

4.4.7. Interpretation in terms of flames

As mentioned earlier in Section 3, the autocatalytic reaction, described in terms of the FKPP equation (32), can be considered as a model of combustion. Since $c = 1$ corresponds to burned material, the flame is located in regions of high-concentration gradients. The theory above shows that, in cases when there is a supply of unburned material advected by open flows, the well-known front propagation feature of the FKPP equation, together with the contraction induced by the flow, leads to filamentary structures on which the flame is concentrated. This pattern is steady within the region of observation, and can be generated by a localized initial perturbation (a 'spark'). Outside the filaments no burning takes place. A measure of the efficiency of burning is given by the particle number B^*, which is proportional to the area over which the flame spreads. In closed flows, where the material leaving a certain region is fed back within a short period of time, the asymptotic steady state is $c = 1$ throughout the container. The burning of all the fluid is, however, not necessarily advantageous in a practical problem. The results of this section suggest that *controlled, moderate* burning can best be realized in *open flows*. In the case of everyday heaters, the open character of the flow is due to the effect of buoyancy, which makes the hot gases rise up in the air, thereby leaving the active region around the heater. Eqs. (47) and (49) then suggest that burning in chaotic open flows is more efficient than in nonchaotic ones (cf. (60)).

4.4.8. On the diffusive scale δ_{diff}

It is widely known that diffusion sets a characteristic length scale in reaction-free problems, and this is often taken as $\sqrt{D_{\mathrm{diff}}/S}$ with S as a characteristic strain rate of the flow [62,223]. We point out that in chaotic advection the diffusive scale should be determined with the average Lyapunov exponent (instead of the Eulerian strain). Next, we show that the characteristic bandwidth δ^* of reactive flows is typically exceeding the diffusive scale.

In a reaction-free problem the width δ of a band filled with particles is increasing in time proportionally to $\sqrt{t}$ due to diffusion. In a medium at rest no counter-action is present, and the bandwidth dynamics can be described by the differential equation

$$\dot{\delta} = \frac{D_{\mathrm{diff}}}{\delta} \tag{61}$$

whose solution with initial condition $\delta(0) = \delta_0$ is $\delta(t) = \sqrt{\delta_0^2 + 2D_{\mathrm{diff}}t}$.

In the presence of a permanent contraction due to the chaoticity of the flow, the term $\bar{\lambda}\delta$ should be added. The equation of a typical band then reads as

$$\dot{\delta} = \frac{D_{\text{diff}}}{\delta} - \bar{\lambda}\delta \ . \tag{62}$$

At steady state, contraction balances diffusive spreading, such that

$$\delta^*_{\text{diff}} = \sqrt{\frac{D_{\text{diff}}}{\bar{\lambda}}} \ . \tag{63}$$

This is the diffusive scale corresponding to the reaction-free case in a chaotic flow.

Using (40) and (33), the reactive scale δ^* can be expressed as

$$\delta^* = 2\alpha\sqrt{Da}\,\delta^*_{\text{diff}} \ . \tag{64}$$

The reactive scale is thus larger than the diffusive one whenever Da is larger than $1/(2\alpha)$, i.e., of order unity, which is so in all cases of Table 3. A more important difference is that, in the lack of permanent particle influx, the particle concentration above the diffusive scale is *decaying in time* in a reaction free case, while the particle concentration is *constant* in the reactive case.

We mention that the presence of an additional spreading due to a front velocity can also be incorporated [205] by the form

$$\dot{\delta} = \frac{D_{\text{diff}}}{\delta} - \bar{\lambda}\delta + 2v \ . \tag{65}$$

In dimensionless units ($\delta/L \to \delta$, $t\bar{\lambda} \to t$), this can be rewritten as

$$\dot{\delta} = Pe^{-1}\frac{1}{\delta} - \delta + 2V \ . \tag{66}$$

For large Péclet numbers ($Pe \to \infty$) the first term is negligible compared to the others (V decreases with the square root of Pe only, cf. (38)). This shows that the relevant bandwidth equation is indeed Eq. (39) for our cases of interest (cf. Table 3), characterized by large Péclet numbers: the presence of a front velocity is the dominant effect.

4.4.9. Autocatalytic reaction with continuous inflow of material

Finally, we study how a constant inflow of reactive, autocatalytic material modifies the reaction (47). Such a continuous inflow of one of the materials is inescapable to maintain a steady state in the case of non-autocatalytic processes, as will be discussed in Section 10.4. The injection implies that without any flow and reaction, the rate equation would be $\dot{B} = \Phi_B = \text{const}$, where Φ_B denotes the given injection rate (number of injected particles per unit time). This globally constant inflow rate has, however, to be divided among the filaments of the unstable manifold. This means that the amount of injection that goes into each B-band around the filaments, out of the total injection rate Φ_B, must depend on the actual number of bands, and hence on the average bandwidth δ. This modifies Eq. (41), the bandwidth dynamics, to

$$\dot{\delta} = -\bar{\lambda}\delta + 2v + q_0(\delta) \ , \tag{67}$$

where $q_0(\delta)$ is the share of a typical band from the injection. The novel feature of the continuous inflow problem is the appearance of the term $q_0(\delta)$ whose actual form can only be deduced from the global behavior.

The time derivative of (45), using Eqs. (44) and (67), leads now to

$$\dot{B} = -\kappa B + (c_0 L^D \mathscr{H})^{1/(2-D)}(2-D)[2v + q_0(\delta)]B^{-\beta} \ , \tag{68}$$

where $\beta \equiv (D-1)/(2-D)$ (see (49)) is the same as in the case of no injection. We can fix the value of $q_0(\delta)$ from the fact that in a reaction-free case ($v = 0$) $\dot{B} = -\kappa B + \Phi_B$ has to apply. This leads to $q_0(\delta) = \Phi_B (c_0 L^D \mathscr{H})^{-1/(2-D)}(2-D)^{-1} B^{\beta}$. Using this and (6), and introducing the geometrical factor q as in (48), we end up with

$$\dot{B} = \Phi_B - \kappa B + q\kappa \frac{v}{L\bar{\lambda}} B^{-\beta} \ . \tag{69}$$

Comparing this expression with Eq. (47), we see that a new term, the injection rate Φ_B appears in the rate equation.

5. Coexistence of biological competitors

In this section, we apply the theory developed above to the study of species coexistence in chaotic open flows. This approach sheds some new light on one of the classical problems of ecology, the famous 'paradox of plankton' [179,84,181].

5.1. Competitive exclusion

The problem of coexistence of competing species is a classical question of theoretical ecology. It is of central importance in several ecological problems, ranging from the paradox of plankton [179,84,181] to prebiotic evolution [84,180]. Traditional theoretical and empirical investigations show that the number of coexisting species in a given ecosystem is limited by the number of *limiting factors*, that is, by the number of different resources for which the species are competing. In a well-mixed environment, only those species are able to survive which are best adapted to the use of at least one of the limiting resources [51,61,43]. This result is based on the hypothesis that the competing species are homogeneously mixed in their habitat, which was *assumed* to be the case for aquatic media. Competitive exclusion, however, contradicts the observation that a large number of species do coexist in a single ecosystem, while competing for the same limiting resources (e.g., nitrogen, carbon, phosphorus, etc.) whose number is observed in almost all situations to be never greater than about 10.

The traditional population dynamical equations for the numbers B_1, B_2 of two species B_1, B_2, respectively, competing for the same resource A, in a given well-stirred region, are:

$$\frac{\mathrm{d}B_1}{\mathrm{d}t} = \alpha_1 B_1 - \mu_1 B_1 \ , \tag{70}$$

$$\frac{\mathrm{d}B_2}{\mathrm{d}t} = \alpha_2 B_2 - \mu_2 B_2 \ . \tag{71}$$

The growth and death rates α_1, α_2 and μ_1, μ_2 depend on the number A of resource molecules A available, which changes in time as

$$\frac{\mathrm{d}A}{\mathrm{d}t} = \Phi_A - \alpha_1 B_1 - \alpha_2 B_2 \ , \tag{72}$$

where Φ_A is the rate at which the resource is injected into the region of observation. Regardless of the particular forms of the A-dependences, *no* fixed points can exist in the system in which both species would be in a steady state with non-zero values of $B_i = B_i^*$ [59].

5.2. Paradox of plankton

The contradiction of competitive exclusion with experience, as was first emphasized in Ref. [74], is common in phytoplankton communities, and is called the *paradox of plankton*. Here a number of species coexist in a relatively isotropic or unstructured environment, all competing for the same sorts of materials, and the number of species exceeds considerably the number of limiting factors. To explain this, Hutchinson [74] put forward the idea that seasonal environmental changes prevent competitive exclusion in natural phytoplankton communities. Thus the species of the community, at least on the time scale of ecological observation, are in non-equilibrium coexistence.

Since then numerous investigations revealed many different mechanisms, including spatial and temporal heterogeneity of habitat, predation, disturbance, co-evolution, etc. [220,32], increasing the chance for competitive coexistence. Naturally, under the word 'competition' many different biological phenomena are collected together, which influence the coexistence of species in different ways.

Thus, the original problem changed into finding the most relevant mechanisms which maintain diversity in particular situations [36,73,220,207,14]. Despite the vivid debate in this field of ecology, there appear to be two main lines of consensus. According to one, climatic periodicities and fluctuations play the main role in causing species' persistence in phytoplankton communities [50,166,193]. The other view is that external disturbances [36] are the most adequate hypothesis for the explanation of high diversity in phytoplankton communities, see e.g. Ref. [167]. These suggested explanations of the paradox of plankton assume that the external environmental disturbances are inhomogeneous in space and/or time. These disturbances would keep the species in coexistence by having compact patches of different non-equilibrium states.

In the previous sections, however, we have seen that there is no need to assume external causes to explain the inhomogeneous distribution of species advected by fluid flows. We have seen that even without external disturbances, the aquatic environment is expected to be neither well-mixed nor homogeneous. As we have shown, advected substances accumulate along filamentary fractals, which have a major effect on their active processes. In particular, due to the underlying hydrodynamical advection, active processes feature the property of advantage of rarity (Section 4.4.1). This provides a mechanism which favors the survival of the species that are about to go extinct.

Coexistence hence might be possible in *imperfectly stirred environments*. This mechanism for coexistence is further supported by numerous remote sensing images, which show that phytoplankton are typically distributed along fractal-like filaments in the oceans. (cf. Fig. 4 and [15]).

5.3. Numerical simulations

Numerical [84,179,86] and theoretical [181] investigations proved that the coexistence of competing species is indeed possible in inhomogeneously mixed, open aquatic environments.

The simplest case is provided by advected autocatalytic species in an open flow. Their competition is for the common resource A, which means that their activity is described by $B_1 + A \to 2B_1$, $B_2 + A \to 2B_2$. *Without any flow*, the stronger species with faster reproduction would sooner or later encircle the slowly growing patch of the inferior one, preventing its access to the resources. In a *perfectly mixed* environment,

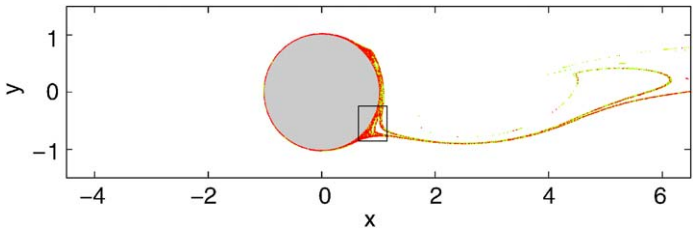

Fig. 28. (Color online.) Coexistence of two species in the von Kármán vortex street flow behind a cylinder. The figure shows a snapshot of the population distribution after steady state has been reached. The two species are green (B_1) and red (B_2).

ordinary differential equations in terms of the average concentrations (similar to Eqs. (70) and (71)), would describe the process by which the inferior species would decay rapidly to extinction.

When the competing autocatalytic species are advected by an *open chaotic* fluid flow, they accumulate on fractal filaments of large perimeter, allowing the inferior species to also have access to the resources. Moreover, the advantage of rarity principle generated by the advection (discussed in Section 4.4.1) favors the species which is less abundant. The less abundant a species is, the more enhanced its activity (in this case, its reproduction rate) becomes.

This expectation was verified in numerical simulations where resource A exists in abundance, as in the case of the simple autocatalytic process of Section 4. The competitors B_1 and B_2, utilizing this resource, are placed in the flow in small patches in front of the mixing region. They enter then into the region where the flow is time-dependent, and are pulled into filaments of fractal structure. The number of competitors of each species rapidly reaches an equilibrium value. In this steady state, the competitors are in coexistence in a significant region of the parameter space, even when one of the competitors is much fitter than the other one.

The numerical simulations were carried out for the von Kármán vortex street behind a cylinder. The coexistence of the species is illustrated in Fig. 28. A small region of that figure is magnified in Fig. 29. It is clear that the species coexist along the filaments of the unstable manifold, and they are washed away everywhere else due to the outflow from the mixing region. The coexistence is further illustrated by the plot of the total population of both species as a function of time, shown in Fig. 30.

Generalizing the theory of Section 4, a set of equations can be obtained that describes the population dynamics of competitive autocatalytic replicators in an open flow, as will be shown in Section 10.3.

5.4. Metabolic models

In many cases, the simple autocatalytic model is not sufficiently realistic to describe real competitive systems. One example is the cyclic competition of species: some bacteria [168] or phytoplankton species [222,178] might produce toxins that inhibit or kill other individuals around them. However, besides these killer and sensitive types, there might exist resistant types that, at the cost of slower replication, can resist the toxin. This way a cyclic competition occurs: killer out-competes the sensitive type, sensitive out-competes the resistant with slower reproduction, and resistant reproduces faster than the killer type. It has been shown that in a well-mixed environment coexistence is impossible [88], but in case of imperfect mixing generated by fluid dynamics, the coexistence is possible also in the case of the cyclic competition [82].

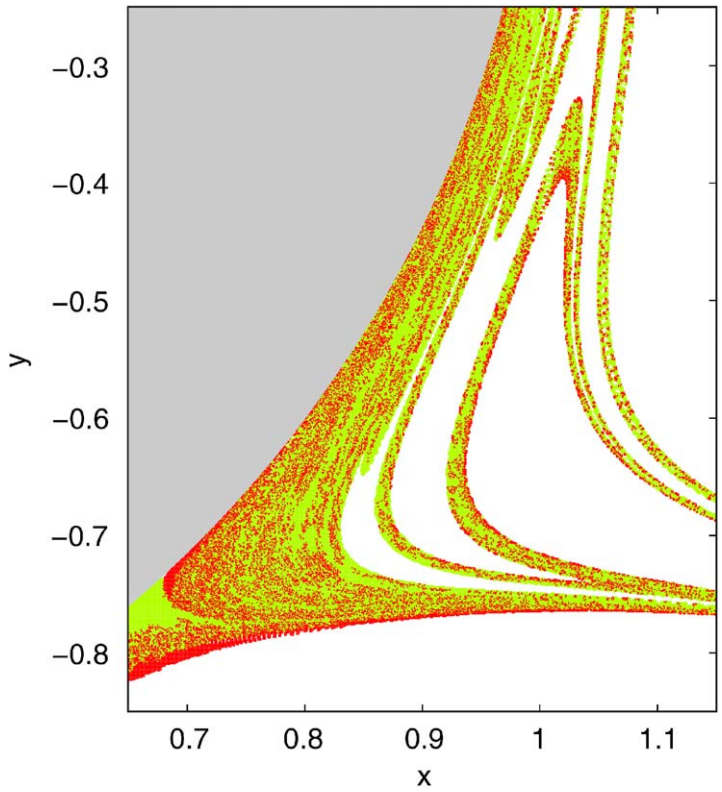

Fig. 29. (Color online.) Magnification of the rectangular box indicated in Fig. 28.

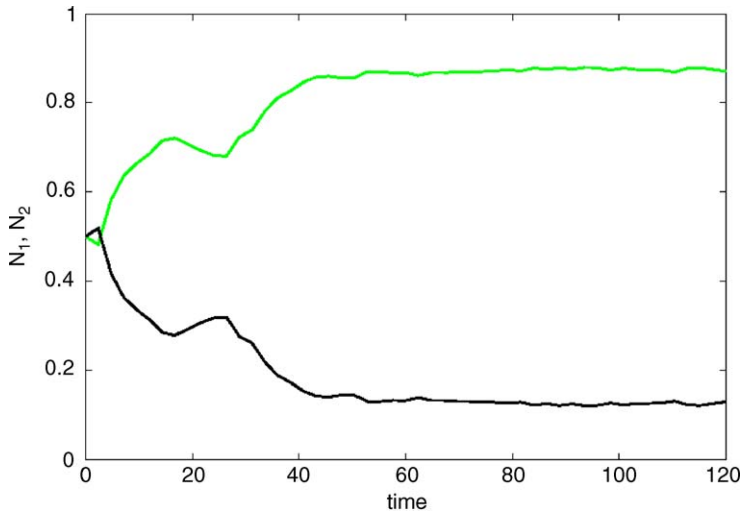

Fig. 30. (Color online.) Plot of the total population numbers (N_1 for B_1 and N_2 for B_2) in the frame of Fig. 28 as a function of time.

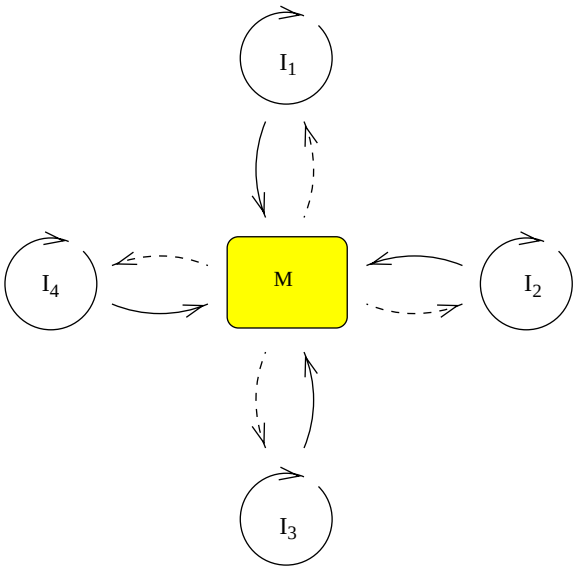

Fig. 31. Scheme of metabolic activity. All competitors I_i contribute to the common metabolism M, which in turn, provides help for reproduction of each species. It is assumed that all species are necessary to keep up the metabolism.

Another example, where an autocatalytic model is not appropriate, emerges when one tries to explain coexistence of self-replicating macromolecules during prebiotic evolution. In this case, a chemically more realistic metabolic model has been suggested [37], where replicating macromolecules cooperate via a common metabolism. In this chemically more realistic metabolic system, replicators help catalytically a common metabolism which in turn supplies energy-rich monomers for replication, as shown schematically in Fig. 31. It is assumed that all the replicators are necessary to drive the metabolic machinery, which means that the replicators act as 'obligate mutualists' in ecological terms. In other words, reproduction is possible if a competitor is supported by the common metabolism, that is, if it has in its small neighborhood *all* other competitors present. Naturally, when one competitor dies out, it drives the whole system to extinction, as no more reproduction is possible any longer. Since the metabolism provides a non-specific help to replication, in the perfectly mixed version of this model the fastest replicator excludes all the others, and the metabolic system collapses. Again, it turns out that the presence of a chaotic flow changes this picture dramatically [86].

We superimposed on this activity the advection, using the blinking vortex–sink flow discussed in Section 2.2.2. The initial patches of the competitors are quite far from each other, as shown in Fig. 32a, so that reproduction is impossible initially, because the metabolic help is unavailable for them. As time goes on, however, all species accumulate on the same fractal filaments, where they get close enough to each other, to start reproduction as they enter in each others' metabolic range. As illustrated in Fig. 32, they can coexist in spite of the permanent outflow for arbitrarily long time, concentrated on the filaments of the chaotic saddle's unstable manifold.

It was also possible to show [86] that the coexistence is robust against the appearance of parasitic species in a region of the parameter space. These parasites are species that do not contribute to the common metabolic pool; they just use it for reproduction, decreasing in this way the amount of available resources for the other competitors.

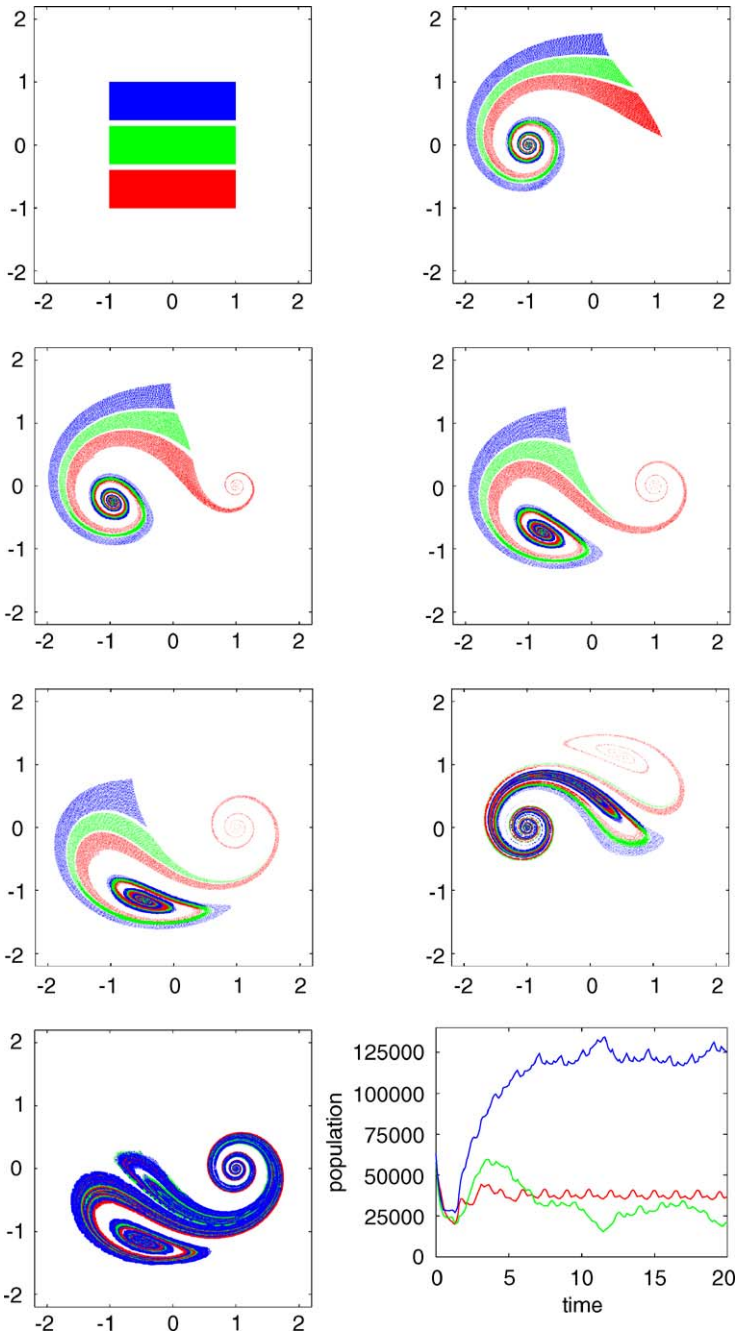

Fig. 32. (Color online.) Coexistence of metabolic network in the blinking vortex–sink system. Three species (blue, green, red) trace out the unstable manifold after some time, and then their population reaches a slightly fluctuating steady state. The snapshots were taken at (a) $t = 0$, (b) $t = 0.5T$, (c) $t = 0.6T$, (d) $t = 0.8T$, (e) $t = T$, (f) $t = 1.5T$, and (g) $t = 10T$. The last figure shows the time dependence of the three populations.

6. Autocatalytic reactions in 3D open flows

All our previous discussions have focused on two-dimensional fluids, because of the simplification this hypothesis entails. However, real fluids are three-dimensional, and many flows cannot be reasonably approximated by two-dimensional models. In this section, we undertake the study of activity in open 3D flows, for the case of hyperbolic advective dynamics, and show that in the jump from 2 to 3 dimensions, fundamentally new phenomena appear [131].

6.1. Advection

We first study the purely advective dynamics of a 3D flow, without considering activity. To simplify the analysis of new dynamical features found in 3D flows, we keep assuming the flow to be periodic in time. In this case, the stroboscopic dynamics can be reduced to a 3D volume-preserving map [47] where escape is possible. Because of its odd dimensionality, the number of unstable directions of the dynamics is different from the number of stable ones: such maps are not Hamiltonian, even though they preserve the 3-dimensional volume. This is in contrast to the 2D case, whose map is Hamiltonian (cf. Section 2). Since volume is preserved, there are two non-degenerate cases of hyperbolic advection dynamics in 3D flows:

- 'Type I': with one unstable and two stable directions, and
- 'Type II': with two unstable and one stable directions.

We will see that these two types of advection dynamics lead to distinct types of rate equations of the reaction dynamics.

We model the advection in a time-periodic 3D flow through a simple 3D map, which is a 3D generalization of the open baker map [204]. In spite of their simplicity, baker maps are known to reflect all generic features of hyperbolic dynamics [152]. The model is defined on a *xyz* cube of linear size L, and its action is shown in Fig. 33a. We denote the map by M. One iteration of M consists of two actions. First, the x and y directions are contracted by a factor Λ, with $\Lambda < \frac{1}{2}$, while the z direction undergoes an expansion by a factor $1/\Lambda^2$, thereby conserving volume. By this transformation, the cube turns into a long thin rectangular slab with its long edge along the z-axis, as shown in Fig. 33a. Second, four pieces with height L of this slab are selected and put in the four corners of the cube. The pieces of the slab that are not selected are discarded, and considered to have escaped (see Fig. 33a). Note that this map is a particular case of the more general situation in which there are two distinct contraction factors Λ_x and Λ_y, to be dealt with in Section 6.3.

The map M has two contracting directions, and one expanding direction, and is therefore of type I. We observe that for the inverse map M^{-1}, stable directions turn into unstable ones, and vice versa. Therefore, M^{-1} has one stable and two unstable directions, and is of Type II. We thus conveniently handle the two generic types of hyperbolic 3D maps with one single map, and its inverse. We note that, since hyperbolic systems are structurally stable, we are not loosing any generality by assuming a particular form for M.

Because the contracting and expanding directions of M (and also M^{-1}) are aligned with the x-, y- and z-axis, it is not difficult to visualize the stable and unstable manifolds: the stable manifold of M is a Cantor set of planes parallel to the horizontal, (x, y) plane, and the unstable manifold is a Cantor set of vertical segments. We can visualize these manifolds by iterating M forward a given number of times

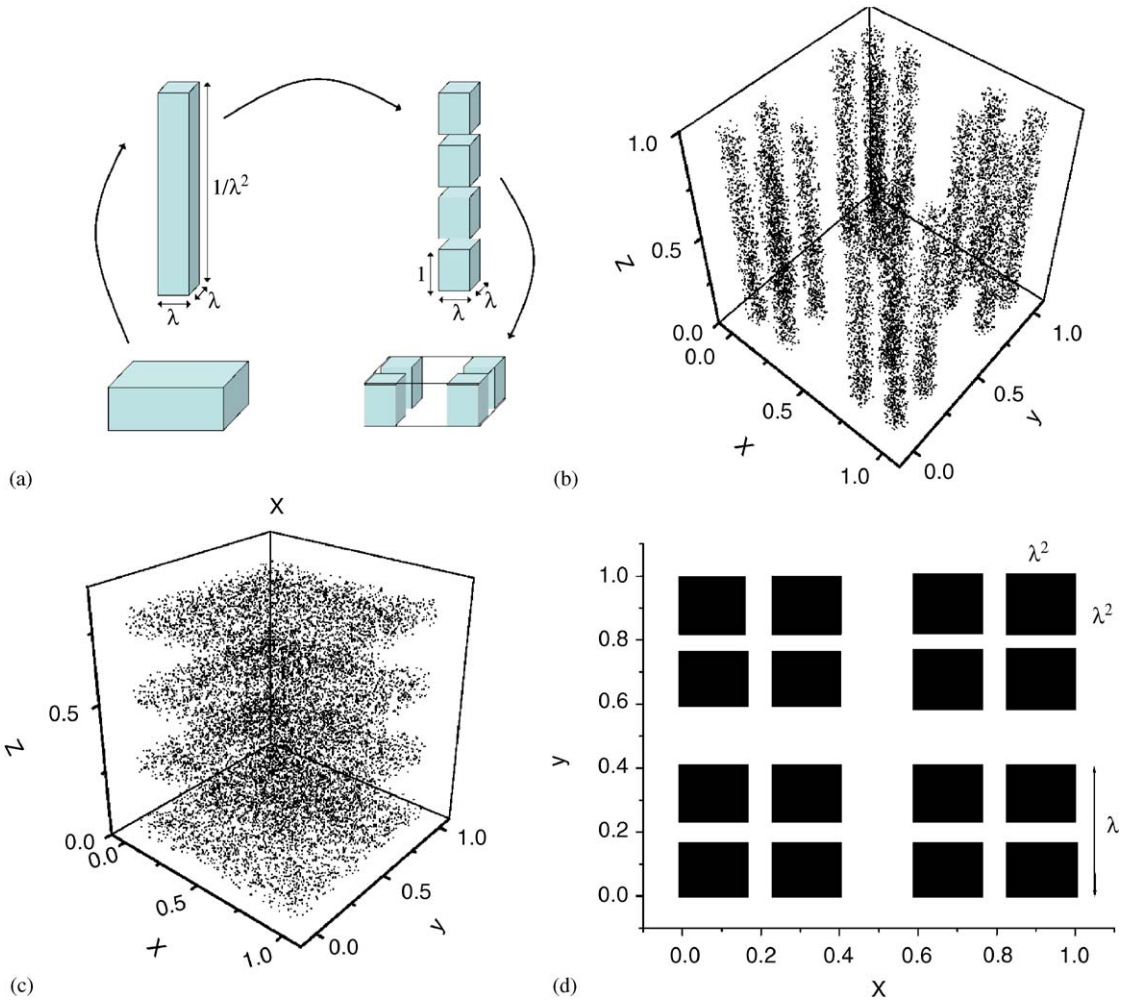

Fig. 33. (a) Illustration of the action of one iteration of map M on a cube of side $L = 1$ (Type I dynamics). The drawing is not to scale. (b) Surviving points after 2 iterations of the map M, for $\Lambda = 0.35$, with initial conditions chosen randomly in the cube. (c) The same as (a), but for the inverse map M^{-1} (Type II dynamics). (d) Intersection with a horizontal plane ($z = \text{const.}$) of the set of surviving points after 2 iterations of M, with $\Lambda = 0.35$.

for many initial conditions chosen randomly within the unit cube. The distribution of points that have not escaped approximate the unstable manifold of M, which is the stable manifold of M^{-1}. Conversely, iterating backwards (or iterating M^{-1} forward) gives a picture of the stable manifold of M (which is the unstable manifold of M^{-1}). The results are shown in Figs. 33b and c.

Let us consider now the unstable manifold of M, depicted in Fig. 33b. Since it is made up of vertical line segments, and since the expansion and contraction rates are uniform, we can restrict ourselves to the intersection of the unstable manifold with a horizontal plane. This is depicted in Fig. 33d, where the intersection of the set of surviving points of two iterations of M with a horizontal plane are shown. In the limit of an infinite number of iterations, a well-known double Cantor set in the plane is formed

[45,115], with fractal dimension given by $-2\ln 2/\ln \Lambda$. The unstable manifold is the product of this set and a one-dimensional line segment, with dimension

$$D_{\mathrm{u}} = 1 - 2\ln 2/\ln \Lambda \ . \tag{73}$$

Note that D_{u} is also the dimension of the *stable* manifold of M^{-1}. A similar reasoning can be applied to the stable manifold: it is the product of a Cantor set with a plane. We thus find

$$D_{\mathrm{s}} = 2 - \ln 2/\ln \Lambda \ . \tag{74}$$

The chaotic saddle is the intersection of the stable and unstable manifolds, and its dimension is $D_{\mathrm{saddle}} = -3\ln 2/\ln \Lambda$. From Eqs. (73) and (74), we see that $D_{\mathrm{u}} \neq D_{\mathrm{s}}$. Furthermore, D_{s} and D_{u} satisfy

$$1 < D_{\mathrm{u}} < 3, \quad 2 < D_{\mathrm{s}} < 3 \ . \tag{75}$$

Note that the structure of the stable and unstable manifolds for the two types of flow for a generic map (and not only for map M) is topologically similar to that shown in Fig. 33. Namely, for Type I flows, stable manifolds are a Cantor set of surfaces, and the unstable manifolds are a Cantor set of one-dimensional curves (and conversely for Type II flows). Also, inequalities (75) hold in general.

We observe from Eq. (75) that in Type II flows the dimension D_{s} of the stable manifold (which fulfills the same inequality as D_{u} in Eq. (75)) may be less than 2. In this case, the stable manifold has generically a null intersection with a one-dimensional curve, and thus the 1D scattering function (such as the escape time) is smooth, even though there is a fractal invariant set. For $D_{\mathrm{s}} > 2$, on the other hand, the typical scattering function has a fractal set of singularities [152]. This is a phenomenon analogous to the one found in Hamiltonian chaotic scattering in three-degree-of-freedom systems [29,200,100]. The transition point, at which $D_{\mathrm{s}} = 2$, is given for the map M^{-1} by $\Lambda = \Lambda_{\mathrm{c}} = 1/4$. If the flow is of Type I however, this transition does not occur. This is an important difference in the dynamics of the two kinds of flows.

6.2. Reaction

We now let the advected particles be active and investigate the autocatalytic reactive dynamics for the 3D flow. Although we have used a discrete map acting at integer multiples of a period T to understand the advection dynamics of a 3D flow, we will now switch to a continuous-time approach of reactivity, because it is easier to grasp. The discrete case will be investigated in Section 12.6.

We first consider the case of general Type I flows, with one unstable direction. From the previous discussion, the reacting B-particles accumulate in filamentary bands along the unstable manifold, which is a fractal set of dimension D_{u}. At any given time, these bands are columns of square base of linear size $\delta(t)$. As time evolves, δ contracts at the average rate $\bar{\lambda}$. However, because of the autocatalytic reaction, there is also a widening due to the reaction front velocity, which tends to increase δ. Thus, analogously to Eq. (41), we have the following equation for the time evolution of δ:

$$\dot{\delta} = -\bar{\lambda}\delta + 2v \ , \tag{76}$$

where v is again the velocity of the reaction front, and $\bar{\lambda}$ is the modulus of the average Lyapunov exponent along both contracting directions. For the case of map M, we have $\lambda = -\ln \Lambda/T$, where T is the period of the flow.

Let $\mathscr{V}_{\mathrm{B}}$ denote the volume occupied by the B-particles around the unstable manifold. Covering this with 3-dimensional cubes of size δ, the number of boxes is $N(\delta) = \mathscr{H} \cdot (\delta/L)^{-D_{\mathrm{u}}}$, and we get

$$\mathscr{V}_{\mathrm{B}} = \mathscr{H} L^3 \left(\frac{\delta}{L}\right)^{3-D_{\mathrm{u}}} , \tag{77}$$

where $\mathscr{H}$ is the Hausdorff volume. The number B of B-particles in the same region is

$$B = c_0 \mathscr{V}_{\mathrm{B}} , \tag{78}$$

where c_0 is the reciprocal value of the volume occupied by a single particle. From this, we can write δ as a function of B: $\delta = (c_0 L^3 \mathscr{H})^{-1/(3-D_{\mathrm{u}})} B^{1/(3-D_{\mathrm{u}})} L$. By differentiating Eq. (77) with respect to time, substituting Eq. (76), and neglecting the time dependence of $\mathscr{H}$, we can write the rate equation for the time evolution of B as [131]:

$$\dot{B} = -\kappa B + q\kappa \frac{v}{\bar{\lambda} L} B^{-\beta_{3\mathrm{D}}} , \tag{79}$$

where $q = 2(c_0 L^3 \mathscr{H})^{1/(3-D_{\mathrm{u}})}$ is a dimensionless constant, the escape rate κ is

$$\kappa = (3 - D_{\mathrm{u}})\bar{\lambda} , \tag{80}$$

and exponent $\beta_{3\mathrm{D}}$ is given in this case by

$$\beta_{3\mathrm{D}} = \frac{D_{\mathrm{u}} - 2}{3 - D_{\mathrm{u}}} . \tag{81}$$

Eq. (79) is the 3D counterpart of Eq. (47): we find a production term which is proportional to a non-integer power of B. There is an important difference, however, in the behavior of the exponent $\beta_{3\mathrm{D}}$ in the 3D case. From Eq. (81), if $D_{\mathrm{u}} > 2$, then $\beta_{3\mathrm{D}} > 0$, whereas if $D_{\mathrm{u}} < 2$, $\beta_{3\mathrm{D}} < 0$. In the two-dimensional case, only the former behavior is possible: the source term in Eq. (79) diverges for $B \to 0$, giving rise to the dynamical catalysis and the 'advantage of rarity' discussed earlier. The case $\beta_{3\mathrm{D}} < 0$, which happens in Type I flows, is only possible in 3D flows, and has no counterpart in two dimensions. In this case the source term vanishes as $B \to 0$. In our map M, the transition point between these two kinds of behavior is at $\Lambda = \Lambda_{\mathrm{c}} = 1/4$, the same as the transition point between smooth and fractal scattering functions of M^{-1}.

The steady-state value of B is

$$B^* = \left(\frac{q v}{\bar{\lambda} L}\right)^{3-D_{\mathrm{u}}} \sim \delta^{*3-D_{\mathrm{u}}} . \tag{82}$$

Since in continuum models the front velocity is proportional to the square root of the diffusion coefficient (see Eq. (33)), we have in 3D flows:

$$B^* \sim v^{3-D_{\mathrm{u}}} \sim D_{\mathrm{diff}}^{(3-D_{\mathrm{u}})/2} . \tag{83}$$

The enhancement factor is now

$$\frac{B^*(D_{\mathrm{u}})}{B^*(D_{\mathrm{u}} = 2)} \sim \left(\frac{v}{\bar{\lambda} L}\right)^{2-D_{\mathrm{u}}} \sim V^{2-D_{\mathrm{u}}} , \tag{84}$$

where V is the dimensionless velocity, defined in Eq. (54). Eq. (84) also reflects the crossover at $D_u = 2$ mentioned above.

The production term in (79) is proportional in the steady state (when it equals κB^*) to $\kappa\bar{\lambda}^{-D_u-3}$. Since, however, the Lyapunov exponent is proportional to the escape rate (see (80)), we find

$$P \sim \kappa^{D_u-2} . \tag{85}$$

The limit of large escape rates is thus completely different for $D_u > 2$ and $D_u < 2$: in the former case, the production diverges as $\kappa \to \infty$, while in the latter, P goes to zero. In case of the 3D baker map M, a large escape rate can be present for $\Lambda \to 0$ only, which implies (see (73)) $D_u \to 1$, $D_s \to 2$. Thus $P \sim 1/\kappa$ as $\kappa \to \infty$, for Type I flows in steady state for large κ.

We have dealt with Type I flows above, but the same approach can be applied with practically no change to Type II flows (with 2 unstable directions). The only difference is that the unstable manifold is now a family of surfaces, and δ is to be interpreted as the average thickness of reactants covering the surfaces. All the equations above apply unchanged. Type II flows, however, have an unstable manifold dimension which is always greater than 2 (cf. Eq. (75)), and therefore do not present a decay of the activity for small B^*, or large κ, as Type I flows do. This is a fundamental difference in the reaction dynamics between Type I and Type II flows. In particular, $\Lambda \to 0$ implies (see (74)) $D_u \to 2$, $D_s \to 1$, and thus P is independent of κ in this limit, for Type II flows.

6.3. Asymmetric contraction

We now study the case of a 3D flow with different contraction factors.

Let us consider the purely advective dynamics first, for the case of Type I flows, which is the type with more interesting reactive dynamics. By considering a generalized baker map M with $\Lambda_x \neq \Lambda_y$, $\Lambda_x, \Lambda_y < \frac{1}{2}$, the intersection of the set of remaining volume after n applications of the map with a plane parallel to the xy plane resembles again Fig. 33d, but the squares are now rectangles, with different sides $\delta_x(n) = \Lambda_x^n \delta_x(0)$ and $\delta_y(n) = \Lambda_y^n \delta_y(0)$. In the limit as $n \to \infty$, an 'anisotropic' double Cantor set is formed, which is the unstable manifold of the chaotic saddle. This Cantor set is characterized by two *partial dimensions* D_x and D_y, corresponding to the two contracting directions of the xy plane. D_x is the fractal dimension of the intersection of a one-dimensional segment parallel to the x axis with the Cantor set. Similarly, D_y is the dimension of the intersection with a segment parallel to the y-axis. Using the two partial dimensions, the number $N(\delta_x, \delta_y)$ of rectangles of linear size δ_x and δ_y necessary to cover the two-dimensional xy section of the Cantor set is [56]

$$N(\delta_x, \delta_y) = \mathscr{H}\left(\frac{\delta_x}{L}\right)^{-D_x}\left(\frac{\delta_y}{L}\right)^{-D_y} , \tag{86}$$

where $\mathscr{H}$ is a constant. The total fractal dimension of the unstable manifold is given in terms of D_x and D_y by

$$D_u = 1 + D_x + D_y . \tag{87}$$

The relation between the partial dimensions and the parameters Λ_x and Λ_y is simply:

$$D_x = -\ln 2/\ln \Lambda_x, \quad D_y = -\ln 2/\ln \Lambda_y . \tag{88}$$

The escape rate κ is given by

$$\kappa T = -\ln(4\Lambda_x\Lambda_y) \ . \tag{89}$$

We now introduce the autocatalytic reaction, whose effect is, as before, to enlarge each rectangle by a certain amount after each iteration of the map, thereby counteracting the loss due to escape. The actual size of a rectangle filled with B-particles also depends on the strength of the reaction. As we did previously in the symmetric case, we consider the continuous limit, when δ_x and δ_y are taken to be continuous functions of the time t. Then, the effect of contraction and frontal reaction propagation can be described by the following differential equations:

$$\dot{\delta}_i = -\overline{\lambda}_i\delta_i + 2v, \quad i = x, y \ , \tag{90}$$

where $\overline{\lambda}_i$ are the contracting average Lyapunov exponents in modulus, and v is the front velocity. For the map M, $\overline{\lambda}_i = -\ln\Lambda_i/T > 0$.

From Eq. (90), and taking $\mathscr{H}$ to be constant, the total number of B-particles around the unstable manifold is

$$B = c_0 L\delta_x\delta_y N(\delta_x, \delta_y) = c_0\mathscr{H}L^{D_u}\delta_x^{1-D_x}\delta_y^{1-D_y} \ . \tag{91}$$

Using Eq. (91), we find a differential equation for the time evolution of the particle number B:

$$\dot{B} = -\kappa B + 2v[(1-D_x)/\delta_x + (1-D_y)/\delta_y]B \ , \tag{92}$$

where

$$\kappa = (1-D_x)\overline{\lambda}_x + (1-D_y)\overline{\lambda}_y \ . \tag{93}$$

Since there are two independent widths δ_x and δ_y, now we cannot use Eq. (91) to express both δ_x and δ_y as functions of B alone to get a closed equation for B, as we did previously. What we can do is to express one width (say δ_y) as a function of B and the other width. The active dynamics is then governed by two *coupled* differential equation (the one for B and the other for δ_x). This means that the nature of the time evolution is quite different from the simple case studied previously ($\Lambda_x = \Lambda_y$).

If one of the contractions is very fast, say the one along the y direction, then δ_y can be assumed to have reached its steady state, $\delta_y = \delta_y^* = 2v/\overline{\lambda}_y$, while δ_x is still evolving. This approximation enables us to express δ_x via B as

$$\delta_x = B^{1/(1-D_x)}(c_0 L^{D_u}\mathscr{H})^{-1/(1-D_x)}(\delta_y^*)^{-(1-D_y)/(1-D_x)} \ . \tag{94}$$

From (92) we then find

$$\dot{B} = (1-D_x)\overline{\lambda}_x\left[-B + q'\frac{v}{\overline{\lambda}L}\left(\frac{v}{\overline{\lambda}L}\right)^{(1-D_y)/(1-D_x)}B^{-\beta'_{3D}}\right] \ , \tag{95}$$

where q' is a geometric factor given by

$$q = 2^{(3-D_u)/(1-D_x)}(c_0 L^3\mathscr{H})^{1/(1-D_x)}$$

and

$$\beta'_{3D} = \frac{D_x}{1-D_x} > 0 \ .$$

In this case the active dynamics is completely determined by the particle number again, and the rate equation is of similar type as in 2D flows (cf. Eq. (47)). This shows that, if one of the directions is contracting at a much faster rate than the other one, the dynamics is effectively two-dimensional. If, however, the two directions have similar contraction rates, Eq. (95) is no longer applicable, and the dynamics is truly three-dimensional, and (90), (92) apply.

7. Reactions in general, non-periodic flows

In this section, we consider reactions taking place in long lasting, aperiodic flows. For simplicity, a 2D case is considered again. By making use of the theory of random maps, a model is presented which yields a rate equation displaying a singular production term, similar to the corresponding case of time periodic flows [85]. Therefore, the singular enhancement (as well as the other features of active chaos highlighted in the previous sections) does not depend on time periodicity, and is found also in flows with random time dependencies [85].

7.1. Random maps and random fractals

In Nature, strictly time-periodic flows are rarely found. Although it is hopeless to find a completely general theory of reactions, there is a class of flows to which our previous theory can be extended. Most flows display *coherent structures*, that is, well-defined persisting space–time patterns [71]. The theory we develop applies to flows in which the coherent structures are the dominating feature. It is assumed that their number is fixed, but their position and shape might change *irregularly, chaotically* in time. In this case, it makes sense to model the advection dynamics as a low-dimensional dynamical system, which can be described on snapshots taken with some period as a map with randomly varying parameters. From now on, we use the term *random flows* to designate such flows.

The advection dynamics can thus be described by a *random map* [169,226,194], in which the parameters μ are assumed to be taken from a stationary ensemble. The parameter μ_n taken at time instant n can then be written as

$$\mu_n = \overline{\mu} + \Delta\mu_n \ , \tag{96}$$

where $\overline{\mu}$ is the average value, and $\Delta\mu_n$ denotes the fluctuation. The overall strength of these fluctuations can be characterized by the relative variance

$$r = \frac{\overline{\Delta\mu_n^2}}{\overline{\mu}^2} \ . \tag{97}$$

Overbars denote averages taken with respect to the stationary ensemble associated with the given random flow.

In open random maps, both the chaotic saddle and its unstable manifold are fractal objects which never repeat their shapes in time [76,140]. Their dimension is, however, well-defined and *time-independent* [169,76,140]. The dimension of the unstable manifold is denoted by D_r where the subscript r reminds us of the fact that the dimension depends on the strength of fluctuations. The dimension D of the nonrandom flow is recovered for $r = 0$.

The chaotic saddle has a positive average Lyapunov exponent $\overline{\lambda}_r$ whose value also depends on the strength r of randomness. The generalization of the Kantz–Grassberger relation [79] is also valid for random maps [104]. This means that the dimension D_r of the chaotic saddle's unstable manifold can be expressed as

$$D_r = 2 - \frac{\kappa_r}{\overline{\lambda}_r} \ , \tag{98}$$

where κ_r denotes the escape rate from the random chaotic saddle.

7.2. Reactions in random flows

We use again an autocatalytic reaction for definiteness, but our results have more general validity. The advection carries an initial distribution of B particles into thin stripes of typical width $\delta(t)$ surrounding the unstable manifold. The advection makes a width δ of the B band contract at a rate given by $-\lambda\delta$, where λ is the instantaneous Lyapunov exponent. Hence, the total time evolution of δ, with the reaction taken into account, is given again by

$$\dot{\delta} = -\lambda\delta + 2v \ , \tag{99}$$

which can be conveniently rewritten as

$$\frac{\mathrm{d}\,\ln\,\delta}{\mathrm{d}t} = -\lambda + 2v/\delta \ . \tag{100}$$

In random flows, λ is a random variable, taken from some ensemble. By averaging over the stationary distribution of the randomly varying parameters of the flow, we get

$$\frac{\mathrm{d}\,\overline{\ln\,\delta}}{\mathrm{d}t} = -\overline{\lambda}_r + \overline{\left(\frac{2}{\delta}\right)v} \ . \tag{101}$$

There is no average on v, since it is an intrinsic property of the reaction.

In order to derive the rate equation, we note that relations (44) and (45) are still valid, but now the Hausdorff volume is a random variable, too. We can thus write (cf. (46))

$$\frac{\mathrm{d}}{\mathrm{d}t}\ln B = (2 - D_r)\frac{\mathrm{d}}{\mathrm{d}t}\ln\delta + \frac{\mathrm{d}}{\mathrm{d}t}\ln\mathscr{H} \ . \tag{102}$$

The above formula is valid for a particular element of the ensemble. Taking the average, and using Eq. (101) and noting that the average of the $\mathscr{H}$ factor is time-independent (since the ensemble is assumed to be stationary), we find

$$\frac{\mathrm{d}}{\mathrm{d}t}\overline{\ln B} = -\overline{\lambda}_r(2 - D_r) + (2 - D_r)v\,\overline{\left(\frac{2}{\delta}\right)} \ . \tag{103}$$

In view of the Kantz–Grassberger relation, Eq. (98), we identify the first term on the right-hand side of (103) as $-\kappa_r$.

To get a closed-form equation for $\overline{B}$ from Eq. (103), we need to derive a relation between $\overline{B}$ and $\overline{\delta}$. We do this by assuming weak relative fluctuations. The validity of this assumption is to be checked

a posteriori. In accordance with the stationarity assumption, we now write $\delta = \overline{\delta} + \Delta\delta$, where $\Delta\delta$ satisfies $\overline{\Delta\delta} = 0$. In view of the aforementioned weak relative fluctuations, the averaged terms in Eq. (101) are well approximated by

$$\overline{\ln\delta} = \ln\overline{\delta} - \frac{1}{2}\rho_r, \quad \overline{\left(\frac{1}{\delta}\right)} = \frac{1}{\overline{\delta}}(1+\rho_r) \ , \tag{104}$$

where

$$\rho_r = \overline{(\Delta\delta/\delta)^2} \ll 1 \tag{105}$$

is the relative variance of the width, which depends on the strength of parameter fluctuations r. For simplicity we assumed that the cross-correlation $\overline{\Delta c \Delta\delta}$ is zero.

Substituting Eq. (104) into Eq. (101), we get the equation for the time evolution of $\overline{\delta}$:

$$\frac{\mathrm{d}\overline{\delta}}{\mathrm{d}t} - \frac{1}{2}\overline{\delta}\frac{\mathrm{d}\rho_r}{\mathrm{d}t} = -\overline{\lambda}\,\overline{\delta} + 2v(1+\rho_r) \ . \tag{106}$$

Comparing with Eq. (101), we see that the effect of randomness on the average width is a multiplicative correction on the production term, which can be thought of as an increase in the effective reaction velocity v. In other words, *randomness enhances productivity*, as compared to the non-random case.

Next, we average the expression $B = c_0 \mathscr{H} L^{D_r} \delta^{2-D_r}$ (see (44) and (45)), and use the expansions $\mathscr{H} = \overline{\mathscr{H}} + \Delta\mathscr{H}$ ($\overline{\Delta\mathscr{H}} = 0$) and $\delta = \overline{\delta} + \Delta\delta$. The result is

$$\overline{B} = \overline{\mathscr{H}}\,\overline{\delta}^{2-D}\left(1 + \frac{(2-D_r)(1-D_r)}{2}\rho_r\right) \ , \tag{107}$$

where for simplicity we also assumed that the cross-correlation term $\overline{\Delta\delta\Delta\mathscr{H}}$ vanishes. Within this approximation,

$$\overline{\ln B} = \ln\overline{B} - (2-D_r)^2\rho_r/2 - 1/2\overline{\Delta\mathscr{H}^2}/\overline{\mathscr{H}}^2 \ .$$

Substituting this result in Eq. (103) and rearranging, we get the final form for the time evolution for the average number B of reacting particles:

$$\frac{\mathrm{d}\overline{B}}{\mathrm{d}t} = -\kappa_r\overline{B} + \kappa_r q\frac{v}{\overline{\lambda}L}\overline{B}^{-\beta_r}\left(1 + \frac{3-D_r}{2}\rho_r\right) + \frac{(2-D_r)^2}{2}\overline{B}\frac{\mathrm{d}\rho_r}{\mathrm{d}t} \tag{108}$$

up to leading order in ρ_r. Here $q = 2(c_0 L^2\overline{\mathscr{H}})^{1/(2-D_r)}$ is an average overall geometric factor, and the power β_r is expressed as (49)

$$\beta_r = \frac{D_r - 1}{2 - D_r} \ . \tag{109}$$

Since $1 < D_r < 2$ for a chaotic system, the production term in Eq. (108) has a singular dependence on $\overline{B}$, and it diverges for $\overline{B} \to 0$. The relation between β_r and D_r is formally the same as in the time-periodic case (see (49)), but here D_r is the dimension of the unstable manifold *of the random flow*. Although the $\overline{B}$-dynamics is coupled to that of ρ_r in (108), we can assume that ρ_r reaches a steady state faster than $\overline{B}$, i.e., the last term is negligible. The equation is then of similar type as (47). Thus, we have shown that the

singular enhancement of production is present *even in random flows*, and hence cannot be dismissed as an effect of artificial time-periodicity assumptions.

Comparing Eq. (108) with the corresponding Eq. (47) for time-periodic flows, the random nature of the flow is manifested by $D_r > D$, where D is the dimension of the nonrandom flow (the limit $r, \rho \to 0$) (see e.g. [76,140]) from which $\beta_r > \beta$ follows. This confirms the fact that productivity is enhanced by randomness (the prefactor $1 + (3 - D_r)\rho_r/2$ is larger than one). From Eq. (108) it follows that properties described in Section 4 also hold for reactions in random flows.

7.3. Numerical results

In order to test the theory, we have chosen the flow generated by 4 point vortices [140], which is one of the simplest 2D flows that has a non-periodic sustained time dependence (see Section 2.2.3). Thus, in this system the randomness is generated by the internal dynamics of the flow, and not by external environmental perturbations. The vortices of the model might represent coherent structures (mentioned in the beginning of this section). This chaotic vortex system can also be considered as a local model of 2D turbulence over a finite period of time [11,162].

We numerically implement the autocatalytic reaction in the following way. We choose a rectangular region $\mathscr{R}$ containing initially all the four vortices. We then partition $\mathscr{R}$ into $n_x n_y$ rectangular grid cells, corresponding to the division of the x- and the y-axis into n_x and n_y segments, respectively. As the system evolves in time, the center of the four vortices undergoes an overall drift [140]. For this reason, we define $\mathscr{R}$ in the co-moving coordinates x_c and y_c, defined by $x_c = x - \frac{1}{4}\sum_{i=1}^{4} x_i$ and $y_c = y - \frac{1}{4}\sum_{i=1}^{4} y_i$, (x_i, y_i) being the instantaneous position of vortex i. In these new coordinates, the motion of the vortices is confined to a finite area of the (x, y) plane since the total vorticity is zero, $\sum_{i=1}^{4} \Gamma_i = 0$ (cf. Section 2.2.3).[4] Region R is chosen so that if a particle leaves R, it will necessarily escape towards infinity. The numerical simulation of the reaction is identical to the one described in Section 4.1, except that the spatial region of interest undergoes a drift, as time goes on.

We use vortex strengths $\Gamma_1 = \Gamma_2 = \Gamma_3 = 1$, $\Gamma_4 = -3$, and choose $R = [-1.3, 1.3] \times [-0.2, 1.4]$. The initial vortex positions are $x_1 = x_2 = x_3 = x_4 = 0$, and $y_1 = 0.1$, $y_2 = 0.6$, $y_3 = 1$, $y_4 = 0.4$. The reaction time lag is kept constant, at the value of $\tau = 2$. We start with a uniform initial distribution of B particles on the grid. After a few reaction steps, the system reaches a state of dynamical equilibrium, which is independent of the initial distribution. Because of the flow's aperiodicity, the number of B particles does not stay constant in time, but fluctuates in a random-like fashion, see the inset in Fig. 34. The theory predicts that after the transient period is over, the B particles should be distributed in a filamentary fashion, shadowing the unstable manifold of the advection dynamics. In other words, the B distribution is a fractal for scales larger than the width δ. In Fig. 34, we show the B distribution after 7 reaction steps, corresponding to dimensionless time $t = 14$. By this time the transient phase is over, and the system is in a steady state. It is clear from Fig. 34 that the B distribution is very intricate and filamentary. In order to test the theory quantitatively, we calculate the fractal dimension of this distribution, which should be equal to the dimension of the unstable manifold of the purely advective (without reaction) dynamics. To calculate the fractal dimension of the steady B distribution, we compute the equilibrium distribution at the same time $t = 14$ for several values of the grid size $\varepsilon = \sigma$, keeping all the other parameters constant. Let $\mathscr{R}_0$

[4] For $N = 4$, the case $\sum_{i=1}^{4} \Gamma_i = 0$ is exceptional and is shown to be integrable [147]. The resulting vortex motion is, however, complicated enough so that on snapshots taken with a fixed period the dynamics appears to be random.

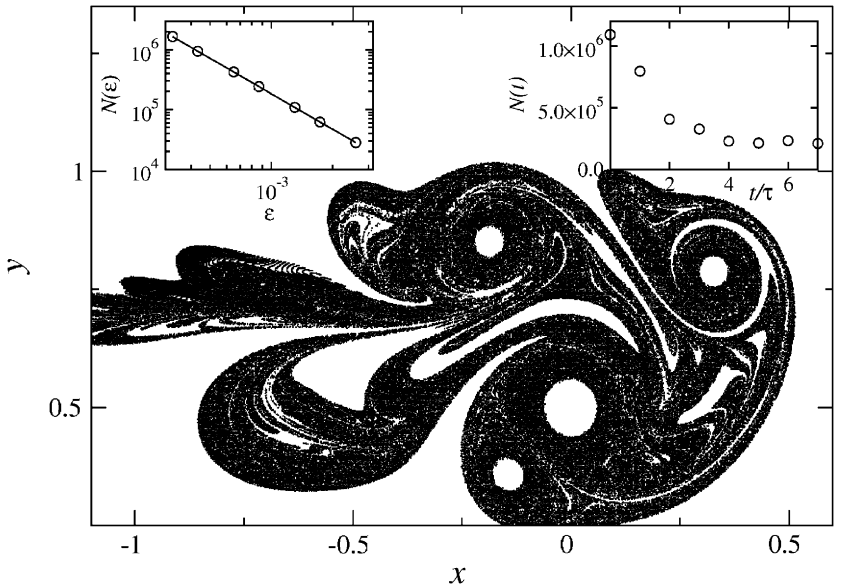

Fig. 34. Distribution of B-particles at time $t = 14$, right after the seventh reaction step. The upper left inset illustrates the scaling of $N(\varepsilon)$ (note that $\varepsilon = \sigma$ the reaction range). The result is a well-defined power law, giving a fractal dimension of 1.96. The upper right inset shows the time evolution of the number of B particles, where the time t is measured in units of the reaction time τ.

be a subregion of the rectangle $\mathscr{R}$. If $N(\sigma)$ is the number of B particles in the steady state distribution within $\mathscr{R}_0$, it should scale as $N(\sigma) \sim \sigma^{-D_B}$, with D_B as the dimension of the B-distribution, for scales larger than σ. The left inset shows the numerical result for N as a function of σ. The counting region $\mathscr{R}_0$ is the one shown in Fig. 34. It is seen that $N(\sigma)$ does indeed follow a power law, from which we find $D_B = 1.96 \pm 0.01$. Comparing this with the value $D_r = 1.95$ of the unstable manifold dimension of the advection dynamics, calculated in Ref. [140], we see that they match to within numerical uncertainties.

8. Effects of transport barriers and non-hyberbolicity

We have focused so far on hyperbolic advection dynamics, that is, when all the orbits in the chaotic saddle are unstable. However, in many cases of practical interest the advection dynamics is non-hyperbolic, having stable (actually, elliptical) periodic orbits around the chaotic saddle. It is shown that this can have important consequences when the advected particles are chemically or biologically active [24,132,130].

8.1. The effective dimension D_{eff}

For concreteness, we focus again on two-dimensional incompressible flows with a periodic time dependence, in which the motion of passively advected particles is given by a Hamiltonian dynamical system as shown in Section 2. The non-hyperbolicity is due to the presence of *KAM islands* [152,22] in phase space, which consist of regions within which the orbits are confined. These islands are bounded by *absolute transport barriers*, which the flow cannot cross. These islands appear in a complex hierarchical

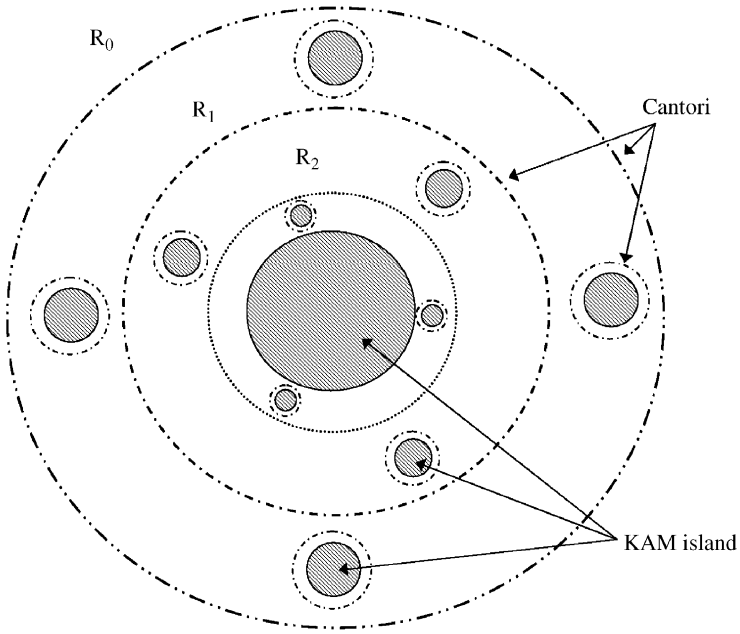

Fig. 35. Schematic illustration of the hierarchical structure of KAM islands and Cantori, generic in non-hyperbolic flows. Solid circles represent KAM tori, and Cantori are represented by circles with 'gaps'. R_i denotes a region belonging to level i in the hierarchy of Cantori.

structure in all scales, in a fractal-like way. Physically, they correspond to vortices in the flow, from which fluid does not escape. Such vortices are very common in 2D flows, and they have been observed in environmental flows, such as in the atmosphere (the stratospheric polar vortex, which plays a crucial role in the process of ozone depletion [93,58], is in zeroth-order approximation such a barrier), and also in ocean circulations [2,3]. Associated with KAM islands (or vortices), there is a set of *Cantori*, remnants of broken up KAM tori, which are 'leaky' invariant sets surrounding the islands. Even though particles can cross the Cantori, they may take a long time in doing so, and as a consequence the Cantori act as *partial transport barriers*. The overall picture of the phase space in non-hyperbolic (2D) systems is sketched in Fig. 35. This 'segmentation' of the phase space caused by the presence of KAM islands and Cantori has no counterpart in hyperbolic systems.

We introduce the concept of effective dimension for the passive (non-reactive) dynamics. In open chaotic systems, the stable (and unstable) manifold of the invariant set is fractal, with the fractal dimension D defined by the limit

$$D = -\lim_{\varepsilon\to 0} \ln N(\epsilon)/\ln(\varepsilon)\ , \tag{110}$$

where $N(\varepsilon)$ is the number of boxes of size ε needed to cover the stable (and unstable) manifold. D satisfies $1 \leqslant D \leqslant 2$. For non-hyperbolic systems, it is known [103,34] that D always assumes the maximum value $D = 2$.

Limit (110) converges very slowly and is only attained for *very* small values of ε. In fact, in non-hyperbolic systems, a log–log plot of $N(\varepsilon)$ versus $1/\varepsilon$ is typically, to a very good approximation,

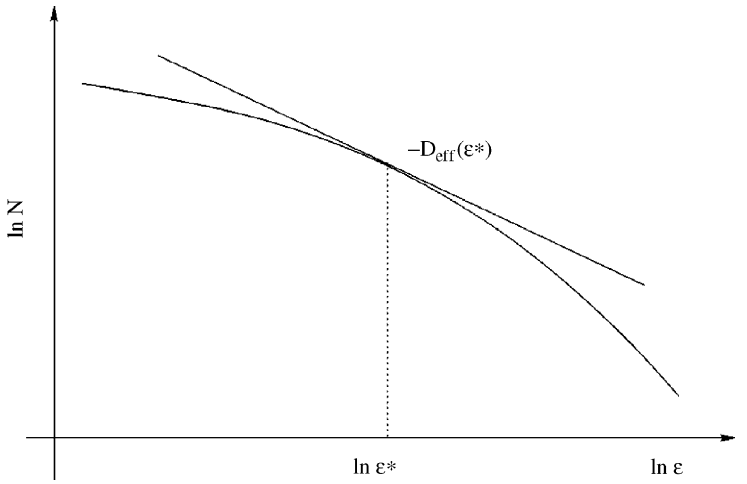

Fig. 36. Illustration of the concept of effective dimension, the slope of the tangent to the $\ln N$ vs. $\ln 1/\varepsilon$ curve.

a straight line with a slope less than 2 over an ε range of many orders of magnitude, even though from Eq. (110), the slope is 2 for $\varepsilon \to 0$. The slope in fact does approach 2 for ε small enough. But if for some physical reason one has a finite resolution ε (given, for instance, by the size of the advected particle), the dimension that is practically seen is given by the effective dimension D_{eff} [21], defined as an approximation to D for finite ε (see Fig. 36):

$$D_{\text{eff}}(\varepsilon) = -\frac{\mathrm{d}\,\ln\,N(\varepsilon)}{\mathrm{d}\,\ln\varepsilon} \approx \text{const.} \quad \text{for } \varepsilon_1 < \varepsilon < \varepsilon_2\ , \tag{111}$$

and $\varepsilon_1 \ll \varepsilon_2$. Obviously, D_{eff} satisfies $D_{\text{eff}}(\varepsilon) \to 2$ as $\varepsilon \to 0$.

The effective dimension D_{eff} depends also on the location in phase-space for non-hyperbolic systems. This is due to the presence of Cantori which act as transport barriers: particles inside a Cantorus take a much longer time to escape than those that start outside it. This means that the piece of the chaotic saddle's stable manifold that is within the Cantorus is more stretched and folded than that outside. At finite resolution, its filamentation appears to be more involved and, as a result, the effective dimension in the inner region should be higher than in the outer region.

Before testing this idea, we introduce a numerical model. We use the 2D Hamiltonian (area-preserving) map given by [64,39]

$$\begin{aligned} x_{n+1} &= \lambda[x_n - (x_n + y_n)^2/4]\ , \\ y_{n+1} &= \lambda^{-1}[y_n + (x_n + y_n)^2/4]\ , \end{aligned} \tag{112}$$

where $\lambda > 0$ is a real parameter. The discrete-time system (112) can be considered as a stroboscopic map of some time-periodic 2D incompressible flow. Map (112) has an open dynamics, with trajectories coming from infinity, and being scattered towards infinity again after a transient time. For $\lambda < 6.5$, the map is non-hyperbolic [103]. We fix $\lambda = 6$. In Fig. 37a, we show the Poincaré section for this system, found by plotting many iterations of a few initial conditions. There is a stable period-2 orbit, which is the center of a KAM island composed of two pieces. This KAM island is embedded within a Cantorus, which can be seen by the long time it takes for a particle in its interior to escape, as is evidenced by the

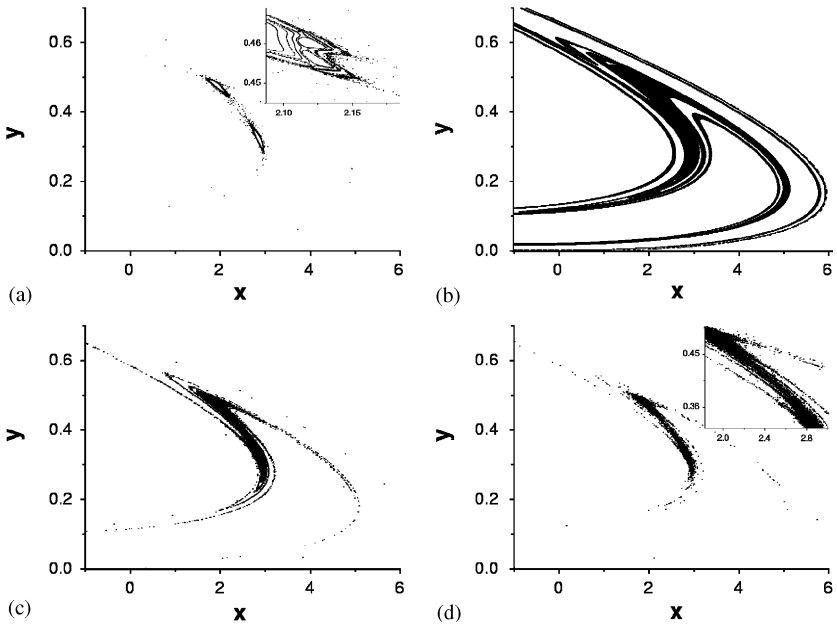

Fig. 37. (a) Orbits of the map (112) for $\lambda = 6$. The inset shows a magnification of a small region. Complex structures of stable orbits and Cantori can be seen. (b) Steady state distribution of the autocatalytic process for $\lambda = 6$ and $\tau = 1$; (c) same as (b), with $\tau = 50$; (d) same as (b), with $\tau = 200$. The magnification in the inset shows the filamentation of the region lying between the two KAM islands.

outermost orbit, shown in the figure as a cloud of points surrounding the islands. Orbits initialized within the Cantorus have a much longer average escape time than those orbits initialized outside it. There are smaller Cantori embedded within the big one, corresponding to even larger escape times, and so on, in a hierarchical structure similar to that of the KAM islands themselves. Evidence of this 'fine structure' is seen in the inset of Fig. 37a, which shows a magnification of the island structure. Note that, although we are looking at the particular case of map (112) for convenience, this self-similar structure of KAM islands and Cantori is a general feature of any non-hyperbolic Hamiltonian system [152].

We now use the dynamical system (112) to calculate the effective dimension D_{eff}. To do this, we use the uncertainty method [57] to calculate $f(\varepsilon)$, the fraction of boxes of size ε needed to cover the fractal set (compared with the total number $\sim \varepsilon^{-2}$). The effective dimension is then obtained from

$$2 - D_{\text{eff}}(\varepsilon) = \frac{\mathrm{d}\,\ln f(\varepsilon)}{\mathrm{d}\,\ln \varepsilon}\ . \tag{113}$$

We first calculate D_{eff} outside the Cantorus, and obtain $D_{\text{eff}} = 1.54$ (Fig. 38a). Inside the first Cantorus, we find a considerably greater value $D_{\text{eff}} = 1.91$ (Fig. 38b). This shows that D_{eff} indeed depends on the location in phase space, and is greater inside a Cantorus. There is, however, an infinite number of Cantori, organized hierarchically around the KAM islands. As we go deeper and deeper within the Cantorus structure, the typical escape time increases, and so does D_{eff}. In fact, we are able to find regions in system (112) whose effective dimension is numerically indistinguishable from 2.

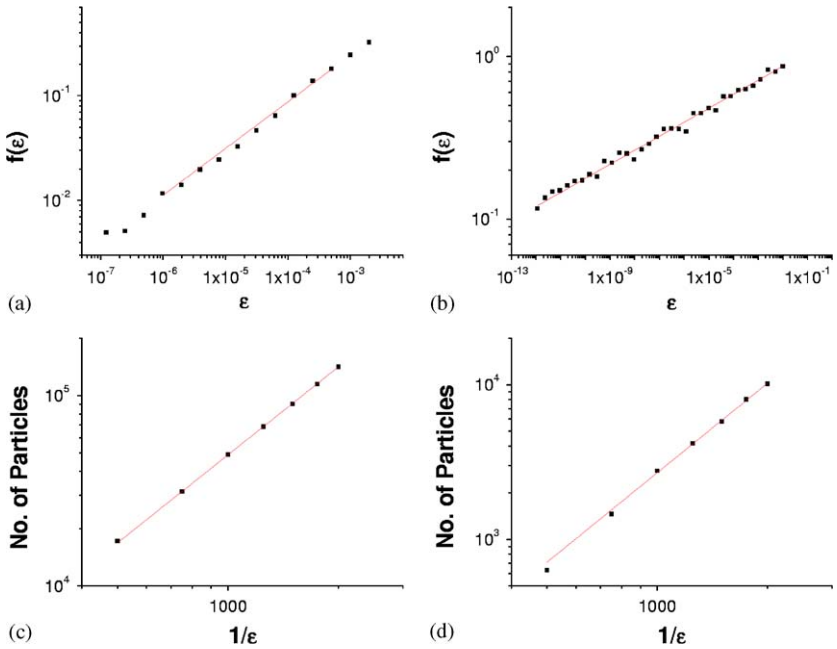

Fig. 38. (a) $f(\epsilon)$ outside the Cantorus; the slope gives $D_{\text{eff}} = 1.54 \pm 0.01$. (b) $f(\epsilon)$ inside the first Cantorus; $D_{\text{eff}} = 1.915 \pm 0.003$. (c) Number of reacting particles in the filamentary component of the equilibrium distribution as a function of the inverse of the grid size, for $\tau = 1$; the slope gives directly $D_{\text{ob}} = 1.53 \pm 0.01$. (d) Same as (c), with $\tau = 200$; $D_{\text{ob}} = 1.92 \pm 0.03$.

8.2. Consequences for the reaction dynamics

We now discuss the consequences of non-hyperbolicity for the reaction dynamics, using as usual the model of autocatalytic reaction presented in Section 3.

From the above discussion, we find that the deeper we go into the hierarchy of Cantori, the longer it takes to escape, on average. Let us use an integer index i to denote how many levels down in this hierarchy a certain point in phase space is (assuming that the point is not within a KAM torus). Let $T^{(i)}$ be the typical escape time from a level with index i (region R_i in Fig. 35). As we have seen in the previous subsection, $T^{(i)}$ increases with i, and we have $T^{(i)} \to \infty$ as $i \to \infty$. Analogously, let $D_{\text{eff}}^{(i)}$ stand for the effective dimension of a level with label i, and let $\overline{\lambda}_{\text{eff}}^{(i)}$ be the corresponding effective average Lyapunov exponent. As $i \to \infty$, $D^{(i)} \to 2$, as we have seen. Since large values of i mean that the particle spends a long time close to the KAM tori, we expect that $\overline{\lambda}_{\text{eff}}^{(i)} \to 0$ as $i \to \infty$ [103,34].

Within a level i, a band of reacting material has an average width $\delta^{(i)}$ which satisfies

$$\dot{\delta}^{(i)} = -\overline{\lambda}_{\text{eff}}^{(i)} \delta^{(i)} + 2v \ . \tag{114}$$

This equation is analogous to Eq. (41), with the variables replaced by their effective values. The equilibrium value $\delta^{(i)*}$ of the bandwidth is thus given by

$$\delta^{(i)*} = 2\frac{v}{\overline{\lambda}_{\text{eff}}^{(i)}} \ . \tag{115}$$

Since $\bar{\lambda}_{\mathrm{eff}}^{(i)}$ decreases to zero as i increases, we see from the above expression that $\delta^{(i)*}$ increases as i increases. Thus, as we go down the hierarchy of Cantori, the bands become thicker, and there will be a value i_{c} above which all the bands corresponding to that level (and those with $i > i_{\mathrm{c}}$) overlap, and the fractal filamentary structure will not be visible below this level. This tendency is further reinforced by the fact that the size of the regions in phase space corresponding to level i decreases with increasing i. Regions with $i > i_{\mathrm{c}}$ are seen as a solid block of B particles, with no gaps, and no filaments. If we exclude this 'bulky' region, the effective dimension of the B distribution is equal to that of the highest value of i for which filamentation is still discernible. In symbols, $D_{\mathrm{ob}} = D_{\mathrm{eff}}^{(i_{\mathrm{c}})}$, where D_{ob} denotes the 'observed dimension' of the B-particle distribution.

From Eq. (115), $\delta^{(i)*}$ is proportional to the reaction front velocity, which implies that the critical level i_{c} increases with decreasing v. By considering v as a variable, by decreasing v, i_{c} increases abruptly at certain critical values of v. As a consequence, the observed dimension D_{ob} increases by jumps, approaching 2 as v approaches 0. This infinite sequence of transitions is a consequence of the hierarchy of KAM tori and Cantori, and is thus a unique feature of non-hyperbolic flows (that is, flows which possess transport barriers).

In order to test the phenomena predicted above, we use the space–time discretization procedure explained in Section 4.1 to simulate numerically the advection–reaction dynamics in map (112). We initially fix the reaction time $\tau = 1$ (meaning one reaction at each iteration of the map). After an initial transient time, we find that the space distribution of the reacting particles settles down to a steady state that is independent of the initial conditions (except those that lead to the empty equilibrium, corresponding to all particles escaping after a finite time). The steady state distribution is plotted in Fig. 37b. This distribution represents again a dynamical equilibrium, when particles are produced by the reaction at the same rate with which they escape through advection.

The distribution of Fig. 37b is made up of two components: a bulky component $\mathscr{B}$, which includes the region corresponding to the KAM islands and the outermost Cantorus (compare with Fig. 37a), and a filamentary component $\mathscr{F}$, surrounding $\mathscr{B}$ (see Fig. 37b). The existence of $\mathscr{B}$ is due to the presence of the KAM islands: the finite reaction front velocity v causes the B particles to penetrate within the KAM tori, which is not possible in the purely advective dynamics. In fact, not only are the islands taken over by the reacting particles, but, in our case, also their surrounding Cantori. In the case of Fig. 37b, $\tau = 1$ corresponds to a value of v for which the bands in the first level of Cantori already overlap, rendering this whole region a solid block of reacting particles. In the case of an open hyperbolic dynamics, the region $\mathscr{B}$ is totally absent.

For hyperbolic dynamics, the equilibrium distribution has a fractal structure (down to the grid size), with an observed fractal dimension D_{ob} equal to the dimension D of the unstable set in the underlying Hamiltonian dynamics. For non-hyperbolic systems the filamentary part $\mathscr{F}$ of the distribution must have an observed dimension D_{ob} equal to the effective dimension $D_{\mathrm{eff}}(\delta^{(i_{\mathrm{c}})*})$, and not D. We have calculated the box-counting dimension of the distribution shown in Fig. 37b, after excluding the bulky component. This is shown in Fig. 38c. We have obtained $D_{\mathrm{ob}} = 1.53 \pm 0.01$, which is, within numerical error, equal to $D_{\mathrm{eff}} = 1.54$, calculated previously in the reaction free case for the region outside the first Cantorus in Fig. 38a.

To test the prediction of the sequence of transitions as v is decreased, we simulate the system's dynamics for increasing values of τ (which corresponds to decreasing v). The result for $\tau = 50$ and 200 can be seen in Figs. 37c and d, respectively. As τ is increased, the region outside the Cantorus is depleted, and above a critical value τ_{c}, part of the region within the Cantorus is 'breached', and becomes filamentary

(Fig. 37d). This τ_c corresponds to a critical value of v for the first transition of the series predicted by the theory we presented above. Comparing Figs. 37d and b, the former's structure does look more convoluted, suggesting a larger observed dimension. A box-counting calculation of D_{ob} confirms this, and gives the result $D_{ob} = 1.92$ (Fig. 38d), in excellent agreement with $D_{eff} = 1.91$, calculated previously Fig. 38b for the non-reactive dynamics. Increasing τ further (that is, decreasing v), we should in principle see other transitions, but numerical limitations do not allow us to resolve them.

We note that for arbitrarily small v, non-hyperbolic systems always have a non-empty steady state. This is another difference with hyperbolic systems, which always have a critical value of τ above which the system empties (this emptying transition is studied in Section 12.2).

8.3. Extension of the concept of fractal dimension

We can extend the concept of effective dimension to cases other than the ones treated above. The existence of a well-defined fractal scaling over decades of resolution is actually not necessary for our theory to work. For reacting systems with a filamentary distribution in configuration space, our approach only requires that, close to the steady state, $N(\varepsilon)$ be a power law of ε at the length scale around the reactive scale δ^*. This is important because many filamentary structures observed in environmental processes do not present a clear scaling over decades of resolution. This is the case, for example, for the plankton growth or for the ozone reaction [223]. Our treatment can be carried out in this case with an exponent $D_{eff}(\varepsilon = \delta^*)$ replacing the fractal dimension D, where $D_{eff}(\varepsilon)$ is defined as the slope of the $\ln N(\varepsilon)$ versus $\ln(1/\varepsilon)$ curve (see Fig. 36):

$$D_{eff}(\varepsilon) = -\frac{\mathrm{d}\,\ln N(\varepsilon)}{\mathrm{d}\,\ln \varepsilon}\ . \tag{116}$$

This is formally identical to our previous definition of effective dimension, Eq. (111). However, now we do not require that $N(\varepsilon)$ be a well-defined power law over several decades. It can be interpreted as the local slope of the curve $\ln N$ versus $\ln \varepsilon$. The theory of reaction dynamics presented here can then be applied to cases where the fractal dimension (or even the effective dimension as defined in the previous subsections) is not well-defined. We just need to replace D by D_{eff} in all expressions, where D_{eff} is to be taken at a resolution corresponding to the reactive scale δ^*. In particular, the exponent β of the rate (47) should then be evaluated with this D_{eff} in (49).

9. Effects of inertia

So far we have assumed that particles are passively advected by the fluid; in other words, that the velocity of each advected particle is always equal to the velocity of the surrounding fluid. Finite-size particles, however, *cannot* adjust, due to their inertia, instantaneously their velocity to variations of the fluid velocity. Therefore, in general the particle velocity $\mathbf{v} = \dot{\mathbf{r}} \equiv \mathrm{d}\mathbf{r}/\mathrm{d}t$ ($\mathbf{r}(t)$ is the position of the particle as a function of time) typically differs from the fluid velocity $\mathbf{u}$. In this section, we elaborate the effects of inertia on active processes [148,149,206].

9.1. Advection of finite size particles

The simplest case of non-inertial effects is when the advected particles are small spherical particles of finite size. The equation of motion for the dynamics of a small rigid spherical particle with radius a and mass m_p [119,10,127] is

$$m_p\dot{\mathbf{v}} = m_f\frac{\mathrm{d}}{\mathrm{d}t}\mathbf{u}(\mathbf{r}(t),t) - \frac{1}{2}m_f\frac{\mathrm{d}}{\mathrm{d}t}\left(\mathbf{v}-\mathbf{u}(\mathbf{r}(t),t) - \frac{1}{10}a^2\nabla^2\mathbf{u}(\mathbf{r}(t),t)\right) - 6\pi a\mu\mathbf{x}(t) + (m_p-m_f)\mathbf{g} - 6\pi a^2\mu\int_0^t \mathrm{d}\tau\frac{\mathrm{d}\mathbf{x}(\tau)/\mathrm{d}\tau}{\sqrt{\pi\nu(t-\tau)}}\ , \tag{117}$$

where

$$\mathbf{x}(t) \equiv \mathbf{v}(t) - \mathbf{u}(\mathbf{r}(t),t) - \tfrac{1}{6}a^2\nabla^2\mathbf{u}\ ,$$

$\mathbf{r}(t)$ and $\mathbf{v}(t)$ are the position and velocity of the particle, respectively, and $\mathbf{u}(\mathbf{r},t)$ is the flow field at location $\mathbf{r}$ at time t. Here m_f is the mass of the fluid displaced by the particle, and μ is the viscosity. The first term on the right-hand side is the acceleration of the fluid element in position $\mathbf{r}(t)$ at time t and represents the force exerted on the particle by the undisturbed fluid. The derivative $\mathrm{d}\mathbf{u}/\mathrm{d}t = \partial\mathbf{u}/\partial t + (\mathbf{u}\cdot\nabla)\mathbf{u}$ is the total hydrodynamical derivative. The second, third and fourth terms represents the added mass effect, the Stokes drag, and the buoyancy force, respectively. The integral is called the Basset history term, and is due to the fact that the particle modifies the flow locally. The terms involving $a^2\nabla^2\mathbf{u}$ are the so-called Faxen corrections for nonuniform flow fields. Eq. (117) is valid for small particles at low particle Reynolds numbers (that is, the Reynolds number calculated by using the particle size as the length scale). This requires that the initial velocity difference must be small as well.

For sufficiently small particle radius a, the Faxen corrections can be neglected. By assuming that the particle takes a long time to return to a fluid region visited earlier (compared to the hydrodynamical time scale), the Basset history term can also be neglected.

Taking these approximations into account, and using dimensionless variables defined by

$$\mathbf{r}\to\mathbf{r}L,\quad \mathbf{v}\to\mathbf{v}U,\quad \mathbf{u}\to\mathbf{u}U,\quad t\to\frac{L}{U}t\ ,$$

where L and U are the typical length and velocity scales of the flow, and the new variables on the right-hand side are all dimensionless, we get the following dimensionless equation of motion:

$$\ddot{\mathbf{r}}(t) = \frac{1}{St}(\mathbf{u}(\mathbf{r}(t),t)-\dot{\mathbf{r}}(t)) + w\mathbf{n} + \frac{3}{2}R\frac{\mathrm{d}}{\mathrm{d}t}\mathbf{u}(\mathbf{r}(t),t)\ , \tag{118}$$

where $\mathbf{n}$ is a vertical unit vector pointing downwards, and the dimensionless parameters are

$$St^{-1} = \frac{6\pi a\mu L}{(m_p+\frac{1}{2}m_{\mathrm{F}})U},\quad R = \frac{m_f}{m_p+\frac{1}{2}m_f},\quad w = \frac{m_p-m_f}{6\pi a\mu U\,St}g\ . \tag{119}$$

The parameter St represents the amount of damping and is called the *Stokes number*, the dimensionless decay time due to the Stokes drag. The limit of $St\to 0$ corresponds to the case of point particles with no inertia (since m_f and m_p are proportional to a^3). It is in this limit where the advection equation (1), used in the previous sections, holds. R is the mass ratio parameter, and $R<\frac{2}{3}$ corresponds to aerosols

Table 4
Range of observability of inertial effects

	Particle size	Observable effects	Drastic effects
Micro-organisms	$a = 10^{-4}$ m	2 m	2 cm
Rain drop, plankton	$a = 10^{-3}$ m	200 m	2 m
Beer can	$a = 4$ cm	400 km	4 km
Balloon, drifter	$a = 1$ m	2×10^5 km	2000 km

For particles of a given size (first column), the table gives the lengthscale L on which inertial effects on the particle trajectories are clearly observable (second column), and the length scale on which these effects are drastic (third column). The results have been obtained from Eq. (119) by postulating that the effects are observable for $St > 10^{-3}$, and drastic for $St > 10^{-1}$. We take $U = 1$ m/s, $R = 1$, $\nu = \mu/\rho_{\text{fluid}} = 10^{-6}$, consequently $St = (2/9)10^9 a^2/L$ for a and L measured in meters.

(heavier than the fluid), and $R > \frac{2}{3}$ corresponds to bubbles (lighter than the fluid). Parameter w is the scaled particle settling velocity for still fluid.

Based on the expression for St in Eq. (119), we can estimate typical length scales over which the effects due to inertia are observable. These estimates are shown in Table 4 for a wide range of particle sizes.

The general inertial dynamics (118) possesses a four-dimensional phase-space (x, y, v_x, v_y) even for planar stationary flows, whereas for the non-inertial particle dynamics the phase space is two-dimensional. This extra dimensionality of the phase space is a consequence of the fact that an inertial particle is not constrained to follow the fluid, and thus its velocity is an independent dynamical variable. Hence, there are extra degrees of freedom in the corresponding dynamical system. The inertial dynamics is dissipative, even in incompressible flows, and the phase-space volume contracts at the rate $2/St$, which is always positive, in contrast to the non-inertial case, in which the phase-space volume in the (x, y) plane is preserved by the flow.

The dissipative character of the inertial dynamics raises the possibility that there is an attractor in phase space, which is not possible in the non-inertial approximation. It is then possible to have a *strange attractor*, or *chaotic attractor*, with a fractal geometric structure and a sensitive dynamics [12,203,24,189,27,20,148,149,106,206,155]. If there is a strange attractor of phase space dimension less than 2, its projection on the two-dimensional configuration space will also have a fractal structure. In this case, the particles accumulate on a fractal filamentary structure, much like in the case of non-inertial particles in open flows. We will see that the presence of a strange attractor in the inertial dynamics has very similar effects on the reaction dynamics, and can be understood using essentially the same formalism we used for open flows.

To illustrate the existence of a fractal distribution of inertial particles, we use a simple two-dimensional cellular flow field, given by the stream function

$$\psi(x, y) = [1 + k \sin(\omega t)] \sin x \sin y \ , \tag{120}$$

where k and ω are the amplitude and angular frequency of the temporal oscillation of the flow field, respectively [148,149,106]. This flow field consists of a square lattice of vortices rotating in alternating directions (see Fig. 39a and b), gravitation acts along the y-axis. The time-independent version of the flow dynamics ($k = 0$) was first considered in Ref. [196] as a simple model to describe the distribution of plankton resulting from the cellular motion induced by winds in lakes and oceans, often called the Langmuir circulation [102]. The effects of finite-size particles in this particular flow, without forcing

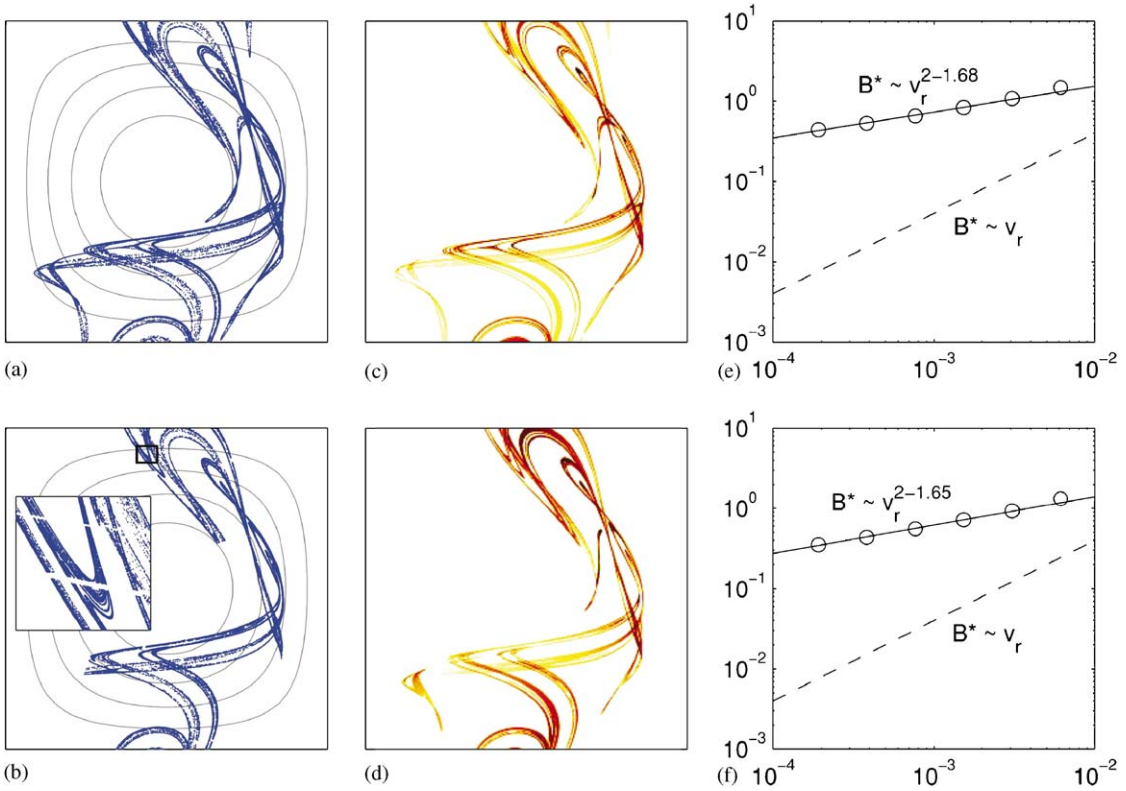

Fig. 39. (a)(b) Chaotic sets in the advection dynamics of the non-reacting inertial B-particles: (a) chaotic attractor ($k = 0.53$) and (b) chaotic saddle responsible for transient chaos ($k = 0.524$). The small rectangle at the top of the panel (b) is magnified in the inset to show the small scale (Cantor-like) structure of the saddle. The other parameters are $St = 1$, $R = 1.1$, and $w = -3.934$. (c)(d) Distribution of the B-particles after a sufficiently long time ($t = 100$ periods of the flow field). Fractal filamentation is caused by the chaotic attractor in (c) and by the chaotic saddle in (d). Only a single vortex cell of $[0, \pi] \times [0, \pi]$ is shown and the acceleration due to gravity points downward. The color coding represents the density of B-particles, in which darker colors correspond to higher density. The initial condition is a small blob of B-particles. (e)(f) The total number B^* of the B-particles in the steady state versus the reaction velocity v in the case of the chaotic attractor in (e) and the chaotic saddle in (f). The full line corresponds to the fit $B^* \sim v^{2-D}$ predicted by the theory. For reference, the $B^* \sim v$ line is shown as a dashed line, which corresponds to a non-chaotic case ($D = 1$).

($k = 0$), were analyzed in detail by Maxey [119]. In this case, the asymptotic particle trajectories are well-defined smooth curves extending from cell to cell. When $k \neq 0$ chaos sets in, and chaotic attractors appear [148,149]. Because of the spatial periodicity of the flow field, the dynamics of the particles can be restricted to a basic cell $[0, 2\pi] \times [0, 2\pi]$, with periodic boundary conditions. We consider the stroboscopic mapping taken with the period of the flow field. We find that in the bubble regime, where the particles are lighter than the surrounding fluid, with large enough amplitude of the forcing (large enough that the rotation of the vortices change their direction periodically), the attractor is chaotic, as shown in Fig. 39a (for more detailed information on the parameters used, see Refs. [148,149,206]). Since the fractality is visible in the configuration space, the dimension of the attractor is less than 2.

9.2. Reactions on chaotic attractors

We now investigate the reaction dynamics in a system of inertial particles with an attractor like the one in Fig. 39a, cf. [206]. An autocatalytic reaction is considered with only the B-particles having finite size. As we have seen, in the presence of an attractor with fractal dimension less than 2, the advected particles concentrate on a filamentary fractal structure in the configuration space, i.e., in the plane of the flow. Across these filaments, of dimension D, contraction occurs. This contraction is exponential in time with some contraction rate $\overline{\lambda}' > 0$. $\overline{\lambda}'$ depends on the flow's hydrodynamical characteristics and the particle's inertial properties.

An analysis of the bandwidth dynamics can be made in a way entirely analogous to the one presented in Section 4. We find that the width dynamics is governed by Eq. (41) with $\overline{\lambda}'$ replacing $\overline{\lambda}$, and since (44) and (45) also hold, we obtain the rate equation for the B-particles [206]

$$\dot{B} = -\overline{\lambda'}(2-D)B + q(2-D)\frac{v}{L}B^{-\beta} \tag{121}$$

with exponent β given by (49). The basic difference compared with (47) is that D is the dimension of the chaotic attractor (or of a saddle's unstable manifold living in the high-dimensional phase space) and thus $\overline{\lambda}'(2-D)$ cannot be identified now with an escape rate κ. The structure of the rate equation is, however, essentially the same.

Eq. (121) describes the competition of two effects: contraction and production. As a result, again, a *steady-state* sets in after sufficiently long time for the global distribution of the B-particles (see Fig. 39c and d). Eq. (52) is confirmed by Fig. 39e and f for inertial particles whose advection dynamics possesses a chaotic attractor and a saddle, respectively.

9.3. Effects of diffusive noise

For inertial particles of finite Stokes numbers no continuum theory applies, therefore the effect of diffusion can be taken into account by adding a noise term to the dynamical equation. The intensity of this noise is proportional to the diffusion coefficient D_{diff}. In a detailed numerical analysis [106] it was found that diffusion can *enhance* the productivity of the autocatalytic reaction in a resonance-like manner, in a phenomenon akin to *stochastic resonance*, well-known in the theory of noisy dynamical systems. More specifically, for a certain critical noise or diffusivity level D_{diff}^m (different from zero), the productivity of the reaction is found to be maximum, where the productivity increment can be as large as one quarter of the value without the presence of noise. Interestingly, this maximum is attained for a noise level that still corresponds to weak noise. The productivity versus noise level curve has a peak, characteristic of stochastic resonance (see Fig. 40). This enhancement of the productivity by noise is present under very general conditions, whether the invariant set underlying the advection dynamics is a strange attractor (sustained chaos) or a chaotic saddle (transient chaos).

10. Other reactions

In this Section, we look into the effects of an underlying open 2D chaotic flow on reactions other than the autocatalytic one. We assume that the continuum approach is applicable (inertial effects can be neglected).

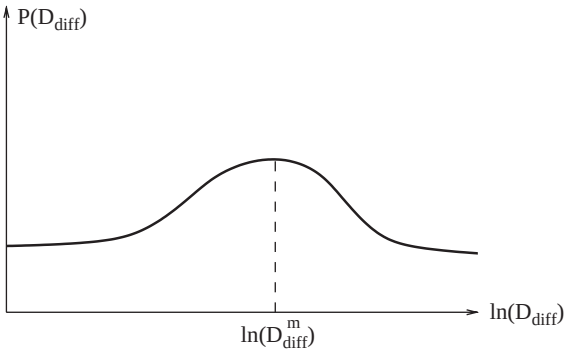

Fig. 40. Schematic diagram of the dependence of the number of inertial B-particles in a steady state on the diffusion coefficient.

In particular, we deal with bistable reactions [143], excitable media [144], flames [89,90], population dynamics of competing species [181] (already mentioned in Section 5), and collisional reactions [83].

10.1. Bistable reactions and excitable media

In general, a reaction among N chemical species with dimensionless concentrations c_i $(i = 1, \ldots, N)$ in a homogeneous environment is described by

$$\frac{\mathrm{d}c_i}{\mathrm{d}t} = -kf_i(c_1, \ldots, c_N), \quad i = 1, \ldots, N \ , \tag{122}$$

where the functions f_i characterize the reactions, and k is an overall reaction rate. Eqs. (122) are valid only for a homogeneous (perfectly mixed) environment. If the N chemical species are being advected by a fluid flow with a given velocity field $\mathbf{u}(\mathbf{r}, t)$, the corresponding concentrations $c_i(\mathbf{r}, t)$ are functions of space and time, which evolve according to the advection–diffusion–reaction equation (cf. Eq. (34) for the autocatalytic case):

$$\frac{\partial c_i}{\partial t} + (\mathbf{u} \cdot \nabla)c_i = kf(c_1, \ldots, c_N) + D_{\mathrm{diff}} \nabla^2 c_i \ . \tag{123}$$

For simplicity we assume that the diffusion coefficients corresponding to all chemical species are equal. Note that we are also assuming in Eq. (123) that the chemical reaction does not modify the flow.

Much insight can again be gained into the reaction dynamics by analyzing the Lagrangian filament slice model [136] of the process. It is now of the form

$$\frac{\partial c_i}{\partial t} - \bar{\lambda} x \frac{\partial c_i}{\partial x} = kf(c_1, \ldots, c_N) + D_{\mathrm{diff}} \frac{\partial^2}{\partial x^2} c_i \ . \tag{124}$$

By measuring time in units of $1/\bar{\lambda}$ and length in units of some linear scale L, the Damköhler and Péclet numbers ((37) and (38), respectively) appear again. The former one multiplies f_i, while the reciprocal value of Pe multiplies the second derivative.

A simple yet important case of Eq. (123) is the *bistable reaction* involving only one species ($N = 1$). A bistable reaction is a process with two stable and one unstable chemical states. In other words, there

are three values of the concentration $c_1 \equiv c$ which are fixed points of the pure chemical dynamics (122), one of which is unstable, the other two being stable. The corresponding reaction function $f(c)$ can be modeled by the form

$$f = c(c_0 - c)(c - 1) \ . \tag{125}$$

The stable fixed points are $c = 0$ (unexcited or rest state) and $c = 1$ (excited state), while the unstable one is $c = c_0 < 1$. Perturbations smaller than c_0 die out, but bigger ones, exceeding the threshold, grow until reaching the upper limit $c = 1$. In this second regime the system is qualitatively similar to an autocatalytic reaction (for which $f = c(1 - c)$). Localized perturbations generate fronts moving with a constant speed v [133] even in a medium at rest. This velocity v is, similarly to the autocatalytic case, proportional to $\sqrt{D_{\rm diff}k}$: Eq. (33) holds with $\alpha = |1 - 2c_0|/\sqrt{2}$ [133]. Correspondingly, the bandwidth equation (41) is expected to hold again, and turns out to be consistent with the Lagrangian filament slice model. Furthermore, for the total number B of particles, Eq. (47) can be applied, and the properties mentioned in Section 4 hold for the bistable reaction as well. A main difference appears in the emptying transition which is found to happen at a critical Damköhler number $Da_{\rm c}$ with a discontinuous jump [143]. The emptying transition is thus of first order in the bistable reaction, while it is of second-order in the case of the autocatalytic reaction.

Another important application of the above concepts is given by *excitable media*. An excitation in some given medium is due to the interplay of an activator chemical species C_1, which undergoes some kind of an autocatalytic growth, and an inhibitor species C_2. The presence of the latter converts the excited state into a metastable one which decays after some time to the unexcited state, which is thus the only attractor of the chemical dynamics. An important feature of excitable media is the presence of a threshold. Initial perturbations below the threshold die out quickly, while the ones above it reach the stable fixed point only after producing an excitation. Besides the transmission of neural signals and the excitation of the heart tissue [133], certain plankton population models are also described by excitable media [210]. In the FitzHugh–Nagumo model [133] of excitable media, the activator follows a bistable reaction as discussed above, but the slowly increasing concentration of the inhibitor shifts it out of the excited state. The inhibitor concentration grows proportionally to the difference between the number of activators and the number of inhibitors. The functions

$$f_1 = c_1(c_0 - c_1)(c_1 - 1), \quad f_2 = \epsilon(c_1 - \gamma c_2) \tag{126}$$

define the full reaction with typical parameter values [144] $\alpha = 0.25$, $\gamma = 3$, $\epsilon = 10^{-3}$. An interesting finding [144] for such a reaction is that, with localized initial perturbations above the threshold c_0 in open flows, it reaches a steady state over a broad range of Damköhler numbers, $Da_{\rm c} < Da < Da'_{\rm c}$. Both the onset and the disappearance of the steady state happens with a sudden jump of the average concentrations. The transition at $Da_{\rm c}$ is the usual emptying transition, which is due to the fact that the reaction is too slow to compensate the effect of outflow. The one at $Da'_{\rm c}$ is explained in terms of a structural change within the Lagrangian filament slice model [70]: the middle part of the filament carries very low concentrations, and the material is accumulating along the two edges of the filament. In certain flow geometries [67], the value $Da'_{\rm c}$ might formally be infinite implying that a steady state exists for $Da > Da_{\rm c}$. As long as the concentration is approximately constant over the filaments and a steady-state sets in, the situation is similar to the one described in Section 4 for both C_1 and C_2. It is rather remarkable that an open flow is *capable of stabilizing* the excited state on a fractal, in spite of the fact that this state is metastable both in a homogeneous environment and in closed flows [144]. Fig. 41 illustrates this same kind of

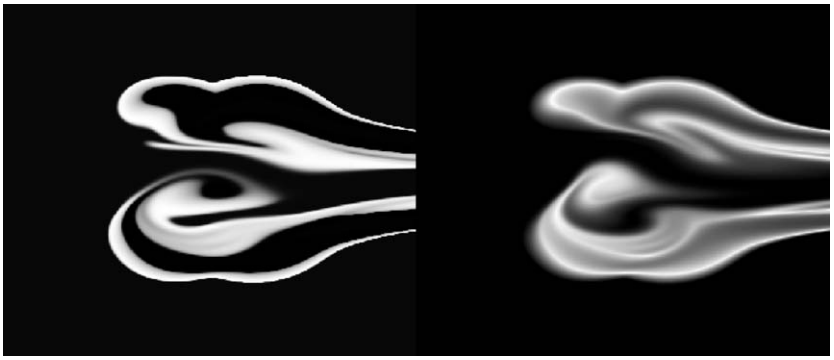

Fig. 41. Distribution of phytoplankton (left) and zooplankton (right) in a predator–prey model of plankton population dynamics living in an open chaotic flow (from left to right). Light gray corresponds to high concentrations. Picture by E. Hernández-García and C. López with their kind permission.

stabilization with a plankton model of excitable character in an open flow [67]. The plankton dynamics is of predator–prey type modelling zooplankton–phytoplankton interaction, and the flow represents an oceanic jet which is perturbed in a region by a localized wave, the mixing region of the open flow.

10.2. Flames

A combustion model more realistic then the one described by the FKPP equation (see Section 4) has been studied in Refs. [89,90]. The combustion reaction is the decay

$$C \to P \tag{127}$$

of fuel C of concentration c into a product P which does not play any further role in the dynamics. The reaction is exothermic: it produces a fixed amount of heat q per amount of reacted material. The decay rate is proportional to the concentration c, with a reaction rate $k(T)$ which depends on the temperature T according to an Arrhenius law. Additionally, there is an ignition temperature T_I below which no burning can take place:

$$k(T) = k \exp\left(-\frac{E}{k_B T}\right) \quad \text{for } T > T_I \ , \tag{128}$$

and $k(T) = 0$ for $T < T_I$. Here k is an overall decay rate, E is the constant activation energy, and k_B denotes the Boltzmann constant. This time dependence and the presence of a heat source produces a nonlinear coupling between the concentration c and the temperature field T.

The advection–diffusion-reaction equation for c is of the form of Eq. (123) with $c_1 \equiv c$, and $c_2 \equiv T$ and

$$f_1 = -kc \ \exp\left(-\frac{E}{k_B T}\right) \ . \tag{129}$$

The second equation follows from the heat balance. The thermal energy can be expressed as $\varrho c_p T$, where ϱ and c_p denote the density and the specific heat at constant pressure, respectively. Thus, we obtain a

temperature equation

$$\frac{\partial T}{\partial t} + (\mathbf{v}\cdot\nabla)T = \frac{qk(T)}{\varrho c_p}c + D_{\rm heat}\nabla^2 T \ . \tag{130}$$

Because the heat diffusion coefficient $D_{\rm heat}$ is in general different from the fuel's diffusion coefficient, a basic new dimensionless parameter appears as the ratio of them, the Lewis number:

$$Le = \frac{D_{\rm heat}}{D_{\rm diff}} \ . \tag{131}$$

Due to the temperature dependence, the reaction produces a kind of front propagation. As the filamentary slice model shows [89], the temperature tends to accumulate along filaments of finite width and this is accompanied by a local decrease of the fuel concentration there. Combustion can lead to a steady state in open flows [90] where the flame is concentrated along the unstable manifold, similar to the case of the FKPP equation. An emptying transition is present, i.e., slow reactions characterized by low Damköhler numbers (37) die out, and the combustion is quenched. At a critical $Da_{\rm c}$, however, combustion starts suddenly (with a jump in the steady-state temperature), and in the full range $Da > Da_{\rm c}$ steady combustion takes place on a filamentary pattern. In this range, Eq. (47) is expected to hold for the area occupied by the flame, or for the integrated excess temperature in the observational regime, along with the properties described in Section 4. A new feature is the dependence of the critical Damköhler number $Da_{\rm c}$ on the Lewis number. $Da_{\rm c}$ increases with Le [90]. This implies that an increase in the heat diffusivity (increasing Le) leads to quenching of the flame: fast heat conduction is not advantageous for maintaining controlled burning.

10.3. Population dynamics of competing species

We now re-examine in more detail the problem of coexistence of biological populations in open flows, already discussed in Section 5. As the simplest model of competition, we take two species competing for the same resource A. The interaction of the two species B_1 and B_2 is limited to the competition for resource A, and it is assumed that they do not influence each other otherwise. An autocatalytic process models the reproduction of each species B_1 and B_2:

$$A + B_1 \to 2\,B_1, \quad A + B_2 \to 2\,B_2 \ . \tag{132}$$

The species are advected by a flow, which we consider to be open. After some (short) time, we find bands of species along the filaments of the unstable manifold. These stripes contain several narrow subbands, whose *total* width is denoted by δ_1 and δ_2 for species B_1 and B_2, respectively (see Fig. 42).

The time evolution of these widths can be written as

$$\dot{\delta}_i = -\overline{\lambda}\delta_i + 2v_i p_i, \quad i = 1, 2 \ , \tag{133}$$

with v_i denoting the corresponding 'reaction rates' of the two species, which are related to their reproductive rates. Because the species can be assumed to be distributed among the subbands in a random manner, due to the chaos in the advection dynamics, we introduce here the probability p_i of finding a subband of species B_i on the edge of a typical filament of total width $\delta_1 + \delta_2$. This probability typically depends on the distribution of the species inside the filament. In case of complete, homogeneous mixing of the

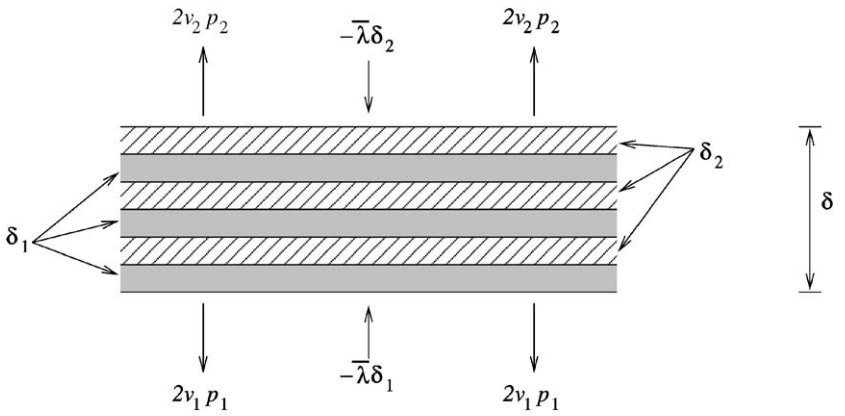

Fig. 42. Schematic diagram of the band structure in a competition model.

species inside the stripes, the probability would be proportional to the relative weight: $p_i = \delta_i/(\delta_1 + \delta_2)$. In general, this is not the case, and the p_i depend on the band widths δ_i in a non-trivial way. Simple dimensional reasoning suggests that p_i depends on δ_1/δ_2 in addition to the parameters of the flow and of the activity.

Summing up (133) for $i = 1, 2$ we arrive at Eq. (41) with $\delta = \delta_1 + \delta_2$ and

$$v \equiv p_1 v_1 + p_2 v_2 \tag{134}$$

as the average spreading velocity. Since there is no fractal scaling below the total bandwidth $\delta_1 + \delta_2$, the number of species B_i in the observation region is proportional to δ_i: $B_i/(B_1 + B_2) = \delta_i/(\delta_1 + \delta_2)$, with the consequence that the probabilities p_i are functions of the ratio B_1/B_2. Beyond the total width $\delta = \delta_1 + \delta_2$, the distribution is, however, fractal, and the total number $B = B_1 + B_2$ fulfills Eqs. (44) and (45). So the total number follows Eq. (47) with v as defined by Eq. (134). This results in the following population dynamical equation for species B_i [181]:

$$\dot{B}_i = -\kappa B_i - q(D-1)\frac{v}{L}B^{-\beta-1}B_i, + q\frac{v_i}{L}B^{-\beta}p_i\left(\frac{B_1}{B_2}\right), \quad i = 1, 2\ . \tag{135}$$

Here q is given by Eq. (48). By summing the equations for $i = 1$ and 2, we obtain

$$\dot{B} = -\kappa B - q\kappa\frac{v}{\overline{\lambda}L}B^{-\beta}\ , \tag{136}$$

which means that the total number of individuals follows exactly the autocatalytic rate equation (47) but with the weighted average velocity (134) of the competitors. For the number of each species, (135) gives a coupled, nonlinear set of population dynamical equations, containing production terms with non-trivial scaling given by fractal-dimension-dependent exponents.

In (135) the actual form of $p_i(B_1/B_2)$ is still undetermined. However, its form is well defined at steady state. Taking the ratio $v_1p_1/(v_2p_2)$ as expressed by (135) for $i = 1$ and 2, respectively, in the steady state $\dot{B}_1 = \dot{B}_2 = 0$ we find that $v_1p_1/(v_2p_2) = B_1^*/B_2^*$, with B_i^* being the steady-state values. Using $p_2 = 1 - p_1$,

this implies

$$p_1 = \frac{B_1^*/B_2^*}{v_1/v_2 + B_1^*/B_2^*} \ . \tag{137}$$

The above expression for p_1 in the steady state, together with simple dimensional reasoning and symmetry arguments, suggests that the choice

$$p_1(B_1/B_2) = \frac{(B_1/B_2)^\alpha}{(B_1/B_2)^\alpha + \omega}, \quad p_2 = 1 - p_1 \tag{138}$$

is a realistic one for the general form of p_1 and p_2. This has been confirmed by numerical evidence [181], which showed that ω is close to $(v_1/v_2)^\alpha$, with the coefficient α depending on the details of both the flow and the competition.

With choice (138) for p_i, a stability analysis of the fixed point was carried out in [181], showing that the non-trivial, coexistence fixed point is stable for $0 < \alpha < 1$. This finding was also supported by numerical evidence. This means that *coexistence can be generated by the chaotic advection dynamics of open flows*.

10.4. Collisional reactions

We consider the reaction scheme wherein the collision of two 'molecules' generates a new one, different from the previous two:

$$\mathrm{A} + \mathrm{B} \to \mathrm{C} \ . \tag{139}$$

In contrast to the autocatalytic process, a source of both components A and B is needed for the reaction to go on indefinitely. We assume that A is homogeneously distributed in the flow, and component B is injected uniformly at a certain location with a constant injection rate Φ_B.

On the level of individual particle modeling, we assume that particles A and B possess a reaction range σ_0 within which they are able to convert themselves and their partners into C particles. After a certain crossover time, B particles are expected to lie in bands of average width δ_B around the unstable manifold. As a consequence of the reaction, on both sides of this B-band, C-bands of typical width δ_C are expected to be present (see Fig. 43).

As long as this width is smaller than the reaction range σ_0, on both sides of the band, new C particles can appear, i.e., the C, band widens while the B band shrinks. Let v_{coll} denote the velocity of this process. The equations of the bandwidths can then be written as

$$\dot{\delta}_B = -\bar{\lambda}\delta_B - 2v_{\mathrm{coll}} + q_0(\delta_B), \quad \dot{\delta}_C = -\bar{\lambda}\delta_C + 2v_{\mathrm{coll}} \ . \tag{140}$$

Here q_0 is a source term which might depend on the actual B-width, since the inflow rate of B particles is constant only on the global level, and this requires a local width dependence, as discussed in Section 4.4.9. For $\delta = \delta_B + 2\delta_C$, Eq. (140) is equivalent to Eq. (41), if the front velocity is taken as

$$v = v_{\mathrm{coll}} + \tfrac{1}{2}q_0(\delta_B) \ . \tag{141}$$

Hence Eq. (41) describes the dynamics of the total width in this type of reaction as well.

There is no fractal scaling below δ, thus the number of B and C particles in the region of observation are proportional to δ_B and δ_C, respectively. Introducing

$$X = B + 2C \tag{142}$$

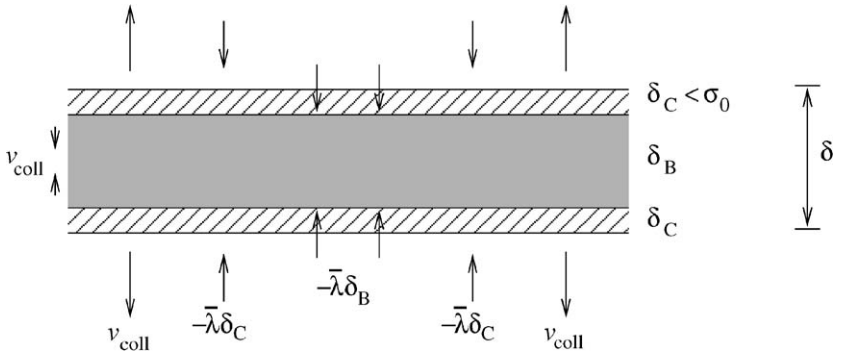

Fig. 43. Schematic diagram of the bands along the unstable manifold for collisional reactions.

as the total number of B and C particles, it fulfills (44) and (45) in place of B, since beyond δ the distribution is fractal. Putting all this together, we get

$$\dot{B} = -\kappa B - q(D-1)\frac{q_0(\delta_B) + 2v_{\text{coll}}}{2L} B X^{-\beta-1} + q\frac{q_0(\delta_B) - 2v_{\text{coll}}}{2L} X^{-\beta} ,$$
$$\dot{C} = -\kappa C - q(D-1)\frac{q_0(\delta_B) + 2v_{\text{coll}}}{2L} C X^{-\beta-1} + q\frac{v_{\text{coll}}}{L} X^{-\beta} . \tag{143}$$

The value of $q_0(\delta_B)$ is determined by requiring that $\dot{B} = -\kappa B + \Phi_B$ in case of $v_{\text{coll}} = 0$ (no reaction). From this condition, we get the following expression for $q_0(\delta_B)$:

$$q_0(\delta_B) = \frac{2\Phi_B L}{q}\frac{X^{\beta+1}}{(1-D)B + X} . \tag{144}$$

After substitution into (143), the reaction equations for the collisional reactions become

$$\dot{B} = -\kappa B + q\frac{v_{\text{coll}}}{L}\left[(1-D)\frac{B}{X} - 1\right] X^{-\beta} + \Phi_B ,$$
$$\dot{C} = -\kappa C + q\frac{v_{\text{coll}}}{L}\left[(1-D)\frac{C}{X} + 1\right] X^{-\beta} - \frac{(D-1)C}{(1-D)B + X}\Phi_B , \tag{145}$$

where the coefficient q and the exponent β are given again by (48) and (49), respectively. These reaction equations above are strongly coupled and nonlinear.

From (142) and (145), we can get a time-evolution equation for X. We recover Eq. (69) with X in place of B, and with v given by the effective reaction rate (141). Note that in this case v is not constant any longer, it depends on q_0, which in turn depends on B and C, and also on the injection rate Φ_B.

11. Reactions in closed flows

Flows in containers, or in finite domains subjected to periodic boundary conditions, are called closed, because particles cannot escape. Advected particles typically return close to their initial positions within a few natural time units of the flow. In this section, we show that certain aspects of the reaction dynamics

of closed flows can be understood with concepts taken from the open case, such as, e.g., fractal sets and fractal dimensions.

11.1. *Effective rate equation during the transicence towards a homogeneous state*

Reactions in such flows have completely different characteristics from those taking place in open flows. In the absence of fluid transport barriers, autocatalytic and bistable reactions, reactions in excitable media or flames [143,144] all lead to a steady state in which the full fluid domain is either occupied by the product or no product is present at all. The asymptotic state is thus homogeneous, and hence much less interesting than in the open case. This is fully consistent with the observation that product is distributed along the unstable manifolds. In closed flows the unstable filamentation is dense over the full domain. However, from localized initial particle distributions, the *transient* behavior before reaching a homogeneous steady state typically exhibits filamentary product distributions. Based on [80], we propose here to describe this behavior by means of a *time-dependent effective dimension*, $D_{\mathrm{eff}}(t)$. We emphasize that there is no invariant set in the system whose dimension would be $D_{\mathrm{eff}}(t)$. Nevertheless, this concept turns out to be useful since it allows a treatment analogous to that used in the open case.

We consider two-dimensional flows, in a square domain of linear size L, and the autocatalytic reaction A+B $\rightarrow$ 2B. A basic observation is that the length $\mathscr{L}$ of a line segment in a chaotic flow grows, over long times, exponentially: $\mathscr{L}(t) \sim \exp(ht)$, where h is the *topological entropy* of the advection dynamics [146,78,6,52,53]. Its value is typically somewhat larger than the average Lyapunov exponent $\bar{\lambda}$. For the sake of simplicity we assume in what follows that the topological entropy and the Lyapunov exponent coincide.

The increase in length of a material line *of finite width* is exponential only as long as it is short; later, saturation sets in. Therefore we write the equation of the length dynamics as

$$\dot{\mathscr{L}} = \bar{\lambda}\mathscr{L}\left(1 - \frac{\mathscr{L}}{\mathscr{L}^*}\right) , \tag{146}$$

because it is the simplest equation that has both an initial exponential growth and a saturation. Since we expect the filament width in the steady state to be δ^* given by Eq. (42), the saturation length is the total area divided by this width:

$$\mathscr{L}^* = \frac{L^2}{\delta^*} . \tag{147}$$

In the transient state, however, $\delta(t)$ evolves in time according to Eq. (41). The width is typically much shorter, while $\mathscr{L}(t)$ is much longer than the linear size L. We can thus *define* an instantaneous effective dimension via the relation[5]

$$\mathscr{L}(t) = \delta(t)\left(\frac{\delta(t)}{L}\right)^{-D_{\mathrm{eff}}(t)} . \tag{148}$$

[5] Note that in this definition no Hausdorff volume appears.

By taking the time derivative of this and using (146), we obtain an equation for the effective dimension as

$$\dot{D}_{\rm eff}\ln\frac{\delta}{L}=\bar{\lambda}\left[\left(\frac{\delta(t)}{\delta^*}\right)^{1-D_{\rm eff}}\left(\frac{L}{\delta^*}\right)^{D_{\rm eff}-2}-1\right]+(1-D_{\rm eff})\frac{\dot{\delta}}{\delta} \tag{149}$$

which is a non-autonomous differential equation.

Based on the effective dimension's time dependence, we turn now to the particle number dynamics. The number of boxes of size δ/L covering the B-distribution, according to (148), is $(\delta/L)^{-D_{\rm eff}}$. The area is then $\delta^2(\delta/L)^{-D_{\rm eff}}$, and the particle number B is obtained as

$$B(t)=c_0\delta^2(t)\left(\frac{\delta(t)}{L}\right)^{-D_{\rm eff}(t)}, \tag{150}$$

where c_0 is the reciprocal of the volume occupied by one particle. The time derivative of the above expression is

$$\dot{B}=B(2-D_{\rm eff})\frac{\dot{\delta}}{\delta}+\dot{D}_{\rm eff}B\ln\frac{L}{\delta}\ . \tag{151}$$

Using (149), and expressing δ by B via (150) yields the equation for B as

$$\dot{B}=\frac{2v}{L}(c_0L^2-B)\left(\frac{B}{c_0L^2}\right)^{-\beta(t)} \tag{152}$$

with

$$\beta(t)\equiv\frac{D_{\rm eff}(t)-1}{2-D_{\rm eff}(t)}\ . \tag{153}$$

It is interesting to observe that a singular term of power $-\beta(t)$ is present in (152), but now it *depends on time*.

Further insight can be gained by working out explicit asymptotic forms. From Eq. (41), we know that after an initial time t_1 which is a few times $1/\bar{\lambda}$, the bandwidth is close to its steady state, $\delta\approx\delta^*$. After time t_1, the last term in (149) becomes exponentially small, and the equation simplifies to

$$\dot{D}_{\rm eff}\ln\frac{\delta^*}{L}=\bar{\lambda}\left[\left(\frac{L}{\delta^*}\right)^{D_{\rm eff}-2}-1\right], \tag{154}$$

where $\delta^*/L=2v/(\bar{\lambda}L)$. Note that $D_{\rm eff}(t)$ converges towards 2 as $t\to\infty$. The precise solution of (154) with an initial effective dimension value $D_{\rm eff}(t_1)$ at time t_1 is

$$D_{\rm eff}(t)=2-\frac{\ln[1-(1-(L/\delta^*)^{2-D_{\rm eff}(t_1)})\mathrm{e}^{-\bar{\lambda}(t-t_1)}]}{\ln[L/\delta^*]}\ . \tag{155}$$

For $t\gg t_1$, a Taylor expansion can be applied to leading order. This shows an exponential convergence of the effective dimension to 2:

$$D_{\rm eff}(t)\approx 2-\frac{\mathrm{e}^{-\bar{\lambda}(t-t_1)}[(L/\delta^*)^{2-D_{\rm eff}(t_1)}-1]}{\ln(L/\delta^*)}\ . \tag{156}$$

By rewriting the B-equation (151) as

$$\dot{B} = \left(-\bar{\lambda}B + q(t)\frac{v}{L}B^{-\beta(t)}\right) + B\bar{\lambda}\left(1 - \frac{2v}{\bar{\lambda}L}\left(\frac{B}{c_0L^2}\right)^{-\beta(t)}\right) , \tag{157}$$

where $q(t) \equiv 2(c_0L^2)^{1/(2-D_{\rm eff}(t))}$, we see that the first term on the right-hand side is similar to the reaction equation (47) valid in open flows. After time t_1, the first term on the right-hand side of (151) becomes negligible ($\dot{\delta} \approx 0$). For times $t > t_1$, the B-dynamics is therefore governed by

$$\dot{B} = B\bar{\lambda}\left(1 - \frac{2v}{\bar{\lambda}L}\left(\frac{B}{c_0L^2}\right)^{-\beta(t)}\right) . \tag{158}$$

Using (150) with δ^* in place of δ simplifies (158) to

$$\dot{B} = B\bar{\lambda}\left(1 - \frac{B}{c_0L^2}\right) . \tag{159}$$

This equation is essentially different from that valid in open flows. A long-term solution can only exist if $B(t)$ converges to c_0L^2, $\beta(t)$ diverges, but $(B/c_0L^2)^{-(\beta+1)}$ remains finite.

Eq. (159) can be solved explicitly. The initial condition is that the particle number at t_1 is $B(t_1)$. For $t \gg t_1$ this reads as

$$B(t) = c_0L^2\left(1 - \left[\frac{c_0L^2}{B(t_1)} - 1\right]e^{-\bar{\lambda}(t-t_1)}\right) . \tag{160}$$

By relating $B(t_1)$ to the fractal dimension $D_{\rm eff}(t_1)$ via (150), we find the equivalent form

$$B(t) = c_0L^2\left(1 - \left[\left(\frac{2v}{\bar{\lambda}L}\right)^{D_{\rm eff}(t_1)-2} - 1\right]e^{-\bar{\lambda}(t-t_1)}\right) . \tag{161}$$

The asymptotic homogeneous product distribution is thus reached via a purely exponential decay, determined by the Lyapunov exponent, and does not depend on the instantaneous effective dimension at all. The treatment presented here is a leading order approximation only. A more careful extension of this theory would be desirable, eventually in the spirit of [199,48].

11.2. Roughness exponents and multifractal chemical measures

As we have seen, in closed flows passive advection spreads any dye droplet over the entire fluid surface (in other words, the unstable filamentation is space filling). In the case of a reaction taking place in the fluid, this means that the support of the asymptotic product distribution is two dimensional. An interesting recent discovery shows, however, that the distribution is not always smooth: it might become 'rough' [139]. The class of active processes which has been shown to display this behavior is that of *decaying* reactions in the presence of time-independent *sources*, whose distribution is assumed to be smooth. For simplicity, we consider here the case of a linear decay, represented symbolically by

$$A \to 0 . \tag{162}$$

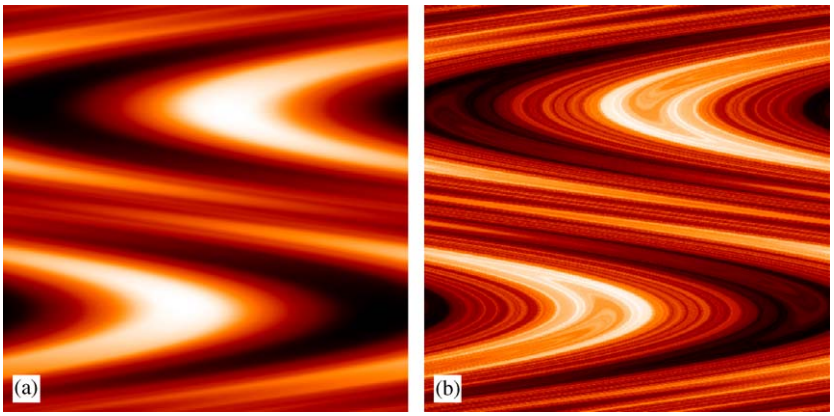

Fig. 44. Steady concentration distribution of a linearly decaying substance A under a closed, time-periodic chaotic flow (in the shear flow model by Pierrehumbert [159]) in a smooth (a) and a filamental (b) phase. The region shown is the unit square of the fluid's (x, y) plane and the source term is proportional to $1 + \sin(2\pi x)\sin(2\pi y)$. The average Lyapunov exponent of the passive advection dynamics is $\bar{\lambda} = 2.7$ over a period of the flow, and the chemical decay rate is (a) $k = 4.6$, and (b) $k = 1.4$. The Damköhler number is thus $Da = k/\bar{\lambda} = 1.70$ in (a) and $Da = 0.52$ in (b), respectively, in harmony with (166). Picture by Izabella Benczik with her kind permission.

For a given flow, at certain parameters a *smooth-filamental transition* [139,141] can take place as illustrated by Fig. 44. In the filamental case the concentration contours are striated, they run parallel to the unstable foliation of the advection dynamics. Certain filaments are much more densely populated than others. Roughness is present perpendicular to the unstable direction, and corresponds to sharp fluctuations of the concentration, which are present on all scales. Mathematically, the concentration field cannot be approximated by a Taylor series in directions transversal to the unstable manifold, even for arbitrarily small scales. In the limit of weak diffusion, the distribution becomes non-differentiable along the stable foliation. It is worth noting that the basic features might remain valid in the presence of non-differentiable source distributions as well [68].

This phenomenon can be understood as a result of a competition between chemical dynamics, which tends to homogenize the concentration throughout the container, and chaotic advection, which tends to generate inhomogeneities in the concentration due to the processes of stretching and folding. If the chemical time scale is slow enough, filaments of high concentration persist for arbitrarily long times aligned with the unstable foliation. This regime is called the *filamental phase*. If the decay of the chemical dynamics is, however, faster than the dispersion of trajectories caused by advection, irregularities of the chemical field decrease and finally a smooth distribution is obtained. This is called the *smooth phase*.

In the filamental phase, the chemical concentration appears to be higher on certain filaments than on others. These filaments form a subset of the whole unstable filamentation, which is space filling in closed flows. The effect of the reaction can therefore be considered to be similar to that of opening up a reaction free flow, since this also selects a subset of the original filamentation (via selecting the never escaping orbits in the opened up flow, and their unstable manifolds). Insight may be gained into this process by the so-called 'leaking' method of flows, which corresponds to defining an artificial escape region within a closed flow, and studying the dynamics of the resulting open system, for which all the properties mentioned in Section 2 apply. By this method, a fractal subset of the closed flow's filamentation

is selected. A qualitative similarity between the fractal pattern of the leaked reaction-free flow, and that of the reactive case in the original closed flow has been demonstrated [183,184,211,185,176].

To learn in more detail about how reactivity selects a fractal pattern, we consider the balance between the inhomogenizing effects of the chaotic flow and the homogenizing effect of the decaying reaction. This can be expressed again by means of a bandwidth equation, to a first approximation at least. Since decaying reactions do not produce fronts, the bandwidth equation (41) reduces to

$$\dot{\delta} = -\overline{\lambda}\delta \ , \tag{163}$$

where δ is a typical bandwidth along the unstable filamentation, in the limit of negligible diffusion. A local fluctuation a in the concentration of A decreases with a chemical decay rate k as

$$\dot{a} = -ka \ . \tag{164}$$

The *local concentration gradient* γ is on the order of a/δ. From the two previous equations, the dynamics of the gradient is given by

$$\dot{\gamma} = (\overline{\lambda} - k)\gamma \ . \tag{165}$$

This clearly shows that an instability occurs: local gradient fluctuations die out for fast reactions, but they *grow* if the reaction is slowly decaying. Thus we recover the result of [139,141,68,17,18] for the condition of the existence of a filamental phase: $k < \overline{\lambda}$. By means of the Damköhler number Da (37), the condition for the filamental phase is

$$Da < Da_{\mathrm{c}} \ , \tag{166}$$

and the critical value is found to be $Da_{\mathrm{c}} = 1$.

In a more systematic approach, the roughness is better characterized by structure functions, because the concentration distribution is a self-affine function [30,139,141,69,4,109]. For a steady chemical concentration $a(\mathbf{r})$, the structure functions are defined as

$$S_q(\delta\mathbf{r}) = \langle |a(\mathbf{r} + \delta\mathbf{r}) - a(\mathbf{r})|^q \rangle \sim |\delta\mathbf{r}|^{\zeta_q} \ , \tag{167}$$

where the average denoted by $\langle\rangle$ is taken over different spatial regions. The scaling is valid above the diffusive scale δ^*_{diff} (see Section 4.4.8), and the *roughness exponents* ζ_q do not depend on the diffusion coefficient D_{diff}. The condition for a filamental case is the non-differentiability of the concentration, i.e., $\zeta_q < q$.

In general, ζ_q is a nonlinear function of q (see Fig. 45). Its form is determined by the distribution of the local Lyapunov exponents of the flow.

In the case when the probability distribution $P(\lambda)$ of the local Lyapunov exponents λ is Gaussian, i.e. when

$$P(\lambda) \sim \mathrm{e}^{-G(\lambda)t} \tag{168}$$

and

$$G(\lambda) = \frac{(\lambda - \overline{\lambda})^2}{2\Delta} \ , \tag{169}$$

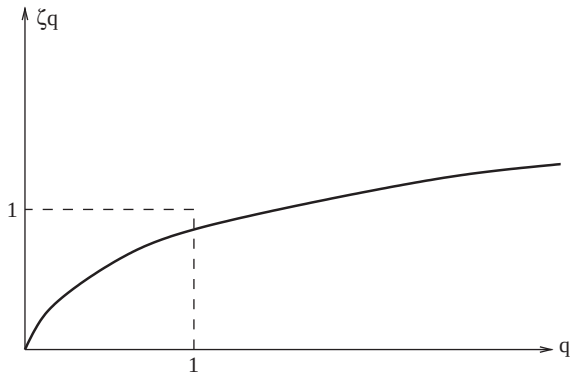

Fig. 45. Schematic diagram of the roughness exponent spectrum in the filamental phase.

a powerful explicit form can be derived in the filamental phase [30,141]:

$$\zeta_q(b) = \sqrt{\left(\frac{\overline{\lambda}}{\Delta}\right)^2 + \frac{2qk}{\Delta}} - \frac{\overline{\lambda}}{\Delta} = \frac{\overline{\lambda}}{\Delta}\left(\sqrt{1 + 2qDa\frac{\Delta}{\overline{\lambda}}} - 1\right) . \tag{170}$$

The theory based on the structure functions thus contains contributions due to fluctuation of the local Lyapunov exponent. When all the Lyapunov exponents are the same ($\Delta = 0$), $\zeta_q = qk/\overline{\lambda} = qDa$.

It has recently been pointed out [19] that, based on the concentration gradients, a *chemical measure* can be defined which is a (multi)fractal distribution, and can be characterized in terms of generalized dimensions. This chemical measure is

$$\overline{\mu}_i(\varepsilon) = \frac{\int_{x_i}^{x_i+\varepsilon} |\partial a/\partial x| \, \mathrm{d}x}{\int |\partial a/\partial x| \, \mathrm{d}x} , \tag{171}$$

based on the absolute value of concentration gradients. Due to the denominator, this is normalized, and can be considered as a probability measure. Its generalized dimensions D_q are the exponents satisfying [60]

$$\sum_i \overline{\mu}_i(\varepsilon)^q \sim \varepsilon^{(D_q-1)(q-1)} , \tag{172}$$

which can be expressed [19] by the roughness exponents ζ_q as

$$D_q(k) = 1 + \frac{q(1-\zeta_1(k)) - 1 + \zeta_q(k)}{q-1} . \tag{173}$$

A similar relation has been derived between the structure function exponent and the generalized dimension of the velocity fluctuations in fully developed 3D turbulence [212], and of a diffusively decaying passive tracer in quasi-geostrophic turbulence [198]. In our case the dimension depends on the reaction rate k. The chemical reaction itself produces the fractality and selects its dimension.

It follows from (173) that the information dimension D_1 is given by

$$D_1(k) = 2 - \left(\zeta_1(k) - \left. \frac{\mathrm{d}\zeta_q(k)}{\mathrm{d}q} \right|_{q=1} \right) . \tag{174}$$

This clearly shows that except the case of a trivial roughness exponent spectrum ($\zeta_q = q\zeta_1$), the information dimension differs from 2. Since the slope of ζ_q around $q = 1$ is typically smaller then ζ_1 itself, the information dimension is smaller then 2. For weakly fluctuating Lyapunov exponents $\Delta/\bar{\lambda} \ll 1$, the information dimension can be written in view of (170) in the filamental case as

$$D_1(Da) = 2 - Da^2 \frac{\Delta}{2\bar{\lambda}} < 1 . \tag{175}$$

This equation shows that the dominant chemical gradients of the decaying reaction sit on a fractal of dimension less than that of the flow, and the filamentary phase of decaying reactions in closed flows thus shares certain similarities to frontal reactions in open flows.

11.3. Synchronization in oscillatory and other time-dependent reactions

Oscillatory reactions [98,187] exhibiting exactly time-periodic behavior in well-stirred containers form an important class of nonlinear kinetics. Notable examples are the Belousov–Zhabotinsky reaction [228,44] and metabolic oscillations in cell suspensions [72]. For oscillatory reactions taking place in closed chaotic flows, a novel question arises, just like in systems of coupled oscillators [160], whether the whole system can behave uniformly, whether synchronization can take place.

In a medium at rest, the reactive oscillations at different points of macroscopic distances L are very weakly coupled since the time scale L^2/D_{diff} of the diffusive transport is much longer than the period of oscillations. Synchronized oscillations over the whole domain can thus not occur, the only coherent behavior is therefore in the form of propagating waves [98,187].

The presence of a flow might, however, increase effective coupling, and it is thus expected that sufficiently strong stirring leads to spatially uniform chemical distributions, i.e., to full synchronization. It has been pointed out in [145] that imperfect, chaotic mixing is sufficient to produce efficient synchronization even in the presence of inherent inhomogeneities of the chemical process when exactly uniform concentrations are unattainable.

Neufeld et al. [145] show that a relevant parameter is the stirring rate, which is proportional to the Lyapunov exponent of the passive advection problem, and is, for periodic flows, inversely proportional to the period of the flow. The increase of the stirring rate strengthens the coupling among the local oscillations, and above a critical value synchronization sets in. First this is rather weak, but the degree of synchronization gradually increases with the stirring rate.

In a synchronized state (strong stirring) the concentrations are nearly homogeneous and change periodically in time. Therefore, a snapshot of the concentration field practically does not exhibit any small scale patterns.

In an unsynchronized state (weak stirring) filamental distributions are found along the unstable foliation of the reaction free flow, and the pattern is changing with time. The snapshots corresponding to different times are statistically equivalent, the average spatial concentration of any chemical component is nearly constant in time. For reactions without any frontal properties, the chemical scale coincides with the diffusive scale (cf. Section 4.4.8 and Eq. (63)), and the width of the filaments is proportional to this width.

The stirring rate can be made dimensionless by multiplying its reciprocal with some chemical rate (the reciprocal of a characteristic reaction time). In terms of this Damköhler number *Da*, synchronization is present for values smaller than a critical Da_c, and filaments can be seen in the unsynchronized state, i.e., for

$$Da > Da_c \ . \tag{176}$$

This condition is formally the opposite to the case of smooth-filamental transitions (Section 11.2) since in that case slow reactions, fast stirring maintain filamental patterns in the presence of chemical sources, while now the same condition leads to synchronization and the lack of pronounced filamentarity.

A somewhat related phenomenon has been observed [230] in excitable media (cf. Section 10.1) where some parameters change randomly in space and time. When this noise is weak and the stirring rate is fixed, the flow washes out the effect of the noise-induced excitation centers and the system remains in its unexcited state. For larger noise, however, local excitations develop into filaments and ultimately fill the whole domain. Later the system starts to relax synchronously back to the unexcited state, and the process repeats in time. Thus, noise induces a coherent global excitation and noise sustained oscillations. At even stronger noise intensities, not all points relax simultaneously, and synchronization might become totally destroyed. Excited and unexcited states are then localized to nearby filamental regions along the unstable manifold at any instant of time. These noncoherent patterns are persistent: they change in time but are statistically equivalent. The scenario at fixed noise level is the following: at slow stirring persistent filamental patterns are present (cf. Eq. (176)). The fast stirred, synchronized regime splits into two subregions. Global excitation are maintained at intermediate stirring rates. The system remains globally unexcited at very strong stirring. These findings might be relevant also in the context of oceanic plankton blooms.

12. Discrete-time modeling

So far, we have considered reactions as time-continuous processes, with the reactants continuously distributed. However, as already mentioned in Section 3, we can also model reactions as kinetic processes, where the reactants are considered as interacting particles, which react at discrete times. This gives rise to a quite different kind of modeling, where the reactive process is described by maps, instead of differential equations. This discrete-time reactive dynamics is the topic of this section. We will see that the results of previous sections are recovered in suitable limits, but there will also be some new phenomena that are found only in the discrete regime. Discrete modeling may be important for population biology, since in this case the continuum approximation can be too coarse grained.

12.1. Basic theory of the discrete autocatalytic reaction

In this part, we discuss the discrete-time theory of the autocatalytic reaction [209,83], in periodic two-dimensional incompressible open flows. The reaction is supposed to take place at instants separated by a constant time interval τ, the *reaction time lag*. It is assumed, for simplicity, that all particles react at the same time, according to the 'infection' scheme described in Section 3 (the requirement of simultaneous reaction is relaxed below, in Section 12.5).

Let $\mathscr{A}_B(t) \equiv \mathscr{A}_B^{(n)}(s)$ denote the area occupied by reagent B at time t. Here $s \in [0, \tau]$ is the time after the nth reaction. Thus the total physical time is $t = n\tau + s$. During the time interval of length τ only the contraction of the chaotic flow controls the number of B-particles. After the B-particles have become distributed in narrow bands around the unstable manifold, in a fixed region of observation, $\mathscr{A}_B^{(n)}(s)$ decreases with to the escape rate κ of the chaotic saddle according to

$$\mathscr{A}_B^{(n)}(\tau) = \mathscr{A}_B^{(n)}(0)\mathrm{e}^{-\nu} \tag{177}$$

with $\nu \equiv \kappa\tau$.

We recall that the fractal unstable manifold is *fattened up* with material B. Let $\delta(t) \equiv \delta^{(n)}(s)$ denote the *average* width of the stripes at time $t = n\tau + s$. At any reaction, there is a sudden increase of the filament width [see Fig. 21b and c] by an amount of 2σ.

$$\delta^{(n+1)}(0) = \delta^{(n)}(\tau) + 2\sigma \ . \tag{178}$$

For convenience, we choose the period of the flow (taken to be the time unit) to be a multiple or a divisor of the time lag: $m\tau = 1$, where m or $1/m$ is an integer, respectively. Whichever of the two options is taken depends on the time lag itself. For time lags shorter than the flow's period ($\tau < 1$), the period contains an integer number of reactions, otherwise ($\tau > 1$) the time lag is an integer multiple of the period. This way we ensure that a periodic behavior with the period of the flow appears as a fixed point or as a periodic cycle (and not as a quasiperiodic motion) on the stroboscopic map taken at the instants of the reaction.

It is worth noting that although the dimension of the unstable manifold is independent of the instant at which the snapshot is taken, the Hausdorff volume $\mathscr{H}$ is not. Since the flow is periodic, $\mathscr{H}$ is periodic with the period of the flow. Thus the Hausdorff volume $\mathscr{H}^{(n-1)}(\tau) = \mathscr{H}^{(n)}(0) \equiv \mathscr{H}^{(n)}$ at the instant of reactions is m or $1/m$ periodic as a function of n.

Since $\delta^{(n)}(s)$ is the smallest box size with which the fractality of the reagent can be measured, the area $\mathscr{A}_B^{(n)}(s)$ of B can be written at any time as (cf. (44))

$$\mathscr{A}_B^{(n)}(s) = \mathscr{H}^{(n)}(s)L^D[\delta^{(n)}(s)]^{2-D} \ . \tag{179}$$

From (177) and (179), the area $\mathscr{A}_B^{(n)}(\tau)$ before the $(n+1)$th reaction can be written as

$$\mathscr{A}_B^{(n)}(\tau) = \mathscr{H}^{(n)}\mathrm{e}^{-\nu}L^D[\delta^{(n)}(0)]^{2-D} \ . \tag{180}$$

From (179), the average bandwidth $\delta^{(n+1)}(0) \equiv \delta^{(n+1)}$ right after reaction $(n+1)$ expressed in terms of $\delta^{(n)}$ right after the nth reaction is given by:

$$\delta^{(n+1)} = \left[\frac{\mathrm{e}^{-\nu}\mathscr{H}^{(n)}}{\mathscr{H}^{(n+1)}}\right]^{1/(2-D)} \delta^{(n)} + 2\sigma \ . \tag{181}$$

This is the discrete-time bandwidth dynamics. Note that in the limit $\tau \to 0$, $\sigma = v\tau$, $\mathscr{H}^{(n)} \to \mathscr{H}(t)$, $\delta^{(n)} \to \delta(t)$, it goes over, in view of (6), into (39).

Eq. (179) implies the following mapping for the B-area $\mathscr{A}_B^{(n+1)}(0) \equiv \mathscr{A}_B^{(n+1)}$ taken right after the reactions:

$$\mathscr{A}_B^{(n+1)} = \{[\mathrm{e}^{-v}\mathscr{A}_B^{(n)}]^{1/(2-D)} + g^{(n)}\sigma\}^{2-D} , \tag{182}$$

where $g^{(n)} = 2(\mathscr{H}^{(n+1)}L^D)^{1/(2-D)}$ is a geometric factor.

Eqs. (181) and (182) belong to the same class of maps as recursion relations of the type $x_{n+1} = f(x_n)$. They are one-dimensional and strongly dissipative, and therefore they describe the convergence towards attractors.

If $\mathscr{H}^{(n)} \equiv \mathscr{H}$ and $g^{(n)} \equiv g$ are constants, a fixed point of the system is found from $\mathscr{A}_B^* = \mathscr{A}_B^{(n+1)} = \mathscr{A}_B^{(n)}$ in the form of

$$\mathscr{A}_B^*(\tau) \equiv \mathscr{H}\delta^{*(2-D)} = \left(\frac{\mathrm{e}^{\bar{\lambda}\tau}\sigma g}{\mathrm{e}^{\bar{\lambda}\tau} - 1}\right)^{2-D} , \tag{183}$$

where (6) has been used again. This is the area occupied by reagent B just after a chemical reaction takes place, in the steady state. The area of B right before a reaction is a factor e^v smaller.

In the more general case when $\mathscr{H}^{(n)}$, and thus $g^{(n)}$, are periodic, the attractor is a limit cycle of the same period. The active process becomes thus synchronized to the underlying flow dynamics. Due to the linearity of Eq. (181), and the fact that $\mathrm{e}^{-v/(2-D)} < 1$, the limit cycle attractor of (182) is always stable.

We now take the continuous time limit $\tau \to 0$, $\sigma \to 0$ of Eq. (182), so that we can compare the results of this section with those of Section 4. Before doing so, it is worth rewriting reaction equation (182) in a different form. If the coverage of the manifold by B is relatively wide, i.e., $\delta^{(n)} \gg g^{(n)}\sigma$, we can expand the right-hand side of (182) to first order to obtain

$$\mathscr{A}_B^{(n+1)} = \mathscr{A}_B^{(n)}\mathrm{e}^{-v} + \sigma g^{(n)}(2-D)[\mathrm{e}^{-v}\mathscr{A}_B^{(n)}]^{-\beta} , \tag{184}$$

where β is given by Eq. (49). In the continuous time limit, $\tau \to 0$, $\sigma = v\tau$, $\mathscr{A}_B^{(n)} \to \mathscr{A}_B(t)$, $g^{(n)} \to g(t)$, the differential equation obtained for the B area is the analog of the *singular* map (184):

$$\dot{\mathscr{A}}_B = -\kappa\mathscr{A}_B + g(t)(2-D)v\mathscr{A}_B^{-\beta} . \tag{185}$$

Using relation (6) and the fact that the area $\mathscr{A}_B$ is proportional to the number of particles B (cf. (45)), we see that this expression is identical to Eq. (47).

12.2. Emptying transition

In the discrete model, the finite size of the reaction range σ leads to an *emptying transition* for large time lags. If during the advection part of the dynamics, of duration τ, the number of escaping particles exceeds the number of new B particles created at the next reaction step, then the balance favors the total extinction of material B. This happens at a *critical* value for the dimensionless reaction-time, v_{crit} .

We derive an expression for v_{crit} via defining the *productivity* of the reaction. The productivity of the chemical reaction in the steady state can be characterized by the ratio of newly born to parent particles B as

$$S = [\mathscr{A}_B^*(0) - \mathscr{A}_B^*(\tau)]/\mathscr{A}_B^*(\tau) = \mathrm{e}^v - 1 . \tag{186}$$

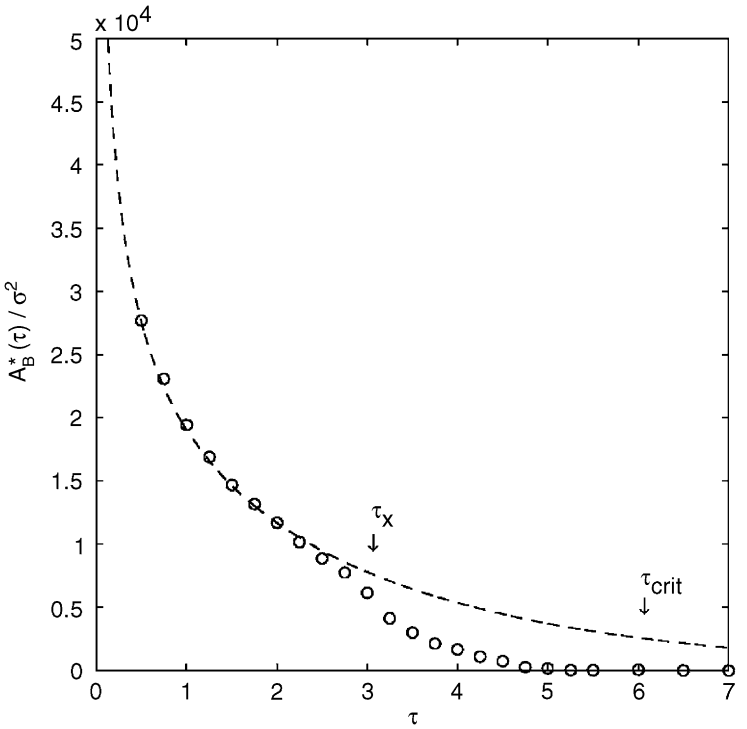

Fig. 46. Dependence of the number $\mathscr{A}_B^*(\tau)/\sigma^2$ of B particles just before reaction at steady state on the time lag τ (all other parameters are as in Fig. 18), with the exception of the reaction range which is $\sigma = \varepsilon_0 = 0.003$. Note the sudden decrease around $\tau_\times \approx 3$ ($v_\times \approx 1.1$), leading to a complete disappearance of B from the mixing region, indicating an emptying transition, around $\tau_{\text{crit}} = 6.1$.

The productivity S, however, cannot be arbitrarily large. An absolute maximum $S_{\max}$ exists, since the number of cells inside the reaction range σ is *limited*. This implies that $e^v - 1 \leqslant S_{\max}$. For v smaller than $v_{\text{crit}} = \ln(1 + S_{\max})$ the productivity of the chemical reaction grows exponentially with increasing reaction time τ or v. For $v > v_{\text{crit}}$, however, S does not grow further. Using Eq. (186) and the fact that $S \leqslant S_{\max}$, we have $\mathscr{A}_B^*(0) \leqslant (1 + S_{\max})\ \mathscr{A}_B^*(\tau)$. Inserting expression (177), this leads to $\mathscr{A}_B^*(0) \leqslant (1 + S_{\max})\mathscr{A}_B^*(0)e^{-v}$. If the quantity $(1 + S_{\max})e^{-v}$ is less than 1, this inequality can only hold for $\mathscr{A}_B^*(0) = 0$. Thus, for $v > v_{\text{crit}}$, the area of reagent B quickly drops to zero, and only the background material A remains in the system in the steady state. In our case $S_{\max} = 8$, the critical reaction time lag thus becomes $\tau_{\text{crit}} = 2\ln 3/\kappa$. In the case of the numerical experiments detailed in Section 4.1, $\kappa = 0.36$ and so $\tau_{\text{crit}} = 6.1$. Indeed, this is confirmed by Fig. 46.[6]

The definition of productivity leads us to another important time value, the *crossover time lag*, $v_\times$. This represents a threshold time lag for which the effects of finite particle size (and grid) come into play. Below this value, the filaments are 'tightly' covered by the B cells, so on average one particle is responsible for *at most two* newborns, $S = 2$. At $v_\times$, the coverage of the filaments is just about to break up, thus:

[6] In the terms used in the continuous theory (Section 4), a 'microscopic Damköhler number' Da can be defined as $Da = \tau^{-1}/\bar{\lambda} = (2 - D)/v$. The critical value of Da, below which the emptying transition occurs, is thus $Da_c = (2 - D)/\ln(1 + S_{\max})$.

$v_\times = \ln(1+S) = \ln 3$, which leads to $\tau_\times = \ln 3/\kappa = \tau_{\rm crit}/2 = 3.05$. For values of τ larger than $\tau_\times$, the theory based on the existence of well-defined bands, described in the previous paragraph, breaks down since it does not make use of the finite particle size. Indeed, a deviation from (183) shows up in Fig. 46 by $\tau = 3$.

12.3. Discrete population dynamics

In Section 10.3 the population dynamics of competing species was formulated in a *continuous* manner. For certain species, however, a discrete modeling is better, and so it is also included here. In this approach, we say that reproduction happens after reaction time lag τ, during which time only the advection modifies the number of particles via outflow from the region of observation.

As in Section 10.3, the competing species are modeled by the autocatalytic processes $A + B_1 \to 2\,B_1$, $A + B_2 \to 2\,B_2$. Species B_1 and B_2 are then competing for the same resource A. These species, besides their autocatalytic activity, are advected by a flow. It is expected that after some short time, they will be distributed along the filaments of the unstable manifold. In fact, both species taken together cover the unstable manifold in bands of total width $\delta^{(n)}(s)$ at time $t = n\tau + s$, time s after the nth reproduction event. It is expected that the species cover sub-bands of total width $\delta_i^{(n)}(s)$, $i = 1, 2$, where $\delta_1^{(n)}(s) + \delta_2^{(n)}(s) = \delta^{(n)}(s)$ (cf. Fig. 42). Just like in the continuous case, it is assumed that the species have a probability p_i, $i = 1, 2$, to be on the edge of the filament, and hence to be able to reproduce.

At the instant of reproduction, the partial stripe widths change as

$$\delta_i^{(n+1)}(0) = \delta_i^{(n)}(\tau) + 2\sigma_i p_i, \quad i = 1, 2\ . \tag{187}$$

That is, the reproduction occurs only where B_i is on the edge (with probability p_i), and there the front can advance by σ_i. Summing up this equation for $i = 1$ and 2, Eq. (178) is obtained with $\sigma = p_1\sigma_1 + p_2\sigma_2$.

Regarding B_1 and B_2 together as B, the total amount of competitors, Eq. (182) holds, again, with $\sigma = p_1\sigma_1 + p_2\sigma_2$.

For the species, we find no fractality below the scale corresponding to the total bandwidth $\delta^{(n)}(s)$. This means that the area occupied by each of the species is proportional to their partial bandwidth $\delta_i^{(n)}(s)$, leading to

$$\mathscr{A}_{B_i}^{(n)}(s) = \mathscr{A}_{B}^{(n)}(s)\frac{\delta_i^{(n)}(s)}{\delta^{(n)}(s)}\ . \tag{188}$$

Using Eqs. (179) and (187), Eq. (188) implies that the area $\mathscr{A}_{B_i}^{(n+1)}(0) \equiv \mathscr{A}_{B_i}^{(n+1)}$ covered by B_i right after reproduction $(n+1)$ becomes

$$\mathscr{A}_{B_i}^{(n+1)}[\mathscr{A}_{B}^{(n+1)}]^\beta = \mathrm{e}^{-\bar\lambda\tau}\mathscr{A}_{B_i}^{(n)}[\mathscr{A}_{B}^{(n)}]^\beta + g^{(n)}p_i\sigma_i \tag{189}$$

with $i = 1, 2$, where $\bar\lambda = \kappa/(2-D)$ from Eq. (6), and $g^{(n)} = 2[\mathscr{K}^{(n+1)}(0)L^D]^{1/(2-D)}$. This is a strongly coupled set of population dynamical equations for the competition of the two species. In the knowledge of the areas covered by B_i after reaction n, (189) determines them after reaction $n+1$. The discrete-population dynamical equations thus define a mapping of population numbers at discrete-time intervals [181].

The discrete-time approach transforms into the continuous description of Section 10.3 in the limit $\sigma_i \to 0$, $\tau \to 0$, but with $v_i = \sigma_i/\tau$ remaining finite. It is easy to show that (189) then turns into (135).

12.4. Coalescence of particles

In this subsection, the case of *coalescence* is studied [148,149], given symbolically by

$$\mathrm{B}+\mathrm{B} \to \mathrm{B}\ .$$

In words, if two advected particles come too close to each other, one of them disappears ('dies'), and the other one survives. The study of this kind of activity is motivated, among others, by population dynamics. In crowded populations, when the local density exceeds a critical value, the mortality rate of individuals increases due to the fact that the niches they occupy (food, necessary chemicals, light) have only a finite capacity. Namely, if the distance between two individuals becomes closer than a given reaction range σ, one of them dies on an average time scale τ, the average reaction lag. The reaction range σ also represents a crowding threshold for the active population, which limits their density.

To illustrate the finite-size effects on the advective coalescence problem, we choose again to use the cellular flow given by Eq. (120). The activity, given by the coalescence process $\mathrm{B}+\mathrm{B} \to \mathrm{B}$, is implemented in the following way [148]. On a grid of size $\varepsilon = \sigma$, we choose a set of boxes that covers the chaotic attractor and then put a particle at the center of each box. There are a total of $N(\sigma)$ boxes covering the attractor. We evolve forward in time each particle in the system for some fixed time τ (which is measured in units of T), and put the particle in the box at the end point of the trajectory. If two or more particles end up in the same box, the first one to arrive remains in it, and the others are removed from the system. We then repeat this procedure to obtain the time evolution of the coalescence process. For simplicity, we choose $\sigma = 5 \times 10^{-3}$ to be the crowding threshold.

In the simulations, we monitor the number density of the particles, defined as $n(t) = \mathcal{N}(t)/N_0$, where $\mathcal{N}(t)$ is the total number of particles at time t in the $N_0 = N(\sigma)$ boxes covering the attractor. From the results of the simulations, we find that in all cases the asymptotic temporal behavior is given (approximately) by $n(t) \sim t^{-1}$.

We argue that this type of behavior, in the limit of slow reaction (large τ), is, in fact, a consequence of the universality of the coalescence reaction kinetics. In order to see this, we first recall that the natural invariant measure of a σ-sized box is the probability for the trajectory to visit that box. Based on that, on a statistical level, we may approximate the dynamics of the flow by a stochastic process consisting of simply shuffling the particles among the boxes covering the attractor, according to the probability given by the natural measure of the chaotic dynamics. Let $p_1, p_2, \ldots, p_N$ be the natural measure of each particular σ box covering the attractor (the natural measure is normalized, $\sum_{i=1}^{N} p_i = 1$). The shuffling step is defined as follows: take the image of the set of $N(t)$ particles such that the image of a certain particle is in box i with probability p_i. After each shuffling, coalescence is imposed in every box containing two or more particles. If we focus on one step of this stochastic process (shuffling + coalescence), we may ask the following question: what is the expected number of boxes that are not empty after one step of the stochastic process, if at the beginning of the step we had m particles in m different boxes? Using techniques of combinatorial analysis, we can follow this reasoning to find an evolution equation for the number density $n(t)$. The details can be found in [148,149]. Here we just write the

final result:

$$\frac{\mathrm{d}n}{\mathrm{d}t} = -En^2 \ , \tag{190}$$

where the constant E is given by

$$E = \frac{N}{2}\sum_{i=1}^{N} p_i^2 \ . \tag{191}$$

Without loss of generality, we may put $n(0) = 1$, and then the solution of Eq. (190) is found to be

$$n(t) = (Et + 1)^{-1} \ . \tag{192}$$

Thus, for long times we get $n(t) \sim t^{-1}$, as in the simulations. From the definition of the generalized dimensions D_q [55], it is found that the constant E can be written as

$$E \sim \sigma^{D_2 - D_0} \ , \tag{193}$$

where D_0 is the familiar fractal dimension, and D_2 is the *correlation dimension* [55].

The decay law for the number $\mathcal{N}(t)$ of particles is thus for long times

$$\mathcal{N}(t) \sim \sigma^{-D_2} t^{-1} \ . \tag{194}$$

The main results of this theory, as given by Eq. (194), are thus: (i) the temporal behavior is universal and independent of the particularities of the chaotic flow, and (ii) the surviving particles are distributed selectively on a subset of dimension D_2 (which is usually close to D_1 and D_0) on the attractor at a given instant of time.

12.5. Phase-active autocatalytic particles

We have so far assumed that all particles undergo the reaction at integer multiples of the time lag τ, *all at the same time*. This is a rather restrictive condition. It would be more realistic to assume some random distribution among the particles of the times in which the reaction takes place, whilst preserving that for each individual particle the reaction occurs with the same time lag τ. In other words, each particle is associated with a *phase*, which determines when it will undergo reaction. The effect of phase in the reaction dynamics was studied in Ref. [177]. Here we present only the most important results and their consequences.

It is assumed that there is a finite number N_θ of phases a particle can have. More precisely, each reacting particle advected by the flow is labelled by an integer index θ, with $0 \leqslant \theta \leqslant N_\theta - 1$. All particles with index θ undergo reaction at instants $t = n\tau + (\tau/N_\theta)\theta$. The case $N_\theta = 1$ corresponds to the previously studied situation of simultaneous reaction by all particles. As in the previous models, we also consider the space to be discretized by a grid of size ϵ, which we take for simplicity to be equal to the reaction range σ. We consider again the autocatalytic reaction, in which the 8 unoccupied neighboring cells are filled with copies of the particle undergoing reaction. The 'daughter' particles are created with the same phase θ as their 'mother'.

The first question is whether the fractal character of the spatial distribution of particles is preserved in this generalized dynamics. Based on numerical simulations, the answer is yes [177]: the area covered by

all the particles (irrespective of their phase) scales with σ as σ^{2-D}, where D is the fractal dimension of the chaotic saddle's unstable manifold associated with the flow. In other words, even with different particles reacting at different times, the total distribution behaves as in the single-phase case ($N_\theta = 1$).

Another relevant question in this context is whether there is some kind of *phase selection* in the equilibrium state (reached after some initial transient time). In other words, does one phase dominate the other one, so that most of the particles in equilibrium have a single phase? Or, on the contrary, do several phases appear in more or less the same proportion? The answer turns out to depend on the reaction time τ. The simplest non-trivial case is that of two phases, $N_\theta = 2$. This system has been found to display *phase coexistence* for sufficiently fast reactions, that is, for τ below a critical value $\tau_c \approx 3$. For $\tau < \tau_c$, the distribution always evolves to a $\frac{1}{2} - \frac{1}{2}$ proportion of particles of either phase, independently of the initial conditions. This happens even if initially there was a higher proportion of particles of a given phase. For $\tau > \tau_c$, however, one of the phases will dominate, occupying typically about 5 times the area of the unfavored phase. In certain cases, one of the phases may even be completely extinguished, leaving only the other one. Which one of the phases is favored depends on the initial distribution of particles. The critical value $\tau_c \approx 3$ corresponds to the value above which the equilibrium distribution ceases to be continuous, and develops 'gaps', as shown in Section 12.2. We can thus say that for $\tau > \tau_c$, there is a kind of *spontaneous symmetry breaking* in the system, with the equilibrium distribution displaying less symmetry than the dynamical laws themselves. Values of τ greater than about $2\tau_c$ correspond to the emptying transition (Section 12.2), for which the equilibrium distribution contains no particles of either kind.

It may be tempting to draw a parallel between phase coexistence and the phenomenon of species coexistence treated in Sections 5 and 12.3. In the case of species coexistence, the different kinds of particle have distinct reaction parameters (such as the rate of reproduction, for example). In contrast, phase coexistence (or phase selection) occurs with *identical* particles. As a consequence, no particular phase is preferred by the dynamics. Although the phenomenon of phase coexistence is intrinsically discrete, and is thus bound to the individual particle modeling, in the continuous limit ($\sigma, \tau \to 0$, $\sigma/\tau \to v$), different phases correspond to different 'colors' of otherwise identical particles. We therefore expect Eqs. (135) and (138) to hold.

12.6. Discrete reaction dynamics in 3D flows

We now study the discrete reaction dynamics corresponding to the theory of three-dimensional active flows, presented in its continuous version in Section 6.2. Reactions are implemented by a discretization of space, in a straightforward generalization to three dimensions of the procedure explained in Section 12.1. Here we also assume τ to be either an integer m (the reaction takes place after m periods), or to take values of the form $1/m$ (the reaction takes place m times in each period). In the actual numerical simulation of the reaction, we take advantage of the symmetries and of the uniform contraction and expansion factors of the 3D baker map M, introduced in Section 6.1, to improve numerical efficiency.

The bandwidth dynamics turns out to be the same as (181) but the unstable manifold's dimension is denoted (as in Section 6) by D_u. For the volume $\mathscr{V}_B^{(n)}$ occupied by B particles right after the reactions we then obtain the map

$$\mathscr{V}_B^{(n+1)} = \{[e^{-v}\mathscr{V}_B^{(n)}]^{1/(3-D_u)} + \sigma g^{(n)}\}^{3-D_u} , \tag{195}$$

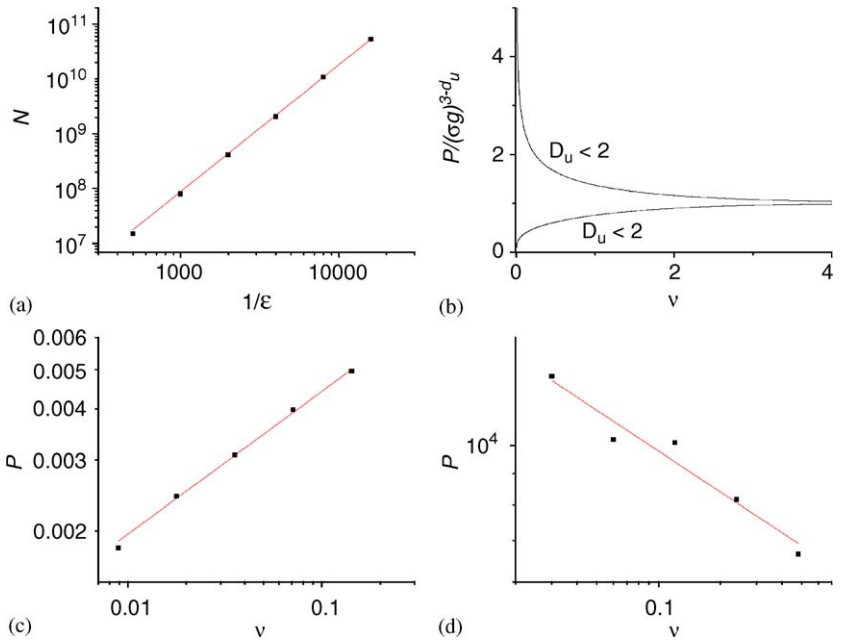

Fig. 47. (a) Number N of occupied cells in the steady-state distribution of the autocatalytic reaction as a function of the inverse of the grid size ε, for $\Lambda = 0.35$; from the slope we get a dimension $D_u = 2.31 \pm 0.01$, which agrees with the theoretical value $D_u = 2.32$. Agreement is also found with other values of Λ we examined. (b) Plot of the ν-dependent part of the theoretical production P, from Eq. (197), for $D = 0.15$ (upper curve) and $D = 0.35$ (lower curve). (c) Production obtained from simulation, as a function of ν, for $\Lambda = 0.35$, that is, for $D_u > 2$; the slope gives $P \sim \nu^{0.35\pm0.02}$, which compares well with the theoretical value 0.32 of the coefficient, from Eqs. (73) and (198). (d) Same as (c), with $\Lambda = 0.15$ and $D_u = 1.73 < 2$; the slope gives a power-law with a coefficient -0.23 ± 0.04, which is close to the theoretical value of -0.27. The great spread in the data is due to the fact that for small Λ the steady-state distribution has few occupied cells.

with $g^{(n)} = 2(\mathscr{H}^{(n)} L^{D_u})^{1/(3-D_u)}$, and $\nu = \kappa\tau$. By assuming the Hausdorff volume to be time independent, we find the steady-state value of $\mathscr{V}_B$:

$$\mathscr{V}_B^* = \left[\frac{e^{\nu/(3-D_u)}\sigma g}{e^{\nu/(3-D_u)} - 1}\right]^{3-D_u} . \tag{196}$$

From Eq. (196) we see that $\mathscr{V}_B^*$ scales with σ as σ^{3-D_u}. To verify this prediction, we simulate the advection-reaction dynamics of the 3D baker map M introduced in Section 6.1. Fig. 47a shows $\mathscr{V}_B^*$ as a function of σ for two values of the parameter Λ of the baker map. The power law predicted by Eq. (196) is confirmed in both cases: the dimension found by fitting is consistent with that given by (73). This confirms the fact that the reacting particles indeed cover the unstable manifold.

We turn our attention to the production P, defined as the amount of reactants produced at each reaction step, which in a steady state is equal to the amount that escapes. In analogy with (186) one finds that the production is $P = (1 - e^{-\nu})\mathscr{V}_B^*$. Substituting from Eq. (196), we have

$$P = \frac{e^{\nu} - 1}{[e^{\nu/(3-D_u)} - 1]^{3-D_u}} (\sigma g)^{3-D_u} . \tag{197}$$

In Fig. 47b, the dependence of P on v is plotted for both $D_u < 2$ and $D_u > 2$. For $v \ll 1$, from the Taylor expansion of Eq. (197) we find that P scales as

$$P \sim v^{D_u-2} \sim \tau^{D_u-2} , \tag{198}$$

in harmony with (85).

We verified Eq. (198) through simulation, as is shown in Fig. 47c for $D_u > 2$, and in Fig. 47d for $D_u < 2$, respectively, where P is calculated for several values of v, for the 3D baker map. It is seen that for $D_u > 2$, P does go to zero as v decreases, and diverges for $D_u < 2$. Moreover, using Eq. (73), the power-law relation predicted by Eq. (198) is verified quantitatively, to within numerical error. There is thus an enhancement of the reaction's productivity as $v \to 0$, which is an exclusive three-dimensional phenomenon.

12.7. Inertial effects and transport barriers (non-hyperbolicity)

In this part, we investigate the effects of particle inertia on the reaction dynamics of flows with non-hyperbolic advection [130], such as those studied in Section 8. As we have seen in Section 9, the inertial effects manifest themselves as dissipation, so that the transition to finite inertia turns the original Hamiltonian advection dynamics into a dissipative dynamics.

It has been recently shown [129] that, while hyperbolic dynamics is robust, nonhyperbolic chaotic scattering typically undergoes a metamorphosis in the presence of arbitrarily small amount of dissipation. Dissipation may convert marginally stable periodic orbits of the KAM islands into attractors. The survival probability around the remnants of KAM tori then becomes exponential, the dimension of the chaotic saddle becomes less than the dimension of the phase-space, and the overall dynamics of the scattering process becomes hyperbolic.

In Section 8, we introduced the concept of effective dimension for non-hyperbolic flows. To understand the meaning of the effective dimension D_{eff} for fractal sets arising in the transition from Hamiltonian nonhyperbolic scattering to weakly dissipative chaotic scattering, we consider a Cantor set, which is constructed in the interval $[0, 1]$ according to the rule that in the nth time step, a fraction $\Delta_n = \gamma/(\xi+n)+h$ is removed from the middle of each one of the $N = 2^{n-1}$ remaining subintervals, where ξ, γ, and h are constants. The conservative case corresponds to $h = 0$, which is characterized by an algebraic decay with n of the total length remaining, given by $R(n) \sim n^{-\gamma}$ for $n \gg \xi$, and by a unit fractal dimension for the invariant set, $D = 1$ [103]. The removed fraction Δ_n decreases at each time step and, as a result, a systematic change of scales is induced, resulting in a non-self-similar invariant set that becomes denser as we go to smaller scales. The consequence is that the box-counting dimension D converges very slowly to 1 as the resolution $\varepsilon \to 0$, leading to a scale-dependent effective dimension (cf. Section 8)

$$D_{\text{eff}}(\varepsilon) \approx 1 - \gamma/\ln \varepsilon^{-1} , \tag{199}$$

for ε small enough.

The limiting dynamics changes drastically and acquires properties of hyperbolic dynamics when a small amount of dissipation is allowed, which is modeled by $0 < h \ll \gamma/\xi$. In particular, the total length of the remaining intervals decays exponentially, $R(n) \sim (1-h)^n$ for $n \gg \gamma/h - \xi$, and the dimension D of the invariant set becomes smaller than one:

$$D = \ln 2 \ln[2/(1-\delta)] . \tag{200}$$

For finite n, however, the transition from the conservative to the dissipative case is much smoother. For $\ln \varepsilon^{-1} \gg \xi$, the effective fractal dimension is

$$D_{\text{eff}}(\varepsilon) \approx \ln 2/\ln[2/(1-\delta)] - \gamma'/\ln \varepsilon^{-1} , \tag{201}$$

where $\gamma' \equiv \gamma/(1-h)$. The key feature is that unrealistically small scales are required to resolve the limiting values of the fractal dimension. For instance, to obtain $D_{\text{eff}} > 0.95$, scales $\varepsilon < 10^{-20}$ are required. Thus, for realistic scales, the physically important characteristic of the fractal set is the effective dimension D_{eff}. We emphasize that D_{eff} is different not only from the fractal dimension of the original non-hyperbolic system, but it also differs from that of the hyperbolic dynamics that results due to the introduction of inertia. This means that *scars* of the non-hyperbolic Hamiltonian dynamics are observable in the hyperbolic dynamics of dissipative systems.

Based on Section 8, the above discussion suggests that, if there are inertial autocatalytic particles in a 2D periodic flow, their steady state distribution seen with a resolution ε will cover an area $\mathscr{A}_B(\varepsilon)$ given by $\mathscr{A}_B(\varepsilon) \sim \varepsilon^{2-D_{\text{eff}}}$. In order to verify numerically this scaling law, we use a discrete-time map, representing the dynamics of a continuous time-periodic flow at multiples of the period. We use the idea of *embedding maps* [27] to incorporate dissipation. For an area preserving map $\mathbf{x}_{n+1} = \mathbf{M}(\mathbf{x}_n)$, representing the dynamics of a time-periodic incompressible fluid, a possible choice for the corresponding embedding map representing the *inertial* (dissipative) particle dynamics is $\mathbf{x}_{n+2} - \mathbf{M}(\mathbf{x}_{n+1}) = \mathrm{e}^{-a}\,(\alpha\mathbf{x}_{n+1} - \mathbf{M}(\mathbf{x}_n))$, where a and α are parameters. This can be written as

$$\mathbf{x}_{n+1} = \mathbf{M}(\mathbf{x}_n) + \mathbf{w}_n , \tag{202}$$

$$\mathbf{w}_{n+1} = \mathrm{e}^{-a}[\alpha\mathbf{x}_{n+1} - \mathbf{M}(\mathbf{x}_n)] , \tag{203}$$

where $\mathbf{x}$ and $\mathbf{w}$ can be interpreted as the configuration-space coordinates and the detachment from the fluid velocity, respectively, so that $(\mathbf{x}, \mathbf{w})$ represents the phase-space coordinates. The embedding map (203) embodies all the main features of the dynamics of a non-inertial particle in a 2D flow. In particular, it can be shown that the above map is uniformly dissipative, with phase-space contraction rate equal to e^{-2a}; that the noninertial dynamics $\mathbf{x}_{n+1} = \mathbf{M}(\mathbf{x}_n)$ is recovered in the limit $a \to \infty$; and that the configuration-space contraction rate is proportional to $\mathrm{e}^{-a}(\alpha - 1)$ for $\mathrm{e}^{-a}(\alpha - 1) \ll 1$. The range $\alpha < 1$ corresponds to the case where the particle is denser than the fluid (aerosols), whereas values of α greater than 1 represent particles less dense than the fluid (bubbles). Thus, the parameters a and α of map (203) are the discrete-time analogues of $1/St$ and R, respectively, of the continuous-time equation of motion for a non-inertial particle, Eq. (118). Next we consider such a dynamics for both $\alpha > 1$ and $\alpha < 1$.

To simulate the flow, we take as $\mathbf{M}$ map (112) of Section 8. We recall that the dynamics is nonhyperbolic for $\lambda < 6.5$. For $\lambda = 4$, for example, there is a major KAM island in the xy-space, as shown in Fig. 48a. Also, from Fig. 48a, one can see tangencies between the stable and unstable manifolds in the neighborhood of the KAM island, which is a signature of non-hyperbolicity. When this map is embedded in Eqs. (202), (203), for $\alpha > 1$, the (x, y)-projection of the resulting four-dimensional map is dissipative in the mixing region (original KAM islands and neighborhood). In this regime, the dissipation stabilizes marginally stable periodic orbits in the KAM islands of the conservative map, converting the KAM islands and their neighborhood into the corresponding basin of attraction of the newly created attractors, as shown in Fig. 48b. The basin itself extends around the mixing region mimicking the stable manifold of the conservative dynamics. As a result, the tangencies between the invariant manifolds apparently disappear, suggesting that the advection dynamics of bubble particles is *hyperbolic*. This hypothesis was also verified from the direct computation of D and κ. For $\alpha < 1$, on the other hand, the configuration-space projection expands

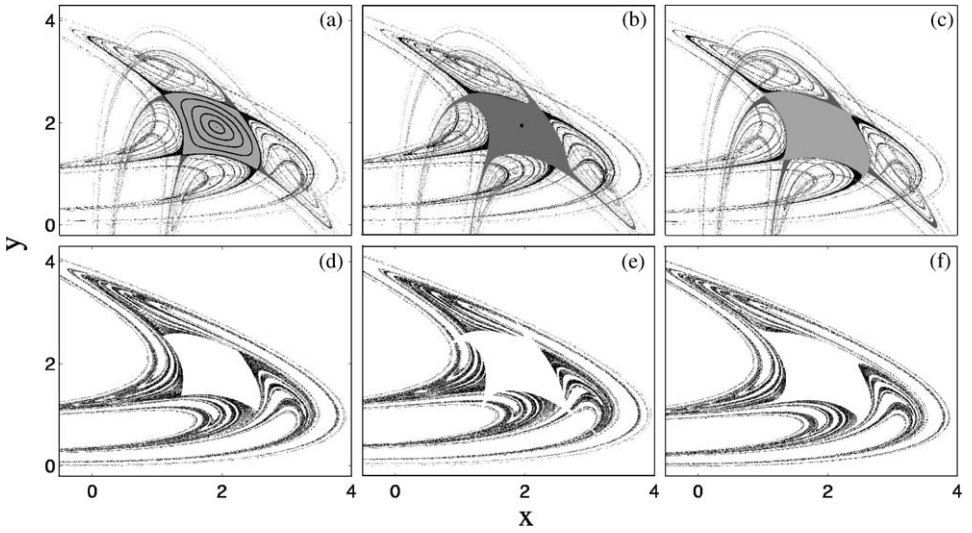

Fig. 48. (a) KAM island (light gray), and stable (gray) and unstable (black) manifolds for $a = \infty$. (b) Fixed point attractor (black dot), basin of attraction (gray), and unstable manifold (black), for $\alpha = 1.05$ and $a = 1$. (c) Stable (gray) and unstable (black) manifolds for $\alpha = 0.95$ and $a = 1$, outside the region covered by the almost trapped orbits (light gray). Particles are launched with initial velocity matching the fluid velocity ($\mathbf{w}_0 = \mathbf{0}$). (d–f) Respective area covered by B-particles in the "open" part of the flow right before the reaction, for $\tau = 5$ and $\sigma = 5 \times 10^{-3}$.

in the mixing region and almost all the orbits eventually escape to infinity. However, for small inertia and α close to 1, particles in the regions corresponding to KAM islands of the conservative dynamics and neighborhood are *almost trapped* in the sense that the time it takes to escape is much larger in these regions than outside them. These regions are neglected in our analysis of the open part of the flow, as shown in Fig. 48c, because filamentary structures cannot be resolved inside them.

To simulate the reaction dynamics, we follow the usual procedure of dividing the mixing region into a grid where the size of the cells represents the reaction range σ. We use the autocatalytic reaction as an example. By starting with a small seed of B-particles near the stable manifold, after a transient time a steady state is reached where B-particles are accumulated along a fattened-up copy of the unstable manifold, as shown in Fig. 48d for massless point particles, in Fig. 48e for bubbles, and in Fig. 48f for aerosols. To compute the effective fractal dimension D_{eff} of the unstable manifold, the uncertainty algorithm [57] has been applied. The effective dimension turns out to be constant over several orders of magnitude of variations in ε and it is approximately the same for both noninertial and slightly inertial bubble particles ($D_{\text{eff}} = 1.73$ for $\varepsilon > 10^{-15}$), while it is somewhat smaller for slightly inertial aerosol particles ($D_{\text{eff}} = 1.68$ for $\varepsilon > 10^{-15}$), as shown in Fig. 49. Strong evidence that the scaling of the area occupied by the particle distribution is determined by the effective dimension is presented in Fig. 50 for two different values of the time lag τ. This shows the scaling of the area covered by the B particles as a function of the resolution. The scaling exponent is consistent with $D_{\text{eff}} = 1.73$ for noninertial and bubble particles, and with $D_{\text{eff}} = 1.68$ for aerosol particles. Thus, the effective dimension D_{eff} plays exactly the same role as the fractal dimension for hyperbolic systems (see Section 4). We note that even though the area changes with the inertial properties of the particles, the *scaling* of the area remains essentially the same for bubbles, as expected from the Cantor-set model.

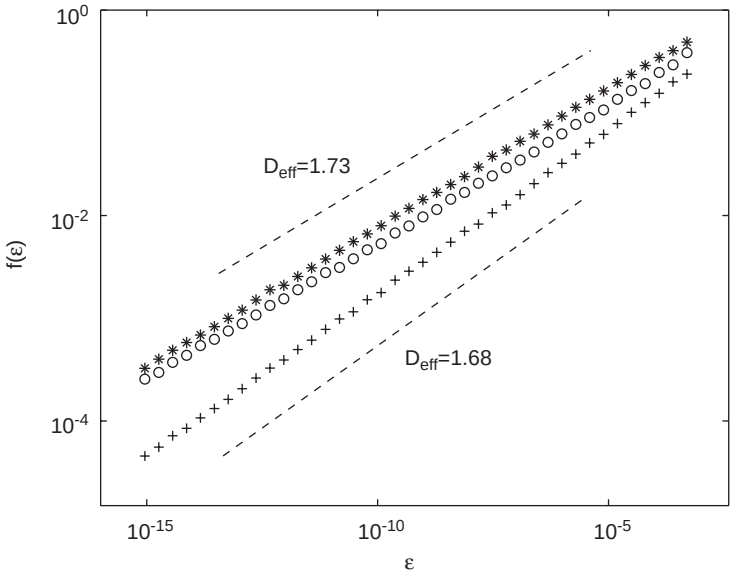

Fig. 49. Effective dimension of the unstable manifold as computed from the uncertainty method, where $f(\varepsilon)$ is the fraction of ε-uncertain points in the line $x = 0$, $0 < y < 0.1$ of the time reversed dynamics. The aerosol data are shifted vertically downward for clarity. Stars correspond to noninertial particles ($a = \infty$), circles to bubble particles with $\alpha = 1.05$ and $a = 1$, and plus signs to aerosol particles with $\alpha = 0.95$ and $a = 1$.

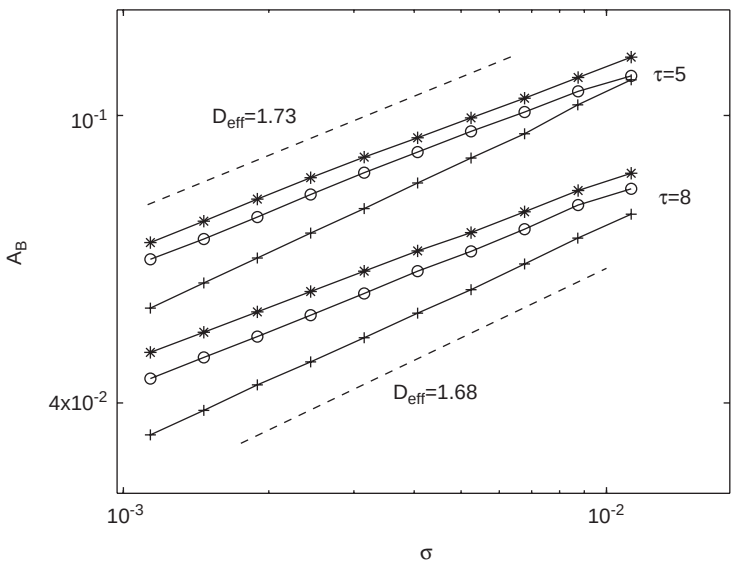

Fig. 50. Scaling of the relative area $\mathscr{A}_B$ covered by B-particles (in the region shown in Figs. 48(d)–(f), right before the reaction) as a function of the reaction range σ for two choices of the time lag τ. Stars correspond to noninertial particles ($a = \infty$), circles to bubble particles with $\alpha = 1.05$ and $a = 1$, and plus signs to aerosol particles with $\alpha = 0.95$ and $a = 1$.

13. Concluding remarks, perspectives

In this work we presented a dynamical system approach towards understanding the dynamics of reactivity in open chaotic flows. We have shown that to describe the reactive phenomenon, a Lagrangian view is particularly suitable. (An Eulerian approach, if it can be carried out at all, is expected to yield the same results, but the Lagrangian one provides, in any case, deeper insight.) It is the reaction-free advection dynamics which essentially determines the main features of the reactive dynamics. Therefore, dynamical system characteristics, like Lyapunov exponents, escape rates and fractal dimensions (of the unstable manifold) of the underlying chaotic advection enter the reactive theory. One of our basic goals has been to find rate equations. By concentrating on the *global* behavior of all the particles (i.e., the total material content) in a fixed region, we have derived rate equations which turned out to be of novel type. They contain singular production terms which arise as a result of the fractality of the advection dynamics. More precisely, on the right-hand side of the rate equations, there is a contribution P to the production which can be written as a power of some combination X of the material content of the substances playing a role in the reaction:

$$P \sim X^{-\beta} , \tag{204}$$

with $\beta > 0$ depending only on the fractal dimension.

The following types of reactions have been investigated:

- *autocatalytic reactions*, more generally, reactions spreading in the form of fronts (Sections 4, 10.1, 10.2, 11.1);
- *collisional reactions* (Section 10.4);
- *competitive dynamics* (Sections 5 and 10.3);
- *decaying dynamics* (Section 11.2);
- *oscillating reactions* (Section 11.3).

The appearance of the singular term (204) in the rate equation reflects the fact that the reaction takes place along the surface of a fattened up fractal whose effective surface tends to infinity by refining resolution, i.e., by decreasing material content.

We also investigated how the reaction outcome and the corresponding rate equation is modified by changing the following features of the flow (first three items) or of the advection dynamics (last two items):

- *open–closed character of the flow*: in the case of closed flows, the filamentary patterns are transient, leading to a new term in the rate equation (Section 11);
- *two-dimensional–three-dimensional flows*: the equations remained formally the same, but in 3D the singular term might become regular in certain cases (Section 6, see also Section 12.6);
- *periodic–aperiodic time dependence of the flows*: the singular production term remains in aperiodic flows, but the activity turns out to be enhanced by the randomness of the flow (Section 7);
- *flow without transport barriers* (*hyperbolic*)*–with transport barriers* (*non-hyperbolic*): effective fractal dimensions cause the singular enhancement of production in the nonhyperbolic case (Section 8, see also Section 12.7);

- *point-like–finite size particles advected in flows*: although the advection becomes dissipative when the particles are of finite size, and attractors replace the chaotic saddle, the singular enhancement remains, depending on the dimension of the attractors' projection onto the configuration space (Section 9, see also Section 12.7).

The dimensionality and the open or closed character of the flow is found to have the strongest influence, which may change the structure of the rate equations. The other factors do not change the structure of the rate equation, only the prefactors and the actual value of exponent β depend on the details. In this sense the singular behavior is *universal*. Although not all possible combinations of flows and reactions have been investigated, the main features are expected to hold in general. To verify this, the investigation of reactions of other types is important, especially more complex and realistic reaction dynamics. Examples of work in this direction include oscillating reactions [91], front propagation in cellular flows [1], and the investigation of chiral symmetry breaking [28] and boundary effects on reactions [31].

Which type of reaction is relevant might depend on the typical scale, and the problem to be solved. In the four main categories mentioned in the Introduction, the situation is the following:

- *Microfluidics*: In this field, the dynamical system approach to mixing is very natural since turbulence is not present. Several chaotic advection studies are available, but to our knowledge chemical reactions have been investigated in nonchaotic flows only. One problem to face with in chaotic cases is that in order to see enhancement, the reactive scale δ^* must be much below the channel width, i.e. should be of the order of a few micrometers. This can be achieved with sufficiently slow reactions (slow on the time scale of the prediction time). These studies might also be relevant for fluids with active particles in porous media, a problem of great environmental relevance. Here, again, very different scales are involved, since in clay it takes e.g. hours for a fluid to spread, whereas in sand and rocky soil this is much faster [26,75,175]. The effect of chaos on the reactions in soil has not yet been studied in detail either [215,65].
- *Laboratory scale*: At this scale, both turbulent mixing and chaotic advection may appear. Besides several theoretical works [125,209], a first experiment has already been carried out in a closed container [154]. It cleanly shows the enhancement of production, but without investigating the filamentary structures. Thus, more detailed experimental studies are necessary (cf. Note added in proofs). These might have applications ranging from cellular processes to epidemiology. Combustion experiments with chaotic flames are also challenges for the future.
- *Oceanic flows*: A dynamical system approach based on observational data has led to the identification of Lyapunov exponents in a real ocean current [4]. The same study indicates that the sea surface temperature can be identified as a decaying substance, and proves that it is rough in the sense of Section 11.2. In other approaches [3,142,107,118], the filamentary character of plankton patchiness is investigated. Longer observational data in this respect are desirable.
- *Atmospheric flows*: The filamentary nature of the atmospheric ozone has long been known [58,41], and a recent approach evaluates the (effective) fractal dimension underlying the chemical reactions [223]. More generally, atmospheric transport simulation codes have appeared [96,97] which are based on Lagrangian principles, and are therefore expected to provide more insight into the filamentary character of several reactions in the stratosphere [58].

This list also illustrates that the basic concepts of dynamical system theory (chaos, Lyapunov exponents, dimensions, etc.) have started to penetrate into sciences like microfluidics, oceanography or meteorology, and have helped properly describing relevant phenomena on different scales. It is therefore desirable for physicists to enter this interdisciplinary research, and to strengthen their efforts to learn more about environmental sciences for the mutual benefit of both fields.

Acknowledgements

This work was supported by the Hungarian Science Foundation (OTKA T047233, TS044839, F042476, T046646) and the MTA/OTKA/NSF Fund (Project No. Int. 526). AEM and CG were supported by FAPESP, and CG was additionally supported by CNPq. GK was supported by the Békésy and by the Bolyai grants. We thank the Max-Planck-Institut für Physik Komplexer Systeme, Dresden, Germany where some of the key ideas of this work were discussed. Useful discussions with H. Lustfeld, I. Mezić, R. Müller, Z. Neufeld, A. Pohlmeier, and I. Scheuring are acknowledged. Special thanks are due to I. Benczik, E. Hernández-Garcia, C. López, I. Mezić, and T. Nishikawa for allowing us the use of their unpublished pictures. We thank the authors of [9] and [58] (the publishers of Deep-Sea Research and J. Atmos. Sci.), and to NASA for the opportunity of using Figs. 5 and 11, and Figs. 4, 10, respectively.

Note added in proofs:

During the refereeing process of the paper, late 2004, we became aware of the work by Nugent et al. [151]. This is the first experimental paper devoted to a detailed investigation of the filamental chemical patterns in a chaotic flow. The authors investigate the Belousov–Zhabotinksy (BZ) reaction [228] in a flow corresponding to the blinking vortex model [7] generated via a magnetohydrodynamic technique. This is the closed version ($\xi = 0$) of the blinking vortex–sink system described in Section 2.2.2. The flow's only dimensionless parameter, the analog of η in (21), is kept constant in the experiments. As a characteristic parameter of the advection–diffusion process, a mixing time τ_m is defined. This is practically the time needed to reach the diffusive scale $\sqrt{D_{\rm diff}/\bar{\lambda}}$ (cf. Section 4.4.8) from a macroscopic scale L due to the exponential stretching/contraction of chaotic advection. In terms of our notation, this mixing time is $\tau_m = 1/(2\bar{\lambda}) \ln Pe$ where the Lagrangian Péclet number (38) is evaluated with the center-to-center vortex spacing as L. With the typical value of the diffusion coefficient for the chemicals in the BZ reaction, the Péclet number is on the order of 10^4. Since the average Lyapunov exponent $\bar{\lambda}$ is inversely proportional to the time period T of the flow, τ_m is practically proportional to T.

Nugent, Quarles and Solomon provide in [151] experimental evidence for the exponential temporal decrease of the filamental widths. They also show that the chemical pattern is concentrated along the unstable manifold of the passive advection problem, i.e. in regions where the finite time Lyapunov exponent is large. Due to the finite observation times, the patterns turn out to be rather similar to those generated by the open vortex-sink model of Section 2.2.2. It is worth comparing our Fig. 14 with their Fig. 2 (passive cases) and our Fig. 23 with their Fig. 3c–e (reactive cases). The authors describe a qualitative change with parameter τ_m. For long mixing times (fast reactions) the patterns are filamental. They are replaced by extended, large scale chemical distributions for short mixing times (slow reactions). This is in harmony with the onset of synchronization in the reaction as discussed in Section 14 and in [145]. Nugent, Quarles and Solomon suggest to interpret the results by comparing the mixing time with the decorrelation time $T_{\rm BZ}$ of the reaction in the absence of any flow, and find that filamental distributions appear whenever τ_m increases beyond $T_{\rm BZ}$. In our terminology, the ratio $\tau_m/T_{\rm BZ}$ plays the role of a Damköhler number

(cf. Eq. (37)), and the transition from large scale to filamental patterns takes place at a critical Damköhler value, unity.

We do hope that this paper will soon be followed by others revealing experimental evidence concerning other aspects of reactive flows.

References

[1] M. Abel, et al., Phys. Rev. E 64 (2001) 046307;
M. Abel, et al., Chaos 12 (2002) 481;
R. Mancinelli, D. Bergni, A. Vulpiani, Europhys. Lett. 60 (2002) 532.
[2] E.R. Abraham, Nature 391 (1998) 577;
P.W. Boyd, et al., Nature 407 (2000) 695.
[3] E.R. Abraham, et al., Nature 407 (2000) 727.
[4] E. Abraham, M. Bowen, Chaos 12 (2002) 373.
[5] F. Ali, M. Menzinger, J. Phys. Chem. 101 (1997) 2304.
[6] M.M. Alvarez, et al., Phys. Rev. Lett. 81 (1998) 3395;
X.Z. Tang, A.H. Boozer, Chaos 9 (1999) 183.
[7] H. Aref, J. Fluid Mech. 143 (1984) 1.
[8] H. Aref, et al., Physica D 37 (1989) 423.
[9] Aristegui, et al., Deep-Sea Res. 44 (1997) 71.
[10] T.R. Auton, F.C.R. Hunt, M. Prud'homme, J. Fluid. Mech. 197 (1988) 241.
[11] A. Babiano, et al., Phys. Fluids 6 (1994) 2465.
[12] A. Babiano, et al., Phys. Rev. Lett. 84 (2000) 5764.
[14] S. Bartha, T. Czárán, I. Scheuring, N. Z. J. Ecol. 21 (1997) 199–206.
[15] E. Barton, et al., Prog. Oceanogr. 41 (1998) 455.
[16] G.K. Batchelor, An Introduction to Fluid Dynamics, Cambridge University Press, Cambridge, 1967.
[17] I. Benczik, Inertial effects and reactions in chaotic flows, Ph.D. Thesis, Eötvös University, Budapest, 2002.
[18] I. Benczik, Discrete time model for chemical or biological decay in chaotic flows. Lifetime induced phase transitions, preprint, 2004.
[19] I. Benczik, Z. Neufeld, T. Tél, Phys. Rev. E 71 (2005) 016208.
[20] I.J. Benczik, Z. Toroczkai, T. Tél, Phys. Rev. Lett. 89 (2002) 164501;
I.J. Benczik, Z. Toroczkai, T. Tél, Phys. Rev. E 67 (2003) 036303.
[21] G. Benettin, et al., Phys. Lett. A 118 (1986) 325.
[22] M.V. Berry, AIP Conf. Proc. 46 (1978) 16.
[23] F. Bottausci, et al., Philos. Trans. Roy. Soc. (London) A 362 (2004) 1001.
[24] A. Bracco, et al., Phys. Fluids 11 (1999) 2280.
[25] A. Bracco, A. Provenzale, I. Scheuring, Proc. Roy. Soc. B 276 (2000) 1795.
[26] S.L. Bryant, K.E. Thompson, Curr. Opin. Colloid Interface Sci. 6 (2001) 217.
[27] J.H.E. Cartwright, M.O. Magnasco, O. Piro, Chaos 12 (2002) 489;
J.H.E. Cartwright, M.O. Magnasco, O. Piro, Phys. Rev. E 65 (2002) 045203(R);
J.H.E. Cartwright, et al., Phys. Rev. Lett. 89 (2002) 264501;
J.H.E. Cartwright, et al., Phys. Rev. E 68 (2003) 016217.
[28] J.H.E. Cartwright, et al., Phys. Rev. Lett. 93 (2004) 035502.
[29] Q. Chen, M. Ding, E. Ott, Phys. Lett. A 145 (1990) 93.
[30] M. Chertkov, Phys. Fluids. 10 (1998) 3017;
M. Chertkov, Phys. Fluids 11 (1999) 2257.
[31] M. Chertkov, V. Lebedev, Phys. Rev. Lett. 90 (2003) 134501.
[32] P. Chesson, Annu. Rev. Ecol. Syst. 31 (2000) 343.
[33] A. Crisanti, et al., Riv. Nuovo Cimento 14 (1991) 1.
[34] F. Christiansen, P. Grassberger, Phys. Lett. A 181 (1993) 47.

[35] A. Crisanti, et al., Phys. Fluids A 4 (1992) 1805.
[36] J.H. Connell, Science 199 (1978) 1302–1310.
[37] T. Czárán, E. Szathmáry, in: U. Dieckmann, R. Law, A.J. Metz (Eds.), The Geometry of Ecological Interactions: Simplifying Spatial Complexity, Cambridge University Press, Cambridge, 2000.
[38] G.Z. Damköhler, Z. Elektrochem. Angew. Phys. Chem. 42 (1936) 846.
[39] A.J. Dragt, J.M. Finn, J. Math. Phys. 17 (1976) 2215.
[40] B. Eckhardt, Phys. Fluids 31 (1988) 2796;
B. Eckhardt, H. Aref, Philos. Trans. Roy. Soc. London A 326 (1988) 655.
[41] S. Edouard, et al., Nature 384 (1996) 444.
[43] I.R. Epstein, Nature 374 (1995) 321.
[44] I.R. Epstein, H. Showalter, J. Phys. Chem. 100 (1996) 13132.
[45] K. Falconer, Fractal Geometry: Mathematical Foundations and Applications, Wiley, Chichester, 1990.
[47] M. Feingold, L.P. Kadanoff, O. Piro, J. Stat. Phys. 50 (1988) 529.
[48] D.R. Fereday, et al., Phys. Rev. E 65 (2002) 035301(R).
[49] R.A. Fischer, Proc. Annu. Symp. Eugen. Soc. 7 (1937) 355.
[50] U. Gaedeke, U. Sommer, Oecologia 71 (1986) 98–102.
[51] G.F. Gause, A.A. Witt, Am. Nat. 69 (1935) 596.
[52] M. Giona, et al., Physica D 132 (1999) 298.
[53] M. Giona, A. Adrover, Chem. Eng. Sci. 56 (2001) 3387.
[54] M. Gorman, Comb. Sci. and Technol. 98 (1994) 37;
M. Gorman, Comb. Sci. and Technol. 98 (1994) 47.
[55] P. Grassberger, I. Proccacia, Phys. Rev. Lett. 50 (1983) 346.
[56] P. Grassberger, I. Procaccia, Physica 13D (1984) 34.
[57] C. Grebogi, et al., Phys. Lett. 99A (1983) 415.
[58] J.-U. Grooß, et al., to appear.
[59] W.S.C. Gurney, R.M. Nisbet, Ecological Dynamics, Oxford University Press, Oxford, 1998.
[60] T. Halsey, et al., Phys. Rev. A 33 (1986) 1141.
[61] G. Hardin, Science 131 (1960) 1292–1298.
[62] P.H. Haynes, in: H. Chaté, E. Villermaux (Eds.), Proceedings of the NATO Advanced Study Institute on Mixing: Chaos and Turbulence, Kluwer Academic Publishers, Dordrecht, 1996, pp. 229–272.
[63] G.J.F. van Heist, J.B. Flór, Nature 340 (1989) 12;
O.U. Velasco Fuentes, G.J.F. van Heist, J. Fluid Mech. 259 (1994) 79;
A. Longhetto, et al., Il Nuovo Cimento 25C (2002) 233.
[64] M. Hénon, Q. Appl. Math. 27 (1969) 291.
[65] K.H. Hermann, et al., J. Hydrol. 267 (2002) 244.
[66] E. Hernández-García, C. López, Phys. Rev. E 70 (2004) 016216.
[67] E. Hernández-García, C. López, Ecological Complexity 1 (2004) 253.
[68] E. Hernández-García, C. López, Z. Neufeld, Chaos 12 (2002) 470.
[69] E. Hernández-García, C. López, Z. Neufeld, in: G. Bofetta et al. (Eds.), Chaos in Geophysical Flows, OTTO Editore, Torino, 2003.
[70] E. Hernández-García, C. López, Z. Neufeld, Phys. A 237 (2003) 59.
[71] P. Holmes, J.L. Lumley, G. Berkooz, Turbulence, Coherent Structures, Dynamical Systems and Symmetry, Cambridge University Press, Cambridge, UK, 1996.
[72] J. Huisman, F.J. Weissing, Nature 402 (1999) 407.
[73] M.A. Huston, Am. Nat. 113 (1979) 81–101.
[74] G.E. Hutchinson, Am. Nat. 95 (1961) 137–147.
[75] J. Islam, et al., Transport Porous Media 43 (2001) 407.
[76] J. Jacobs, et al., J. Hydrol. 267 (2002) 244.
[77] C. Jung, E. Ziemniak, J. Phys. A 25 (1992) 3929.
[78] C. Jung, T. Tél, E. Ziemniak, Chaos 3 (1993) 555.
[79] H. Kantz, P. Grassberger, Physica D 17 (1985) 75.
[80] G. Károlyi, Phys. Rev. E 71 (2005) 031915.

[81] G. Károlyi, T. Tél, Phys. Rep. 290 (1997) 125.
[82] G. Károlyi, Z. Neufeld, I. Scheuring, Rock-scissor-paper game in a chaotic flow: the effect of dispersion on the cyclic competition of microorganisms, J. Theor. Biol. (2004), to appear.
[83] G. Károlyi, et al., Phys. Rev. E 59 (1999) 5468.
[84] G. Károlyi, et al., Proc. Nat. Academy of Sci. 97 (2000) 13661.
[85] G. Károlyi, et al., Phys. Rev. Lett. 92 (2004) 174101.
[86] G. Károlyi, I. Scheuring, T. Czáran, Chaos 12 (2002) 460.
[87] J.A. Kennedy, Y.A. Yorke, Topol. Appl. 80 (1997) 201.
[88] B. Kerr, et al., Nature 418 (2002) 171.
[89] I.Z. Kiss, et al., Physica D 176 (2003) 67.
[90] I.Z. Kiss, J.H. Merkin, Z. Neufeld, Physica D 183 (2003) 175.
[91] I.Z. Kiss, J.H. Merkin, Z. Neufeld, Phys. Rev. E 79 (2004) 026216.
[92] N.E. Kochin, I.A. Kibel, N.V. Rose, Theoretical Hydrodynamics, Interscience, New York, 1963.
[93] T.-Y. Koh, B. Legras, Chaos 12 (2002) 382.
[94] A.N. Kolmogorov, I.G. Petrovski, N.S. Piskunov, Moscow Univ. Math. Bull. 1 (1937) 1 (Engl. Transl.).
[95] D.K. Kondepudi, R.J. Kaufman, N. Singh, Science 250 (1990) 975.
[96] P. Konopka, et al., J. Geophys. Res. 108 (2004) D5, 8324.
[97] P. Konopka, et al., J. Geophys. Res. 109 (2004) D02315.
[98] Y. Kuramoto, Chemical Oscillations, Waves, and Turbulence, Springer, Berlin, 1984.
[99] L. Kuznetsov, G.M. Zaslavsky, Phys. Rev. E 58 (1998) 7330.
[100] Y.-C. Lai, A.P.S. de Moura, C. Grebogi, Phys. Rev. E 62 (2000) 6421.
[101] L.D. Landau, E.M. Lifshits, Fluid mechanics, Elsevier, Butterworth-Heinemann, Oxford, UK, 2000.
[102] I. Langmuir, Science 87 (1938) 119.
[103] Y.-T. Lau, J.M. Finn, E. Ott, Phys. Rev. Lett. 66 (1991) 978.
[104] F. Ledrappier, L.S. Young, Am. Math. 112 (1985) 540.
[105] Q. Liang, Steep-frontend and chaotic shallow flow processes, Ph.D. Thesis, University of Oxford, Oxford, 2004.
[106] Z. Liu, Y.-C. Lai, J.M. Lopez, Chaos 12 (2002) 417.
[107] C. López, et al., Phys. Chem. Earth B 26 (2001) 313.
[109] C. López, Hernández-García, Eur. Phys. J. B 28 (2002) 353.
[110] C. López, N. Hernández-García, Physica D 199 (2004) 223.
[111] Y. Luo, I.R. Epstein, J. Chem. Phys. 82 (1985) 53–57.
[112] R.S. MacKay, J.D. Meiss (Eds.), Hamiltonian Dynamical Systems, Institue of Physics Publishing, London, 1987.
[113] A. Mahadevan, D. Archer, J. Geoph. Res. 105 (2000) 1209.
[114] T. Makino, N. Ohmura, K. Kataoka, J. Chem. Eng. Japan 34 (2001) 574;
N. Ohmura, et al., J. Chem. Eng. Japan 36 (2003) 1458.
[115] B.B. Mandelbrot, The Fractal Geometry of Nature, W.H. Freeman & Co, San Francisco, 1982.
[116] A.P. Martin, J. Plankton Res. 22 (2000) 597;
S.A. Spall, K.J. Richards, Deep-Sea Res. I 47 (2000) 1261;
A.P. Martin, K.J. Richards, M.J.R. Fasham, J. Mar. Syst. 28 (2001) 65;
V.C. Garcon, et al., Deep-Sea Res. II 48 (2001) 2199.
[117] A.P. Martin, et al., Global Biogeochem. Cycles 16 (2002) 1025.
[118] A.P. Martin, Prog. Oceanography 57 (2003) 125.
[119] M.R. Maxey, J.J. Riley, Phys. Fluids 26 (1983) 883.
[121] C.D. Meinhart, S.T. Werely, J.G. Santiago, Exp. Fluids 27 (1999) 414.
[122] M. Menzinger, A.K. Dutt, J. Phys. Chem. 94 (1990) 4510.
[123] M. Menzinger, P. Jankowski, J. Phys. Chem. 90 (1986) 1217.
[124] M. Menzinger, A.K. Dutt, J. Phys. Chem. 94 (1990) 3410.
[125] G. Metcalfe, J.M. Ottino, Phys. Rev. Lett. 72 (1994) 2875.
[127] E.E. Michaelides, J. Fluids Eng. 119 (1997) 233.
[128] Y. Mizuno, M. Funakoshi, Fluid. Dyn. Res. 35 (2004) 205.
[129] A.E. Motter, Y.-C. Lai, Phys. Rev. E 65 (2002) 015205.
[130] A.E. Motter, Y.-C. Lai, C. Grebogi, Phys. Rev. E 68 (2003) 056307.

[131] A.P.S. de Moura, C. Grebogi, Phys. Rev. E 70 (2004) 026218.
[132] A.P.S. de Moura, C. Grebogi, Phys. Rev. E 70 (2004) 036216.
[133] J.D. Murray, Mathematical Biology, Springer, Berlin, 1993.
[134] S.D. Müller, I. Mezić, J.H. Walter, P. Koumoutsakos, Comp. Fluids 32 (2004) 521.
[135] I. Nagypál, I.R. Epstein, J. Chem. Phys. 89 (1988) 6925.
[136] Z. Neufeld, Phys. Rev. Lett. 87 (2001) 108301.
[137] Z. Neufeld, P.H. Haynes, G. Picard, Phys. Fluids 12 (2000) 2506.
[139] Z. Neufeld, C. López, P. Haynes, Phys. Rev. Lett. 82 (1999) 2606.
[140] Z. Neufeld, T. Tél, Phys. Rev. E 57 (1998) 2832.
[141] Z. Neufeld, et al., Phys. Rev. E 61 (2000) 3857.
[142] Z. Neufeld, et al., Geophys. Res. Lett. 29 (2002).
[143] Z. Neufeld, P.H. Haynes, T. Tél, Chaos 12 (2002) 426.
[144] Z. Neufeld, et al., Phys. Rev. E 66 (2002) 066208.
[145] Z. Neufeld, et al., Phys. Rev. Lett. 91 (2003) 084101.
[146] S. Newhouse, T. Pignataro, J. Stat. Phys. 72 (1993) 1331.
[147] P.K. Newton, The N-vortex Problem, Springer, Berlin, 2001.
[148] T. Nishikawa, Z. Toroczkai, C. Grebogi, Phys. Rev. Lett. 87 (2000) 038301.
[149] T. Nishikawa, et al., Phys. Rev. E 65 (2002) 026216.
[150] X. Niu, Y.K. Lee, J. Micromech. Microeng. 13 (2003) 454.
[151] C.R. Nugent, W.M. Quarles, T.H. Solomon, Phys. Rev. Lett. 93 (2004) 218301.
[152] E. Ott, Chaos in Dynamical Systems, second ed., Cambridge University Press, Cambridge, 1993.
[153] J.M. Ottino, The Kinematics of Mixing: Stretching, Chaos and Transport, Cambridge University Press, Cambridge, 1989.
[154] O. Paireau, P. Tabeling, Phys. Rev. E 56 (1997) 2287.
[155] C. Pasquero, et al., Phys. Rev. Lett. 91 (2003) 054502.
[156] J. Pedlosky, Geophysical Fluid Dynamics, Springer, Berlin, 1979.
[157] Á. Péntek, T. Tél, Z. Toroczkai, J. Phys. A 28 (1995) 2191.
[158] Á. Péntek, et al., Phys. Rev. E 51 (1995) 4076.
[159] R. Pierrehumbert, Chaos Sol. Fractals 4 (1994) 1091.
[160] A. Pikovsky, M. Rosenblum, J. Kurths, Synchronization: A Universal Concept in Nonlinear Science, Cambridge University Press, Cambridge, 2001.
[162] A. Provenzale, et al., Chaos, Solitons Fractals 5 (1995) 2055.
[163] A. Provenzale, Annu. Rev. Fluid Mech. 31 (1999) 55.
[166] C.S. Reynolds, Hydrobiologia 249 (1993) 157–171.
[167] C.S. Reynolds, Freshwater Biol. 39 (1998) 741–753.
[168] M.A. Riley, D.M. Gordon, Trends Microbiol. 7 (1999) 129.
[169] F.J. Romeiras, C. Grebogi, E. Ott, Phys. Rev. A 41 (1990) 784.
[170] V. Rom-Kedar, A. Leonard, S. Wiggins, J. Fluid. Mech. 214 (1990) 347.
[171] D. Rothstein, E. Henry, J.P. Gollub, Nature 401 (1999) 770.
[172] J.C. Roux, P. De Kepper, J. Boissonade, J. Phys. 97 A (1983) L168.
[173] A.B. Rovinsky, et al., OIKOS 78 (1997) 101;
A.B. Rovinsky, et al., Phys. Rev. Lett. 70 (1993) 778.
[174] R.B. Rybka, et al., Phys. Rev. E 48 (1993) 757.
[175] E.J. Samson, et al., Cement Concrete Res. 30 (2000) 1895.
[176] M.A.F. Sanjuán, T. Horita, K. Aihara, Chaos 13 (2003) 17.
[177] G. Santoboni, et al., Chaos 12 (2002) 408.
[178] M. Scheffer, Ecology of Shallow Lakes, Chapman & Hall, London, 1998.
[179] I. Scheuring, et al., Freshwater Biol. 45 (2000) 123.
[180] I. Scheuring, et al., Origins Life Evol. B 33 (2003) 319.
[181] I. Scheuring, et al., Theor. Popul. Biol 63 (2003) 77.
[182] N.M. Schnerb, et al., Proc. Natl. Acad. Sci. USA 97 (2000) 10322.
[183] J. Schneider, et al., Phys. Rev. E 66 (2002) 066218.
[184] J. Schneider, T. Tél, Ocean Dyn. 53 (2003) 64.

[185] I. Schneider, Dynamical structures and manifold detection in 2D and 3D chaotic flows, Ph.D. Thesis, Potsdam University, 2004.
[186] J. Schmalzl, G.A. Hausman, U. Hansen, J. Geophys. Res. 101 (1996) 847.
[187] S.K. Scott, Oscillations, Waves and Chaos in Chemical Kinetics, Oxford University Press, Oxford, 1994.
[188] K. Shariff, T.H. Pulliam, J.M. Ottino, Lect. Notes Appl. Math. 28 (1991) 613.
[189] T. Shinbrot, et al., Phys. Rev. Lett. 86 (2001) 1207.
[190] S. Solomon, Rev. Geophys. 37 (1999) 275.
[191] T.H. Solomon, E.R. Weeks, H.L. Swinney, Phys. Rev. Lett. 71 (1993) 3976;
T.H. Solomon, E.R. Weeks, H.L. Swinney, Physica D 76 (1994) 85.
[192] T.H. Solomon, I. Mezic, Nature 425 (2003) 376.
[193] U. Sommer, et al., Hydrobiologia 249 (1993) 1.
[194] J.C. Sommerer, E. Ott, Science 259 (1993) 335.
[195] J.C. Sommerer, et al., Phys. Rev. Lett. 77 (1996) 5055.
[196] H. Stommel, J. Mar. Res. 8 (1949) 24.
[197] A.D. Strook, et al., Science 295 (2002) 647.
[198] J. Sukhatme, R.T. Pierrehumbert, Chaos 12 (2002) 439.
[199] J. Sukhatme, R.T. Pierrehumbert, Phys. Rev. E 65 (2002) 056302.
[200] D. Sweet, E. Ott, J.A. Yorke, Nature (London) 399 (1999) 315.
[201] T. Takigawa, et al., Forma 15 (2000) 273.
[202] D.G.H. Tan, et al., J. Geophys. Res.-Atoms. 103 (1998) 1585.
[203] P. Tanga, A. Provenzale, Physica D 76 (1994) 202.
[204] T. Tél, in: H. Bai-Lin (Ed.), Directions in Chaos, World Scientific, Singapore, 1990, pp. 149–211 ; H. Bai-Lin (Ed.), in: Statphys 19, World Scientific, Singapore, 1996, pp. 346–362.
[205] T. Tél, et al., Chaos 10 (2000) 89.
[206] T. Tél, et al., Chaos 14 (2004) 72.
[207] D. Tilman, S. Pacala, in: R.E. Ricklefs, D. Schluter (Eds.), Species Diversity in Ecological Communities: The Maintenance of Species Richness in Plant Communities, University of Chicago Press, Chicago, 1993, pp. 13–25.
[208] Z. Toroczkai, et al., Physica A 239 (1997) 235.
[209] Z. Toroczkai, et al., Phys. Rev. Lett. 80 (1998) 500;
Z. Toroczkai, G. Károlyi, A. Péntek, T. Tél, J. Phys. A 34 (2001) 5215.
[210] J.E. Truscott, J. Brindley, Bull. Math. Biol. 56 (1994) 981;
J.E. Truscott, J. Brindley, Philos. Trans. Roy. Soc. London Ser. A 347 (1994) 703.
[211] I. Tuval, et al., Eur. Phys. Lett. 65 (2004) 633.
[212] S. Vainshtein, et al., Phys. Rev. E 50 (1994) 1823.
[213] M. Van Dyke, An Album of Fluid Motion, The Parabolic Press, Stanford, 1982.
[214] E. Villermaux, J. Duplat, Phys. Rev. Lett. 91 (2003) 184501.
[215] H. Vereecken, O. Nitzsche, M. Schulze, SSSAJ 22 (2001) 449.
[216] M. Volpert, et al., in: Proceedings of HEFAT2002, 1st International Conference on Heat Transfer, Fluid Mechanics, and Thermodynamics, Kruger Park, South Africa, 2001.
[218] S. Wiggins, Chaotic Transport in Dynamical Systems, Springer, New York, 1992.
[219] F.A. Williams, Combustion Theory: The Fundamental Theory of Chemically Reacting Flow Systems, Benjamin-Cummings, Menlo Park, 1985.
[220] J.B. Wilson, N. Z. J. Ecol. 43 (1990) 17–42.
[221] A. Witt, et al., Phys. Rev. E 59 (1999) 1605.
[222] S. Wium-Andersen, C. Christophersen, G. Houen, Oikos 39 (1982) 187.
[223] A. Wonhas, J.C. Vassilicos, Phys. Rev. E 65 (2002) 051111;
A. Wonhas, J.C. Vassilicos, J. Geophys. Res. 108 (2003) 4325.
[224] H. Yamada, T. Matsui, Phys. Fluids 21 (1978) 292.
[225] A.N. Yannacopoulos, G. Rowlands, G.P. King, Phys. Fluids 14 (2002) 1572.
[226] L. Yu, E. Ott, Q. Chen, Physica D 53 (1991) 102.
[227] W.R. Young, A.J. Roberts, G. Stuhne, Nature 412 (2001) 328.
[228] A.N. Zaikin, A.M. Zhabotinsky, Nature 225 (1970) 535.

[229] E. Ziemniak, C. Jung, T. Tél, Physica D 36 (1994) 123.
[230] C. Zhou, et al., Phys. Rev. Lett. 91 (2003) 150601.

Further reading

[13] E. Balkovsky, G. Falkovich, A. Fouxon, Phys. Rev. Lett. 86 (2001) 2790.
[42] T. Elperin, N. Kleeorin, I. Rogachevskii, Phys. Rev. Lett. 77 (1996) 5373;
T. Elperin, et al., Phys. Rev. E 66 (2002) 036302.
[46] G. Falkovich, A. Fouxon, M.G. Stepanov, Nature 419 (2002) 151.
[108] C. López, Phys. Rev. E 66 (2002) 027202.
[120] D.S. McKenna, et al., J. Geophys. Res. 107 (D16) (2002).
[126] I. Mezic, F. Sotiropoulos, Chaos 14 (2002) 2235.
[138] Z. Neufeld, P.H. Haynes, T. Tél, Chaos 12 (2002) 426.
[161] O. Piro, M. Feingold, Phys. Rev. Lett. 61 (1988) 1799.
[164] R. Reif, Statistical Physics, McGraw-Hill, New York, 1967.
[165] R. Reigada, F. Sagués, J.M. Sancho, Phys. Rev. E 64 (2001) 026307.
[217] G.A. Voth, G. Haller, J.P. Gollub, Phys. Rev. Lett. 88 (2002) 254501.